2016

Improvements to Prediction and Measurement Capabilities for Airborne Dust Deposition, with Application to Redesign of a Low-Reynolds Number Valve

Ravinder Singh Gill
University of Windsor

Follow this and additional works at: https://scholar.uwindsor.ca/etd

Recommended Citation

Gill, Ravinder Singh, "Improvements to Prediction and Measurement Capabilities for Airborne Dust Deposition, with Application to Redesign of a Low-Reynolds Number Valve" (2016). *Electronic Theses and Dissertations*. 5824.
https://scholar.uwindsor.ca/etd/5824

This online database contains the full-text of PhD dissertations and Masters' theses of University of Windsor students from 1954 forward. These documents are made available for personal study and research purposes only, in accordance with the Canadian Copyright Act and the Creative Commons license—CC BY-NC-ND (Attribution, Non-Commercial, No Derivative Works). Under this license, works must always be attributed to the copyright holder (original author), cannot be used for any commercial purposes, and may not be altered. Any other use would require the permission of the copyright holder. Students may inquire about withdrawing their dissertation and/or thesis from this database. For additional inquiries, please contact the repository administrator via email (scholarship@uwindsor.ca) or by telephone at 519-253-3000ext. 3208.

Improvements to Prediction and Measurement Capabilities for Airborne Dust Deposition, with Application to Redesign of a Low-Reynolds Number Valve

by

Ravinder Singh Gill

A Thesis
Submitted to the Faculty of Graduate Studies
through the Department of Mechanical, Automotive & Materials Engineering
in Partial Fulfillment of the Requirements for
the Degree of Master of Applied Science at the
University of Windsor

Windsor, Ontario, Canada

2016

Improvements to Prediction and Measurement Capabilities for Airborne Dust Deposition, with Application to Redesign of a Low-Reynolds Number Valve

by

Ravinder Singh Gill

APPROVED BY:

_____

Dr. Vesselin Stoilov
Department of Mechanical, Automotive & Materials Engineering

_____

Dr. Ronald Barron
Department of Mechanical, Automotive & Materials Engineering

_____

Dr. Jeff Defoe, Advisor
Department of Mechanical, Automotive & Materials Engineering

_____

Dr. Gary Rankin, Co-Advisor
Department of Mechanical, Automotive & Materials Engineering

September 22, 2016

Declaration of Previous Publication

This thesis includes one original paper that has been previously published/submitted for publication in conference proceedings, as follows:

Thesis Chapter	Publication title/ full citation	Publication status
Chapter 2, 3, and 4	Gill, R.S, Defoe, J.J., and Rankin, G.W. A combined numerical and experimental assessment of air and dust flow in a low Reynolds number valve including modifications to prevent valve seal contamination. Proceedings of the ASME 2016 Fluids Engineering Division Summer Meeting, Washington, DC, USA, July 10-14, 2016.	Published

I certify that I have obtained a written permission from the copyright owner to include the above published material in my thesis. I certify that the above material describes work completed during my registration as graduate student at the University of Windsor.

I declare that, to the best of my knowledge, my thesis does not infringe upon anyone's copyright nor violate any proprietary rights and that any ideas, techniques, quotations, or any other material from the work of other people included in my thesis, published or otherwise, are fully acknowledged in accordance with the standard referencing practices. Furthermore, to the extent that I have included copyrighted material that surpasses the bounds of fair dealing within the meaning of the Canada Copyright Act, I certify that I have obtained a written permission from the copyright owner to include such material(s) in my thesis.

I declare that this is a true copy of my thesis, including any final revisions, as approved by my thesis committee and the Graduate Studies office, and that this thesis

has not been submitted for a higher degree to any other University or Institution.

Abstract

High concentrations of particulate matter in air lead to deposition in critical areas of fluid flow devices involving direct intake from the environment. Dust deposition in critical areas can hamper the performance of such devices. In this thesis, the mechanism which results in dust deposition is investigated by studying and redesigning a self-actuated pressure sealing valve using two computational approaches and experiments. A simplified numerical approach is used which predicts dust deposition by employing the built-in functions of Discrete Phase Modelling (DPM) in the commercial Computational Fluid Dynamics (CFD) software ANSYS Fluent 15.0. Also, an advanced numerical approach is used which links a user defined function (C code) to modify the built-in functions; this enables prediction of particle deposition within 15% with an 80% confidence level. Experiments are conducted to assess the dust deposition patterns and valve performance relative to the device specifications. The numerical and experimental results are utilized together to gain insight into the particle deposition behaviour. This is made possible by the development of an innovative post-processing technique that non-destructively quantifies the dust deposited in experiments without the need for any expensive equipment. A simplified 90° bend geometry is used to experimentally calibrate the advanced deposition model. The main mechanism responsible for dust deposition has been determined to be related to particle impact velocities and angles. Particles impacting a surface at low velocity and angle are more likely to stop. Using this insight, the valve geometry is modified to reduce the dust deposition in critical areas. In the modified design, leakage flow is reduced by up to 93% while still maintaining a positive performance margin relative to specifications.

Dedication

I dedicate this work to my family and friends. A special feeling of gratitude to my loving parents, Kulminder and Parmjit Gill, for providing endless encouragement. My sister, Amanjot Sidhu always gave me a helping hand when needed. I also dedicate this work to Harman Bhangu, for always supporting me with your boundless love and words of motivation.

I dedicate this thesis to the loving memory of my uncle Gursewak Grewal. You will always be remembered.

Acknowledgement

Contents

List of Figures

List of Tables

Nomenclature

Symbols

a particle deformation along the impact surface

b particle deformation normal to the impact surface

Cu Cunningham correction factor

d diameter

E Young's modulus

f correction factor for near wall effect drag force

F force

G gap height at sealing radius

k_s static coefficient of friction

K_C composite Young's modulus

$\dot{m}$ mass flow rate

Re Reynolds Number

r radial coordinate

r^* normalized radius

U velocity magnitude

u fluid velocity parallel to wall

u^* wall friction velocity

U_{avg} average velocity at the outlet of simplified 90° bend channel

$\vec{v}$ velocity

V fluid velocity at the centre of the particle

W work

y wall distance

Δp pressure difference across the valve

θ circumferential coordinate

μ dynamic viscosity of fluid

ν Poisson's ratio

ρ density of fluid

ζ loss coefficient

Subscripts

0 nominal conditions

$1G$ numerical flow inlet to gap at sealing radius

$G2$ gap at sealing radius to numerical flow outlet

A adhesion

cr capture

D drag

L lift

p particle

s surface

S sliding

st sticking

R rolling

max maximum

min minimum

$seal$ sealing

Superscripts

M mass-weighted

$+$ dimensionless quantity

θ circumferentially averaged quantity

Abbreviations

BC Boundary Condition

C.O.R. Coefficient of Restitution

CGDS Cold Gas Dynamic Spray

CFD Computational Fluid Dynamics

DPM Discrete Phase Model

DNS Direct Numerical Simulation

LES Large Eddy Simulation

LFE Laminar Flow Element

LDA Laser Doppler Anemometer

RANS Reynolds-Averaged Navier-Stokes

RMS Root Mean Squared

UDF User-Defined Function

UDML User-Defined Memory Location

Chapter 1

Introduction

Dust deposition is a significant problem in fluid flow devices where flow undergoes diffusion along curved paths. Such devices are found in the oil and gas, automotive, power, and food processing industries. High concentrations of particulate matter in air can lead to deposition in critical areas of these fluid flow devices. In this thesis, a valve actuated by a pressure differential across it is the particular device of interest. The valve is designed and manufactured by a Tier 1 automotive supplier. In this valve, particulate matter deposits at the sealing radius resulting in a leakage flow in the "sealed state" exceeding specifications by as much as three times the value allowed according to specification. When this excessive leakage flow is detected, it triggers a warning in the vehicle on-board diagnostics system. Thus, this contamination leads to in-warranty product replacements by the manufacturer.

1.1   Objectives

This thesis has three objectives. The first is to establish which phenomena lead to dust deposition in these self-sealing valves and determine how to prevent such deposition. A combined numerical and experimental approach is used. Based on insight gained, a redesign of the existing self-actuated pressure sealing valve geometry is developed

and assessed, showing up to a 93% reduction in leakage flow, satisfying specifications. The second objective is to develop an advanced modelling capability which enables accurate prediction of dust deposition. The final objective is to develop guidelines to prevent dust deposition in future products.

1.2 Introduction to the Self-Sealing Valve

The portion of the valve near the seal is essentially axisymmetric, as schematically illustrated in Fig.1-1. The valve is bi-directional, and flow direction and valve operation are controlled by the pressure difference across it. The "seal" is flexible and so moves slightly in response to flow conditions and the movement of the "poppet". The region where the poppet and seal come into contact is called the "sealing region". The valve opens when subjected to a sufficiently large pressure differential; when closed, it isolates an enclosed system from the surrounding environment. When air flows from the environment (flow in the direction indicated Fig. 1-1), dust deposits on the top surface of the poppet. When dust deposition occurs in the sealing region, excessive leakage flow occurs when the valve is closed. Due to the combination of changes in flow channel height and radius, the flow continuously diffuses along a curved path making a 180° turn and then a 90° turn from inlet to the outlet. The Reynolds number, calculated based on the seal gap height and mass-averaged velocity at the sealing radius, is 600. This suggests that the flow is laminar; which is confirmed by the numerical analysis as described in chapter 4. The valve geometry and functionality is explained in detail in chapter 3.
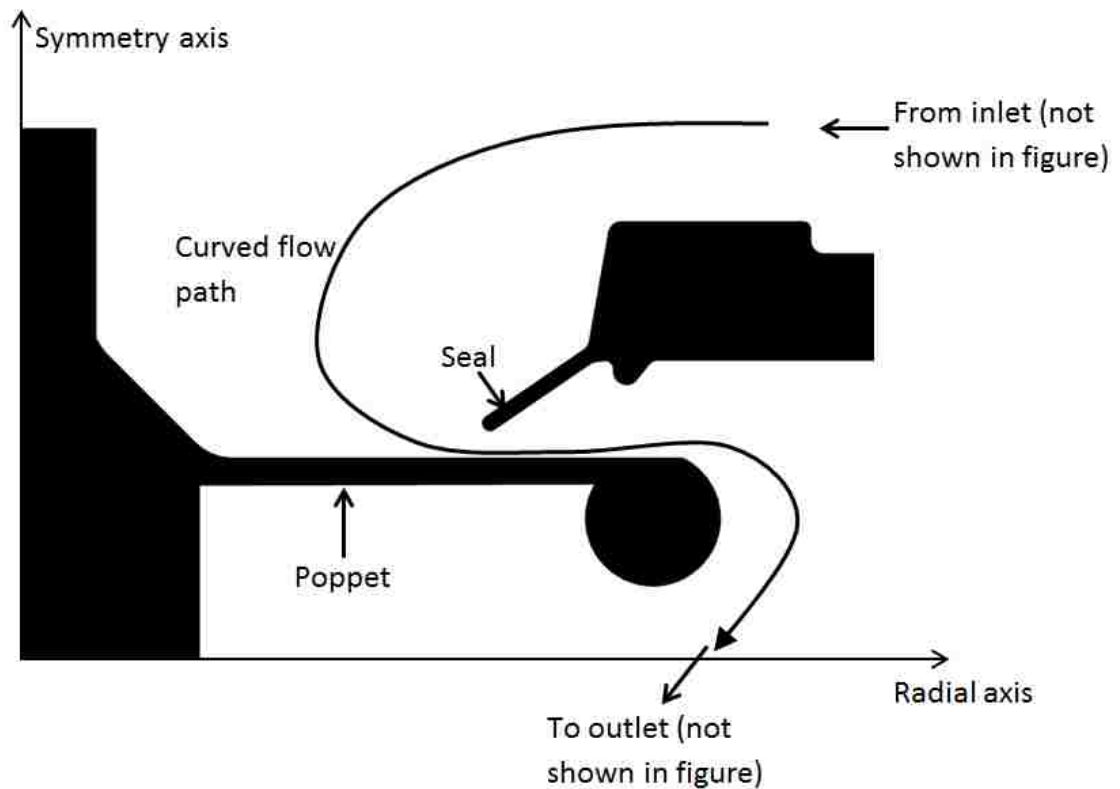
Figure 1-1: Valve geometry showing key components and curved flow path from inlet to outlet.

1.3 Challenges

The complex geometry of the valve and the moving parts make it challenging to understand the flow and dust deposition patterns. Moreover, at the outset, there was no non-destructive method available to quantify and objectively compare the amount of dust deposited on the surface. The problem is made more challenging by the fact that only localized changes to the sealing region are allowed as any alteration to the outer casing of the valve will prove too expensive for the manufacturer.

1.4 High-Level Approach

The work described in this thesis is divided into two phases which align with the first two objectives. In the first phase, simplified numerical computations using the built-in capabilities of the Computational Fluid Dynamics (CFD) package ANSYS Fluent 15.0 [1] are carried out to gain insight into the physical mechanisms responsible for dust deposition in the sealing region. To enable objective comparison of dust deposition patterns determined experimentally (as well as numerically), an innovative image processing approach is developed. Deposition is thus measured experimentally to confirm the numerical findings. The insight gained leads to a valve redesign which yields reductions in leakage flow of up to 93% while maintaining acceptable flow losses. In the second phase, an advanced numerical modelling approach is developed to enhance the numerical prediction accuracy. This model is calibrated with the aid of dust deposition experiments carried out for a rectangular channel with a 90° bend.

1.5 Key Outcomes

The key outcomes of this thesis are:

1. Dust deposition mechanisms for a large range of particle sizes are identified. Particles impacting the surface with a low impact angle have lower momentum in the direction perpendicular to the impact surface and are more likely to deposit.

2. An innovative approach to optically quantify dust deposition is developed which requires only a standard digital camera and post-processing in Matlab [2].

3. The self-sealing valve is successfully redesigned, reducing the leakage flow by up to 93%, while satisfying all specifications.

4. The improved numerical modelling approach is able to predict the amount of particle deposition to within, on average, 15% of the computationally-predicted values with an 80% level of confidence.

5. Design guidelines are established for preventing such contamination issues in future product designs. These guidelines include avoiding the impact of particles with low normal velocities in and near the sealing region, and avoiding deviation of particles from fluid streamlines as much as possible.

1.6   Scope of the Thesis

The existing studies conducted for particle-deposition problems and particle-wall contact mechanisms are discussed in chapter 2. A detailed explanation of the self-sealing valve geometry and its functionality is provided in chapter 3. Chapter 4 describes the simplified numerical analysis and introduces the experiments conducted for natural and artificial dust contamination as well as performance measurement relative to specifications. A modified geometry is also introduced, based on insight gained from simplified analysis. This chapter includes discussion of some limitations of the simplified numerical analysis. Chapter 5 introduces an enhanced numerical model that accurately predicts the dust deposition trends. A simplified geometry with a 90° bend is used to calibrate the model. The self-sealing valve and its modified design are also assessed using this advanced numerical model, showing increased agreement between the predicted and measured dust deposition. The final chapter includes the concluding remarks and recommendations for future product designs.

Chapter 2

Literature Review

Particle deposition is a complex phenomenon which depends on flow characteristics, as well as particle and surface properties. A number of researchers have studied the phenomenon of particle deposition with different flow geometries and Reynolds number regimes. In this chapter, previous research studies related to dust deposition are reviewed. These are followed by a discussion of particle-wall contact mechanics.

2.1   Previous Studies of Particle Deposition

Previous studies of particle deposition provide some guidance in the determination of appropriate modelling approaches. Zhang et al. [3] computationally modelled particle deposition in circular curved pipes with turbulent flow. They studied the secondary flow patterns in curved pipes to evaluate the effects on the particulate phase using a Lagrangian tracking method. It was concluded that particle deposition and pressure drop are significantly affected by complicated flow patterns that depend on Reynolds number and geometric configuration. The valve under investigation in this thesis also has a complex geometry where the flow undergoes a 180° turn along with diffusion. These complexities are thus expected to significantly impact dust distribution.

Chen and Ahmadi [4] performed experiments and numerical simulations to study

the deposition of micron-scale particles in an axisymmetric turbulent flow. They concluded that deposition rates increase with particle size at this scale. The orientation of the geometry in the gravitational field of the Earth is also significant in determining deposition rates. They reported that experimentally-verified numerical simulations can provide good estimates regarding particle transport and deposition in flow passages with complex geometry. Their conclusion leads to the use of computations supported by experiments in the present work.

Matida, Nishino and Torii [5] conducted a study on the deposition of particles onto the wall of a vertical pipe in turbulent flow with a one-way coupled Lagrangian eddy-particle interaction model. The particles investigated had a density of $920\frac{kg}{m^3}$ and diameters between 2μm and 68.5μm. One of the key outcomes of their research is the increased significance of particle inlet conditions as the size of the particles is reduced. With decreased particle size, gravitational effects also diminish in relative importance and the particle path is dominated by fluid dynamics forces. They also concluded that the contribution of Saffman Lift [6] is considerable for particle deposition in turbulent flows. Saffman lift is the lift force experienced by particles in a simple shear flow, with the slip velocity parallel to the flow direction. Similarly to Chen and Ahmadi [4], they also found that particle deposition is affected by gravity. Thus, in the present work it is expected that larger particles deviate more from fluid streamlines and their paths are therefore more difficult to control.

Wilson et al. [7] experimentally and numerically studied aerosol deposition in a 90^0 pipe bend as a function of Reynolds number for turbulent flow for a Stokes number range of 0.1-1.0. The Stokes number is a dimensionless number that characterizes the behaviour of particles suspended in a fluid flow. It is the ratio of the time it takes a particle to respond to changes in the flow to the timescale of the flow. They reported an increase, by a factor of six, in the measured deposition for a three-fold increase in the Reynolds number. Their analysis suggests increased dust deposition

for a Stokes number of approximately 0.4 due to turbulent dispersion. They also concluded that Reynolds-Averaged Navier-Stokes (RANS) computations are sufficient to capture the particle deposition at Reynolds numbers up to approximately 30,000 but for higher Reynolds numbers, the use of Large Eddy Simulation (LES) or Direct Numerical Simulation (DNS) is recommended. This indicates that use of any expensive computational approach is unlikely to be of benefit in the present work since the peak Reynolds number of interest is 600.

Pilou et al. [8] investigated inertial particle deposition in a 90° laminar flow bend employing an Eulerian particle approach with one-way coupling in a two-phase flow. They used an in-house CFD code to simulate the continuous (fluid) phase and a modified convective diffusion equation model to simulate the dispersed (particulate) phase. They calculated the deposition from the sum of diffusive and convective fluxes at the wall. Particle transport was incorporated in the Eulerian description of the particulate phase by adding a Stokes-number-dependent, first-order correction to the particle velocity field. They concluded that the Eulerian-Eulerian model underestimates the particle deposition when compared with deposition predicted by Eulerian-Lagrangian models. This supports the use of a Lagrangian approach to particle path prediction.

Kleinstreuer and Zhang [9] modelled particle deposition in a human airway and experimentally verified the numerical results for laminar, transitional and turbulent flows. They studied flow regimes within a local Reynolds number range of 500 and 10^4 with a low-Reynolds-number $k-\omega$ turbulence model assuming steady incompressible air flow and non-interacting spherical micron-sized particles. The human airway studied is similar to many industrial applications with gas-solid flows in a curved tube. They clearly observed the onset of turbulence with the change in respiratory flow rate from low-level breathing to high-level breathing. This was accompanied by a subsequent decrease in secondary flow. Also, with the increase in flow rate, the particle motion becomes random and disorderly. They concluded that turbulence has

a greater effect on the deposition of smaller particles than it does for larger particles. In the present work, flow is expected to remain in the laminar regime and hence, particles are expected to behave in an orderly manner.

Greenfield and Quarini [10] determined the motion of particles by solving the particle equation of motion, considering the drag force as the primary force acting on the particle. The effect of turbulence is included by using the eddy lifetime model, in which turbulence is modelled as a series of random eddies which have a lifetime and associated random fluctuating velocities. They modified a commercial particle tracking code to include the effects of boundary layers and achieved improved agreement with experiments. Thus, fluid motion in the boundary layer also has a significant effect on particles depositing on the surface.

Abuzeid et al. [11] used both Eulerian and Lagrangian approaches to model the transportation of various particle sizes from a point source in a turbulent channel flow. The Lagrangian approach simulated the turbulent fluctuating velocity field using a Gaussian random process. The particle trajectories in the flow field were calculated using the corresponding particle equation of motion. In the Eulerian method, the mean turbulent flow is simulated using a two equation $k-\epsilon$ turbulence model. Particle diffusion is studied by solving the corresponding advection-diffusion equation. In both approaches, the effect of Brownian diffusion is also modelled. Similar to Pilou et al. [8], the authors concluded that the Lagrangian approach provides more accurate dust deposition patterns than the Eulerian approach. The shortcoming of the Eulerian particle path estimation approach is that it does not provide information on particle impacts at the surface. This further supports the use of a Lagrangian approach for particle path prediction.

Shankara [12] developed a computational deposition model to study the effects of particle deposition on gas turbine vanes. The base model was built using the commercial CFD package ANSYS Fluent, and User-Defined Functions (UDF) to en-

hance Fluent's built-in capabilities and modify the particle-wall interaction boundary conditions. The author predicted higher sticking efficiency for particles with smaller diameter ($\approx 1\mu$m) and very low sticking efficiency for particles with higher diameters ($\approx 30\mu$m) for Mach numbers of 0.85 and 1.02.

A similar approach was followed by Karimi-Esfahani [13] to develop a CFD model for the Cold Gas Dynamic Spray (CGDS) process. The objective was the estimation of particle deposition on an impact target. He used the drag force model available in Discrete Phase Modelling (DPM) in ANSYS Fluent assuming particles of spherical shape and low concentration using the Lagrangian approach. Thus, he considered particle-particle interactions to be negligible and assumed that the fluid flow is not affected by the particle motion. Post-impact particle velocity was determined using the equations of impact dynamics and material properties. Again, a UDF was used to model the particle-wall interaction. The results of predicted post-impact particle velocity are found to be in qualitative agreement with experimental data gathered using a forward-scatter laser Doppler anemometer (LDA).

El-Batsh and Hasebacher [14] provided guidelines for modelling particle deposition on compressor and turbine blade surfaces. They conducted a comprehensive review of the contact mechanics theories available in the literature. They used a critical value of the normal impact velocity which determines if the particle sticks to a surface upon impact. The particles deposited on any surface can be re-suspended in the fluid under the effect of fluid forces for some conditions. This is explained in detail later in this chapter. Both Shankara [12] and Karimi-Esfahani [13] incorporated the contact mechanics and particle-fluid interaction equations into their UDFs to develop an enhanced boundary condition for impacted surfaces.

It is clear that particle deposition heavily depends on the shape of the flow path and Reynolds number. To the best of the author's knowledge, no literature is available that considers the direct prediction of particle deposition in low Reynolds number,

highly curved and highly diffusing laminar flows. As discussed above, the self-sealing valve application has a low Reynolds number flow regime along with complex geometry which involves curved flow paths and diffusion. Most of the work reported in the literature involves flows with much higher Reynolds number and simpler geometries. Hence, to gain insight into the dust deposition patterns in this particular application, numerical simulations and experiments are carried out in tandem. Particle deposition is a result of transportation of the particles by the fluid and particle-wall interactions. In this current study, numerical results are generated using both simplified and advanced numerical approaches. The simplified approach neglects any particle-wall interaction mechanisms. In the advanced numerical analysis, particle-wall interaction mechanisms are modelled in detail in a manner which is explained in the following section.

2.2 Particle-Wall Interaction

Particle-wall interaction mechanisms are an integral part of determining the fraction of particles impacting on a surface that remain on the surface. As mentioned by El-Batsh and Haselbacher [14], particle-wall interaction can be divided into two processes: particle sticking and particle detachment. Particle sticking is a purely mechanical phenomenon which determines whether or not a particle rebounds after impacting a wall. The particle detachment process involves the fluid dynamic interaction between the flow and the particles stuck to the wall. The details of how each of these phenomena are modelled are presented in this section.

2.2.1 Particle Sticking Process

The particle sticking process depends on several parameters including particle size, velocity, angle of impact, and the surface properties of the particle and contact wall.

Many researchers have reviewed the particle sticking or particle adhesion process. It is commonly a result of one or more of the following mechanisms: Van der Waals and electrostatic forces in dry conditions; and liquid bridge forces in wet conditions [14], as indicated in fig. 2-1. Van der Waals force arise from molecular interactions between two surfaces; in this case between a particle and wall. Electrostatic force contributes to the sticking process if the incoming particles are electrically charged in the gas or fluid stream. Liquid bridge force is caused by the formation of a liquid bridge between the particle and contact surface. A liquid bridge consists of an isothermal mass of liquid held by surface tension forces between two bodies in contact [15].
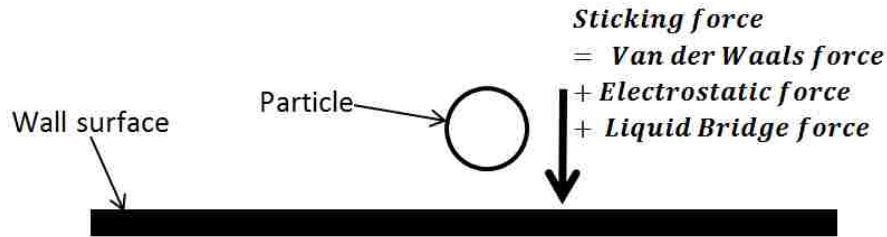
Figure 2-1: Forces contributing to particle adhesion

Berbner and Loeffler [16] studied the significance of these three forces as the particle diameter changes. They concluded that with increases in particle weight and size, the effect of the sticking forces decreases. Therefore, small particles attach to the surface more strongly than do larger particles. They also stated that if it exists, liquid bridge force is dominant. In the current study, dry conditions are assumed, hence, the liquid bridge force is not present. Soltani and Ahmadi [17] conducted a review of adhesion mechanisms and reported that under dry conditions Van der Waals force is the major contributor to particle adhesion. Johnson et al. [18] used the surface energy and surface deformation effects to develop a particle-wall contact model, known as the JKR theory. Based on the JKR theory, Soltani and Ahmadi [17] calculated the sticking force using particle size, and particle and surface material

properties. The sticking force, F_{st}, is given by Soltani and Ahmadi [17] as

$$F_{st} = \frac{3}{4}\pi W_A d_p, \tag{2.1}$$

where W_A is the work of adhesion and d_p is the particle diameter. The work of adhesion for silicon-silicon surfaces in contact is available from literature, determined experimentally by Soltani and Ahmadi [17] and is equal to $38.9 \times 10^{-3} \frac{J}{m^2}$. The dust particles used for analysis in the current study are mostly composed of silicon. To render the analysis tractable, it is assumed that a thin layer of dust already exists on the surface of the wall.

The criteria for particles sticking to the surface is given by Dahneke [19]. He studied the effect of particle impact velocity on the the rebound velocity for spherical particles. He concluded that as the normal impact velocity decreases, the significance of the sticking force increases, which results in decreasing rebound velocities. Below a critical value of normal impact velocity, there is no rebounding of particles and the particles stick to the surface. This velocity is referred to as the capture velocity. Using a mathematical model for the impact and adhesion of spherical particles, Brach and Dunn [20] calculated the capture velocity based on experimental data. The capture velocity, v_{cr} is given as :

$$v_{cr} = \left[\frac{2E}{d_p}\right]^{\frac{10}{7}}, \tag{2.2}$$

where

$$E = 0.51\left[\frac{5\pi^2(k_1 + k_2)}{4\rho_p^{3/2}}\right]^{\frac{10}{7}}, \tag{2.3}$$

The terms k_1 and k_2 are expanded in equations 2.4 and 2.5

13

$$k_1 = \frac{(1 - \nu_s^2)}{\pi E_s}, \tag{2.4}$$

$$k_2 = \frac{(1 - \nu_p^2)}{\pi E_p} \tag{2.5}$$

E_s and E_p are the Young's modulus values (Pa) of the surface and particle materials respectively, ν_s and ν_p are Poisson's ratio values for surface and particle materials respectively. A particle having a normal impact velocity greater than the critical velocity will bounce on contact with the surface.

2.2.2   Particle Detachment Process

Deposited particles become detached and re-suspended in the flow if the fluid forces are large enough to overcome the particle adhesion forces. Soltani and Ahmadi [17] studied various mechanisms of particle detachment. Particles can detach by rolling and sliding, but rolling is the most likely mechanism of detachment for spherical particles.

Detachment by Rolling

When the moment caused by fluid forces about a certain point on the particle-wall contact interface is greater than the moment caused by the adhesion force, the particle begins to roll and hence, is detached. Figure 2-2 depicts the fluid and adhesion forces acting on a particle. Stuck particles will detach from the surface when the following condition is satisfied, obtaining by summing moments about point O:

$$F_D(\frac{d_p}{2} - b) + F_L a \geq F_{st} a, \tag{2.6}$$

In equation 2.6, F_D is the drag force, F_L is the lift force, a is the distance along the surface to point O from the particle centre (representing the deformation of the particle along the surface), and b represents the deformation of the particle normal to the surface.

Soltani and Ahmadi [17] found that the effect of the lift force on detachment is negligible compared to the drag force. Also, in the case of elastic particle adhesion, b is small compared to the particle radius, $\frac{d_p}{2}$, and can be neglected. Therefore, the particle detachment by rolling condition is simplified to

$$F_D \frac{d_p}{2} \geq F_{st} a. \tag{2.7}$$

The deformation along the surface, a is given by Soltani and Ahamdi [17] as

$$a = \frac{3\pi}{2} \frac{W_A d_p^2}{K_C}, \tag{2.8}$$

where

$$K_C = \frac{4}{3} \left[\frac{(1 - v_s^2)}{E_s} + \frac{(1 - v_p^2)}{E_p} \right]^{-1}, \tag{2.9}$$

is the composite Young's modulus.

Detachment by Sliding

Wang [21] studied the effects of initial motion on particle detachment from surfaces and gave a condition for particle detachment by sliding. A particle will detach from the surface if the fluid drag force is strong enough to make the particle slide, that is, when,

$$F_D \geq k_s F_{st}, \tag{2.10}$$

Here, k_s is the coefficient of static friction between the particle and the wall.
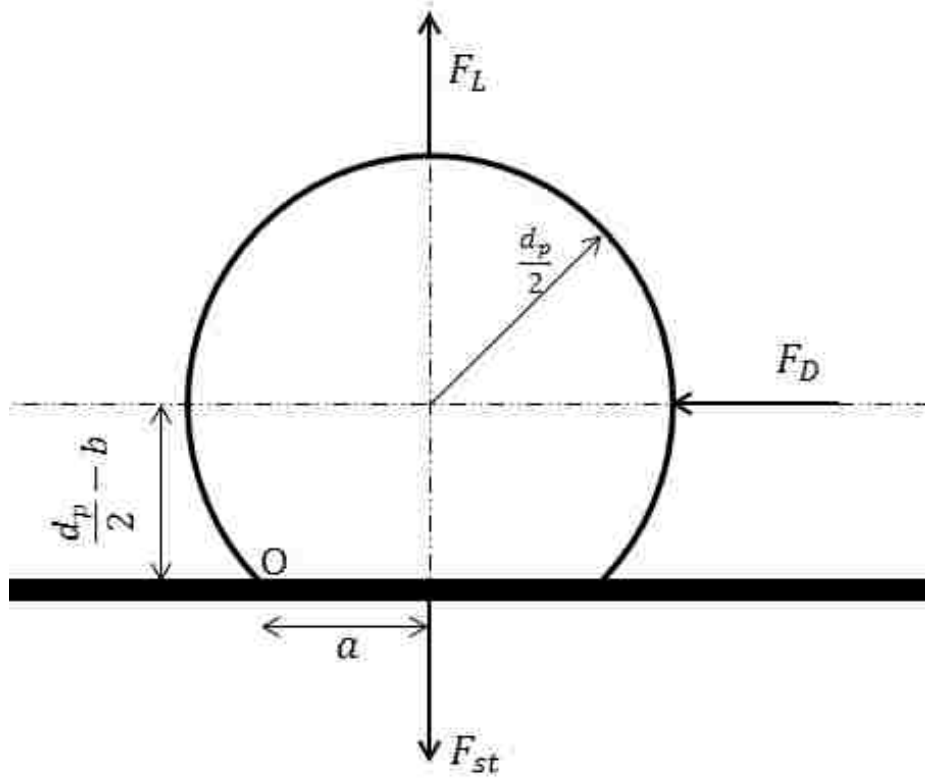
Figure 2-2: Forces acting on a deformed particle stuck to a wall

Limiting Conditions for Detachment by Rolling and Sliding

The drag force on a spherical particle is given by

$$F_D = \frac{1}{2}C_D\rho V^2 \left(\frac{\pi d_p^2}{4}\right)\left(\frac{f}{Cu}\right),$$
(2.11)

where the drag coefficient is given by

$$C_D = \frac{24}{Re_p},$$
(2.12)

and the Reynolds number is given by

$$Re_p = \frac{d_p\rho V}{\mu}.$$
(2.13)

f is a correction factor for the near wall effect given by Soltani and Ahmadi [17] to be approximately 1.7. Cu is the Cunningham correction factor for spherical particles which is approximately 1.0; and $V = \sqrt{u^2 + v_n^2}$ is the fluid velocity at the centre of the particle: u and v_n are the fluid velocity components parallel to and normal to the wall, respectively. As flow is parallel to the wall, $v_n = 0$. Therefore, $V = u$.

For a particle, in the viscous sub-layer, it can be shown that

$$V = \frac{\rho}{\mu} \frac{d_p}{2} u^{*2}, \tag{2.14}$$

which gives

$$F_D = \frac{3\pi}{2} d_p^2 \rho u^{*2}, \tag{2.15}$$

where u^* is the wall shear velocity.

At the limiting condition, u^* is referred to as u_R^* and u_S^* for rolling and sliding respectively. These values represent the critical wall shear velocities.

Substituting the expression for drag force in the rolling limiting condition (eq. 2.7) yields a critical wall shear velocity for rolling:

$$u_R^* = \sqrt{\left(\frac{1}{\rho}\right)\left(\frac{1}{K_C}\right)\left(\frac{W_A}{d_p}\right)}. \tag{2.16}$$

Substituting the expression for drag force in the sliding limiting condition (eq. 2.10 yields a critical wall shear velocity for sliding:

$$u_S^* = 0.5\sqrt{\frac{k_S W_A}{\rho d_p}}. \tag{2.17}$$

Therefore, for a particle to detach and re-suspend in the flow, the wall friction velocity, u^*, has to be greater than the critical wall shear velocities for both the rolling and sliding conditions, or

$$u^* \geq u_R^* \tag{2.18}$$

and

$$u^* \geq u_S^*. \tag{2.19}$$

The particle attachment and detachment models discussed in this section are implemented, calibrated, and assessed in chapter 5 where advanced modelling capabilities are explained.

Chapter 3

Self-Sealing Valve Geometry Details

This chapter introduces important nomenclature related to the valve geometry and explains the function of the self-actuated pressure sealing valve.

Two variants of the self-sealing valve considered in this research are used in practice. Both variants have exactly the same interior geometry. The only difference between the two variants is the inlet geometry. In one variant, the flow enters the inlet plenum (upstream of the region depicted in Fig. 3-2) radially while the other variant has flow entering tangentially. In this thesis, these will be referred to as the radial flow inlet and the tangential flow inlet respectively. Flow visualization experiments, carried out with carbon black and kerosene oil, indicated that the flow downstream of the valve seal is essentially radial for both inlet types, as depicted in Fig. 3-1. Therefore, both the variants of self-sealing valve can be studied by one numerical model. The sealing radius, shown in Fig. 3-1, is where the poppet and seal make contact.
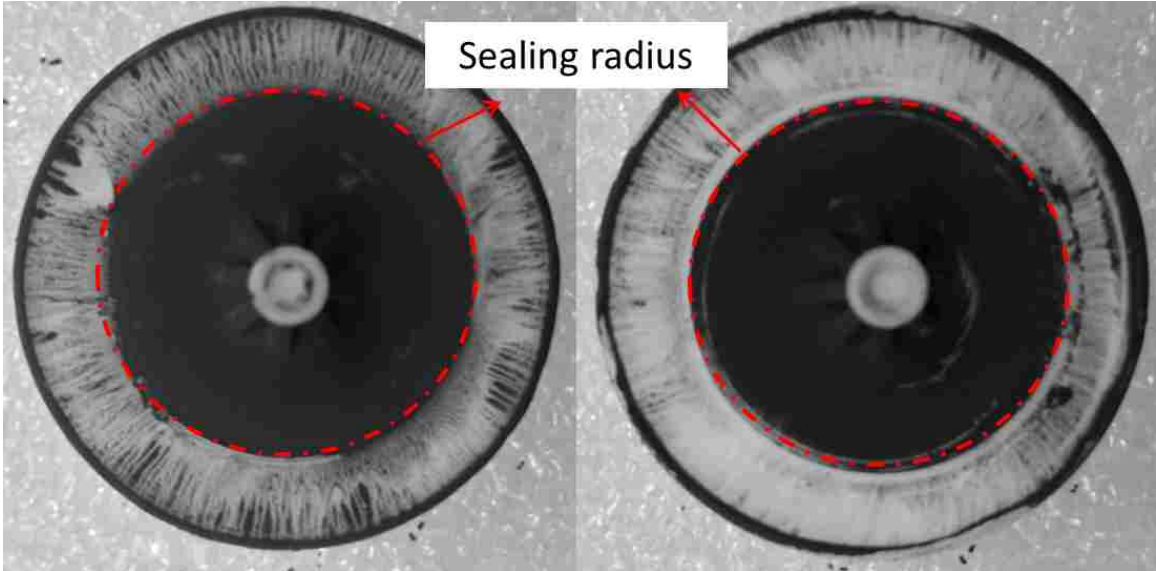
Figure 3-1: Oil film flow visualization of the poppet for radial (right) and tangential (left) inlet flow variants showing near-zero swirl. Flow direction is radially outward.

As mentioned in the introduction, the self-sealing valve is axisymmetric in the region of interest. This is illustrated clearly in Fig 3-2. The opening (gap) of the valve is G, which changes depending on the pressure differential across the valve. When the flow is radially outward through the gap, it originates from the surrounding environment; this is termed the "flow/from environment" condition. When the flow is radially inward through the gap, it exhausts to the surrounding environment; this is termed the "flow/to environment" condition. The nominal conditions for "flow/from environment" operation (the design conditions) are represented by the subscript 0.

The purpose of this self-actuated pressure sealing valve is to provide vacuum/-pressure relief to the fuel tank. This valve is a component of the system that is used in the detection of any leakage in the fuel-vapour line. Fig. 3-3 illustrates how the mass flow and gap size change as functions of the pressure difference across the valve for the tangential inlet variant. The radial inlet variant also functions similarly to the tangential inlet variant, but with a steeper slope for the flow/from environment condition. The valve operation is non-linear, requiring a minimum pressure differen-

tial to open. Once flow from the environment is established, the flow rate and gap size are linearly related. The dynamic pressure based on the mass-weighted average velocity at the gap $\overline{U}_0^M$ is used to non-dimensionalize the pressure difference across the valve. The three functional stages are:
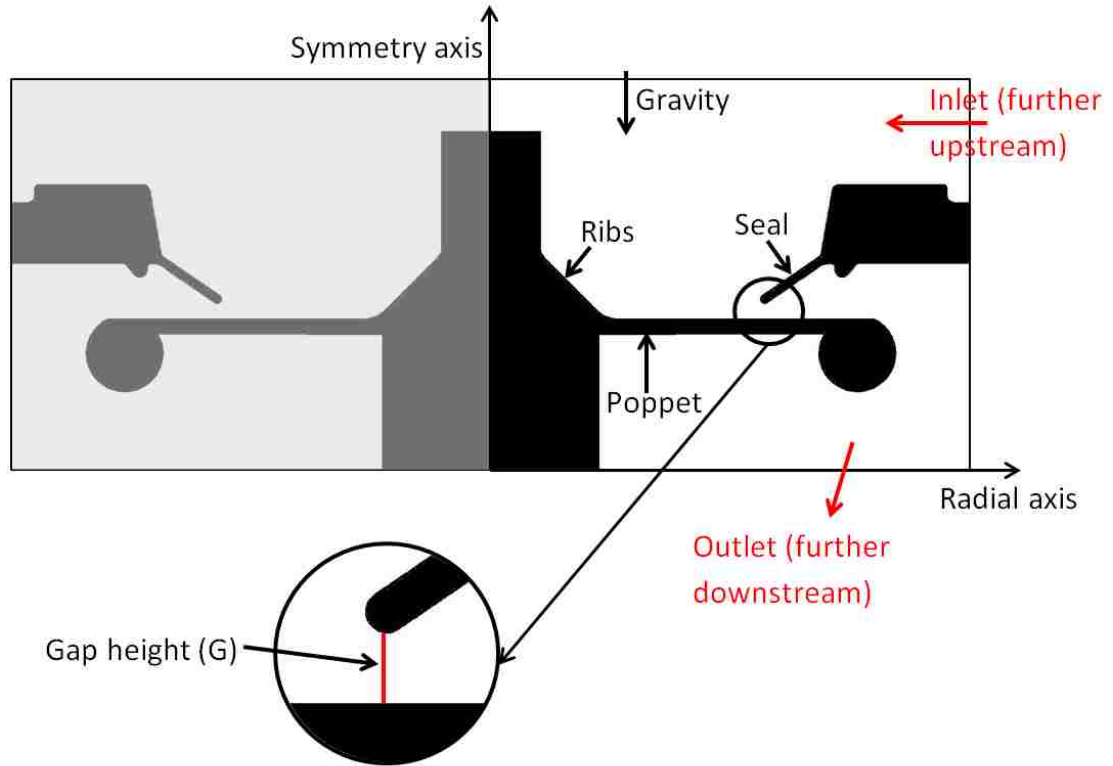
Figure 3-2: Axisymmetric geometry of the self-sealing valve. G represents the valve opening gap.

1. **Sealed Condition:** When the valve is sealed $(G = 0)$, there is not supposed to be any flow through the valve. This position is maintained until a minimum pressure differential is created across the valve.

2. **Flow/from environment:** When the normalized pressure difference (as shown in Fig. 3-3) reaches a value of 3.5, the normalized gap height, G/G_0 and normalized mass flow rate, $\dot{m}/\dot{m}_0$ start to increase linearly. In this condition, the

pressure in the environment is greater than the pressure inside the valve and hence, air flows from the environment (radially outward at the gap).

3. **Flow/to environment:** When the normalized pressure difference (as shown in Fig. 3-3) reaches a value of -1.0, the gap opens suddenly due to the poppet being mechanically pushed downwards, resulting in the large jump in normalized gap height, G/G_0 and normalized mass flow rate, $\dot{m}/\dot{m}_0$ in Fig. 3-3. In this condition, the pressure inside the valve is greater than the pressure in the environment and hence, air flows from inside the valve to the environment (radially inward at the gap).
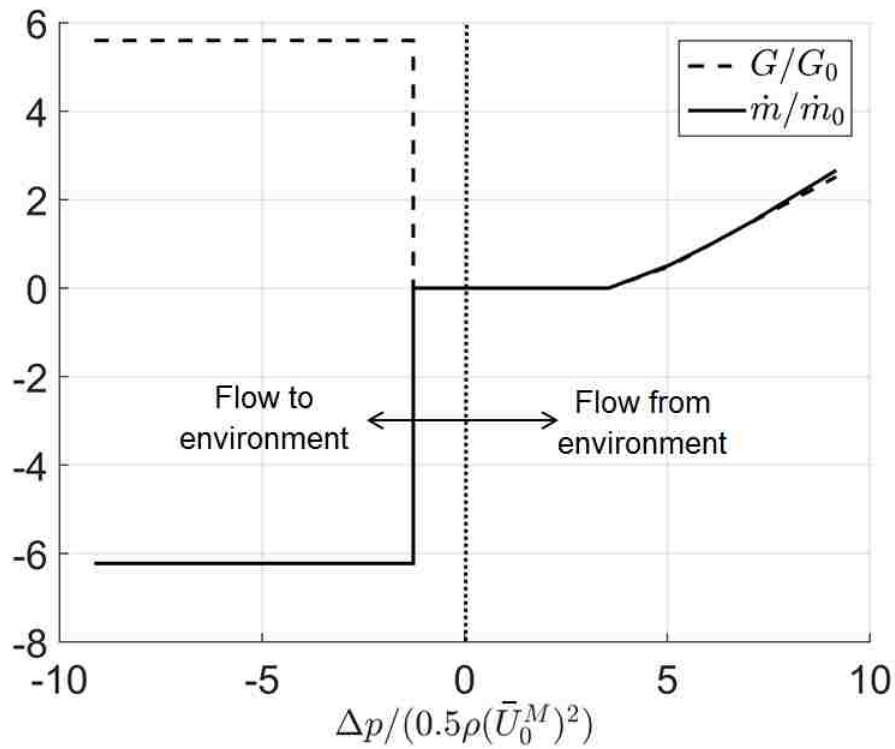
Figure 3-3: Functionality of the tangential inlet variant of the self-sealing valve, showing normalized gap size and mass flow rate as a function of non-dimensional pressure differential.

In the flow/from environment stage, particulate matter also flows into the valve

22

along with air. Over the design lifetime of the valve, the particulate matter deposits in the critical region on the top surface of the poppet. The critical region in this application is the region where the seal and poppet make contact when $G = 0$, which is called the "sealing radius." An annular area surrounding the sealing radius which includes tolerances due to eccentricity between the seal and poppet, quantified below, is defined as the "sealing region." Due to dust deposited in the sealing region during the flow/from environment stage, leakage flow occurs when the valve is supposed to be sealed.

In Fig. 3-4, the sealing radius and the sealing region are schematically illustrated. These are quantified in terms of a non-dimensional radial coordinate

$$r^* = \frac{r - r_{min}}{r_{seal} - r_{min}} \tag{3.1}$$

where r is the radial coordinate, r_{min} is the smallest radius where the poppet surface is flat ($r^* = 0$) and r_{seal} is the sealing radius ($r^* = 1$).

The radial and vertical scales in this valve are related by :

$$r_{seal} - r_{min} = 18G_0 \tag{3.2}$$

The sealing region spans $0.9 \leq r^* \leq 1.1$.

Side View of Poppet

Top View of Poppet

$r^* = 0$ 1.0 1.8

Sealing region
$0.9 \leq r^* \leq 1.1$
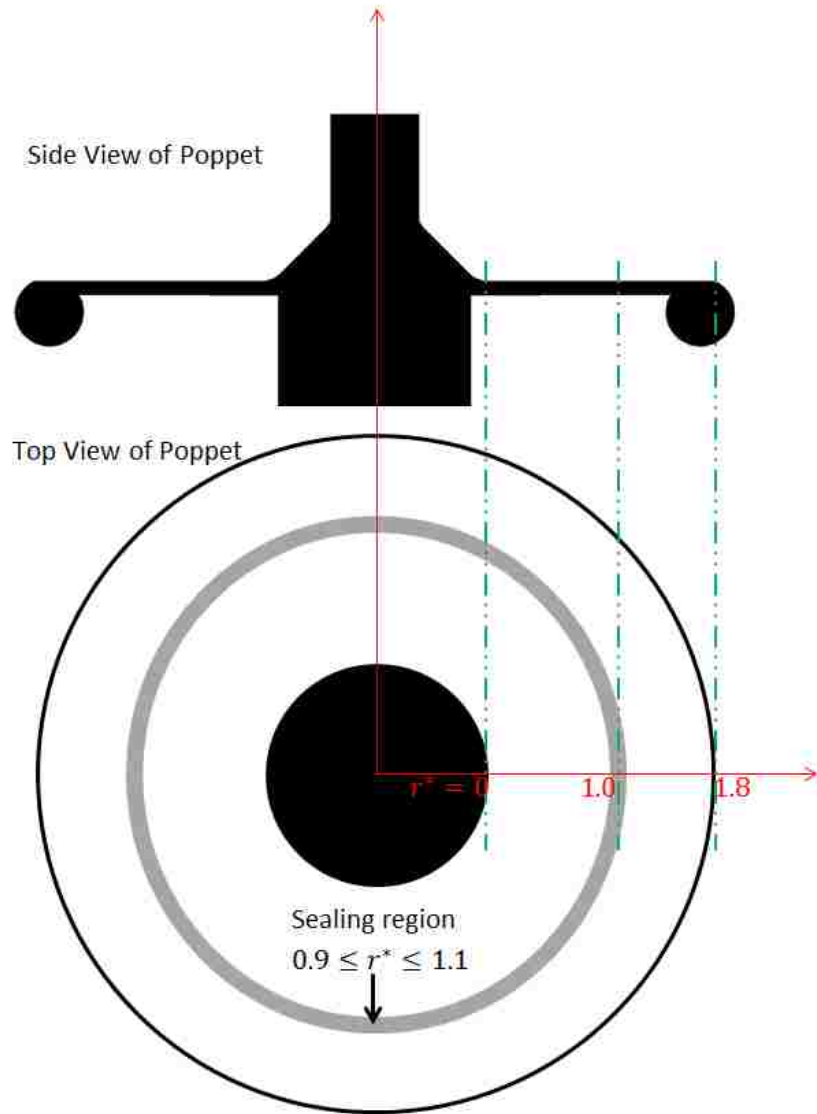
Figure 3-4: Side view and top view of poppet showing the sealing region.

Chapter 4

Assessment of Datum Geometry and Valve Redesign Using a Simplified Numerical Approach and Experiments

This chapter explains the simplified numerical model developed to study the flow and dust problem in the self-sealing valve. The self-sealing valve performance with respect to specifications is studied experimentally. The valve, experimentally subjected to natural and artificial dust deposition, produces dust deposition patterns which are compared to numerical results. The comparisons are enabled by an innovative dust quantification method which is also described. Using the insight gained, the valve geometry is modified. The redesign process and the performance improvements obtained both numerically and experimentally are also detailed in this chapter.

4.1   Computational Setup

In this section, the flow simulation details are first given, followed by information on the DPM approach used in the simplified model.

4.1.1   Flow Field Setup

ANSYS Fluent 15.0 [1] is used to model the flow field using a pressure-based segregated solver. The pressure and momentum equations are spatially discretized to second-order accuracy; the "SIMPLE" pressure-velocity coupling scheme is used. The geometry of the axisymmetric numerical model of the self-sealing valve is shown in Fig. 3-2. The velocity at the inlet is taken to be uniform since the numerical inlet is located far upstream of the region of interest. This is acceptable since the details of the inlet velocity are not considered to be critical. For the numerical outlet, the static pressure is specified. The computational grid is generated with ANSYS Mesher [22] and consists of mostly quadrilateral elements (structured in boundary layers and unstructured elsewhere). The grid has 1.4×10^5 elements. The mesh density varies such that it is finest in the sealing region and gradually coarsens towards the inlet and outlet. The grid pattern in and near the sealing region is shown in Fig. 4-1. The extreme values of mesh parameters such as aspect ratio, skewness, orthogonal quality etc. lie within the acceptable range as suggest by ANSYS. A mesh independence study was conducted and showed only small changes in the key flow metrics when the grid size was doubled. The flow metrics are loss coefficient from inlet to gap (ζ_{1G}), loss coefficient from gap to outlet (ζ_{G2}), and mass-weighted average velocity at the gap ($\bar{U}_0^M$). The changes are quantified in Table 4.1. The loss coefficient is defined as

$$\zeta_{ij} = \frac{p_{t,i} - p_{t,j}}{\frac{1}{2}\rho \left(\overline{U}_0^M\right)^2}. \tag{4.1}$$
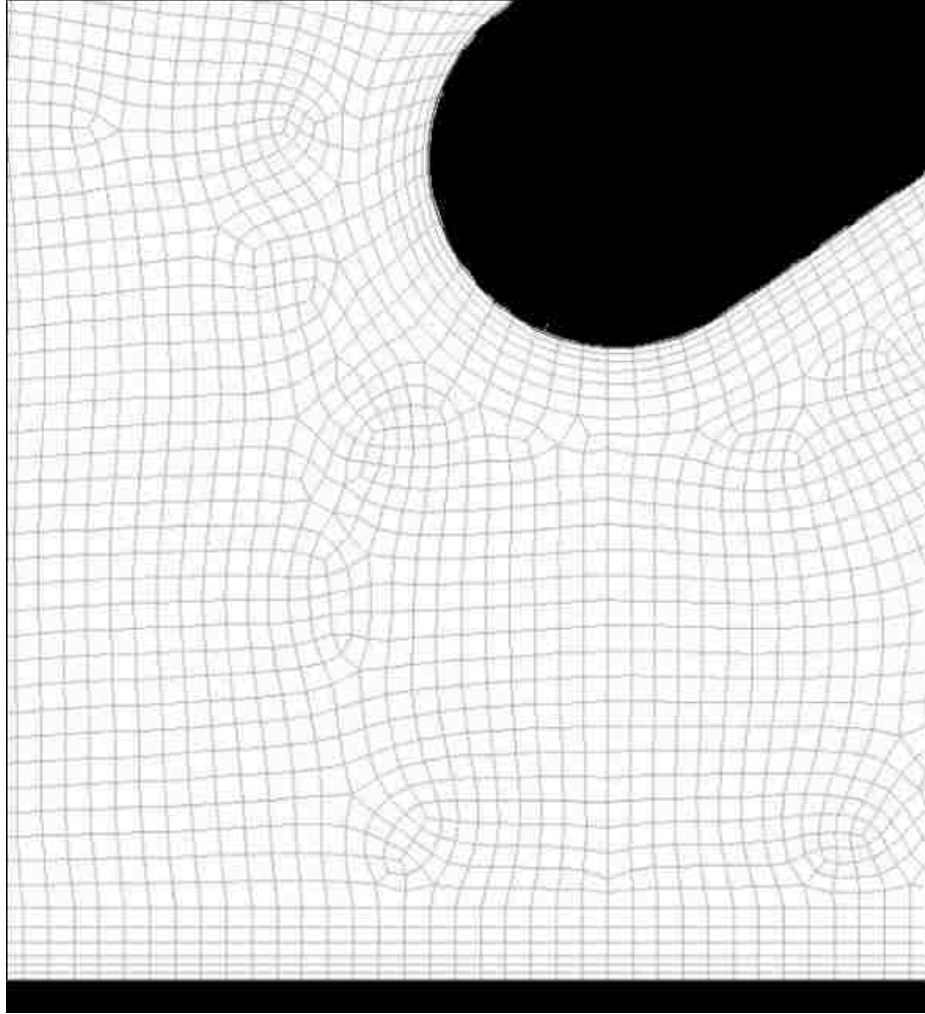
Figure 4-1: Computational grid for the self-sealing valve geometry (in and near sealing region)

Table 4.1: Grid independence study results

Flow metric	% change in 2X finer mesh
ζ_{1G}	0.4
ζ_{G2}	1.32
$\overline{U}_0^M$	0.05

As discussed in the previous chapter, the flow field in the self-sealing valve is axisymmetric and the Reynolds number is in the laminar flow regime. To verify the laminar flow assumption, the flow field is computed using laminar and turbulent (shear stress transport [23]) viscosity models. The difference between the resulting flow fields is negligible. Hence, the laminar approach is used in the remainder of this thesis due to the associated reduced computational cost. The Mach number throughout the valve is found to be less than 0.05, so the flow is modelled as incompressible. Swirl effects are assumed to be negligible as swirl diminishes before the flow reaches the numerical inlet. This is confirmed by the flow visualization experiments, which are shown in Fig. 3-1.

The numerical simulations are considered to be converged when all of the following quantities no longer change by more than 1%:

- Reynolds number based on mass-weighted average velocity at the gap and the gap height,

- pressure coefficients at the inlet and outlet; given by

$$C_p = \frac{p_{1,2} - p_G}{\frac{1}{2}\rho \left(\overline{U}_0^M\right)^2}, \text{ and} \tag{4.2}$$

- loss coefficients ζ_{1G} and ζ_{G2}.

For these quantities, the normalized RMS residuals are at most 5×10^{-5} at this level of convergence.

4.1.2 Discrete Phase Model

Particle paths are computed using the DPM [1] capabilities of Fluent as a post-processing step after obtaining the flow field solution. Using DPM, Fluent allows for the simulation of a discrete second phase in a Lagrangian frame of reference after

solving the transport equations for the continuous phase. In this approach, particle trajectories are calculated based on integration of the particle force balance equation which includes the effects of drag and gravity and can be written as:

$$\frac{d}{dt}\vec{u}_p = \vec{a}_d + \vec{a}_g, \tag{4.3}$$

where $\vec{u}_p$ is the velocity of the particle. $\vec{a}_d$ and $\vec{a}_g$ are the acceleration of the particle due to drag and gravity, respectively, and are given in the Fluent manual [1] as

$$\vec{a}_d = \frac{F_D}{m} = \frac{18\mu^2}{\rho\rho_p d_p^3} \frac{C_D Re_d^2}{24} \frac{\vec{u}_f}{U_f}, \tag{4.4}$$

and

$$\vec{a}_g = \frac{\vec{g}}{\rho_p}(\rho_p - \rho), \tag{4.5}$$

where Re_d is the Reynolds number based on the relative velocity between the particle and fluid:

$$Re_d = \frac{\rho d_p |U_p - U_f|}{\mu}. \tag{4.6}$$

In this work, particle-particle interaction is neglected and only one-way coupling of fluid-particulate phase interaction is considered. This is due to the fact that the dust mass flow rate is six orders of magnitude lower than the air mass flow rate. These assumptions mean that the fluid phase can influence the particulate phase via drag, but the particulate phase has no influence on the fluid phase.

All particles are injected at the flow inlet with a zero initial velocity by choosing a surface injection with uniform particle diameter. The particle-to-fluid density ratio used for analysis is 770:1. For convenience, all particle sizes are normalized with respect to the nominal gap size G_0. The particle sizes used for analysis range from $0.004G_0$ to $0.080G_0$.

Fluent includes the following built-in DPM boundary conditions for particle-wall impacts:

- Reflection : Particles can reflect on impact via elastic or inelastic collision.

- Escape: Particles can escape through a boundary. Such particles are removed from the calculation and reported as incomplete.

- Trap: Particles comes to a complete stop when they come into contact with the boundary.

In reality, the particles may roll, slide, bounce, or come to rest once they impact a surface. The complexity of these possible particle-wall interaction conditions is not captured by any of the built-in DPM boundary conditions. Therefore, in the simplified numerical model used in this chapter, no attempt is made to predict the particle trajectories beyond their first wall impact. Instead, the DPM implementation assumes that all particles come to a complete stop immediately after coming into contact with any solid boundary. The "trap" condition is used to simulate this effect. Hence, the simplified model only predicts the initial impact locations of the particles and assumes that the particles deposit immediately upon impact.

A more advanced modelling approach is used in an advanced numerical model, which is discussed later in chapter 5. This model enables the accurate post-impact prediction of particle trajectories.

4.1.3   Post-Processing of Numerical Results

Particle paths are generated using Fluent and final particle locations are exported for post-processing in terms of non-dimensional radial coordinates, r^*. To visualize the results, the poppet is divided into different r^* bands of width $\Delta r^* = 0.2$. The final particle locations obtained from the computations are assessed to predict the dust

deposition in each band. The output is presented in terms of dust deposited in each band as a fraction of the total dust deposited across all bands.

In the computations, only discrete particle sizes ($0.004G_0$, $0.010G_0$, $0.015G_0$, $0.020G_0$, $0.030G_0$, $0.040G_0$, $0.050G_0$, $0.060G_0$, $0.070G_0$, and $0.080G_0$) are simulated. To determine the contribution from particles of a given size to the dust deposition in a band, weighting based on particle projected area (area of a circle) on the poppet surface is used. The area of a circle is used for the projected area because in the experimental results, dust deposition is viewed and assessed normal to the surface. Dust deposition in each band is further weighted based on the composition of dust particles, which is provided by the manufacturer of dust used in experimental testing. The composition information is given in appendix C and the details of the weighing calculations are found in appendix D. Particles up to $0.010G_0$ in diameter contribute approximately 50% of the dust.

4.2   Experimental Methods

Flow rate measurements are carried out to assess whether the valve satisfies specifications. Dust deposition testing is also conducted to simulate valve operating conditions. The results from the dust testing are post-processed and compared to the numerical results. A leakage test is carried out after contamination with dust to determine leakage flow when the valve is closed (i.e. in the sealed state). Table 4.2 lists the flow rate and leakage flow specifications. The valve must satisfy these specifications when the flow rate measurement and leakage tests are carried out. The remainder of this section describes each experiment.

Table 4.2: Valve flow specifications.

Flow condition/ direction	$\Delta P/(0.5\rho(U_0^M)^2)$	$\dot{m}/\dot{m}_0$
Open/to Environment	-9.13	< -6.22
Open/from Environment	9.13	> 2.64
Closed/from Environment	1.52	$< 1.83 \times 10^{-4}$

4.2.1 Flow Rate Testing

The purpose of flow rate testing is to ensure that the valve satisfies the minimum flow rate requirements for a specific pressure differential in both the to- and from-environment directions. Figure 4-2 schematically illustrates the manner in which the flow rate testing is conducted. The flow enters a filter, which is connected to a mass flow rate meter (TSI 4045 [24]). The pressure differential across the valve is measured using a pressure transducer (Rosemount 3051 [25]).

The uncertainty in measuring the pressure differential across the valve with the pressure transducer is 0.14% of Δp for the "open/to environment" and "open/from environment" conditions. The uncertainty in mass flow rate measurement with the mass flow rate meter is 2% of the $\dot{m}_0$ value. The details of the calculations of these uncertainties are given in appendix E.3.

The purpose of adding a filter in front of the mass flow rate meter is to protect it from airborne particles. The filter removes 99.97% of particles of size $\geq 0.006G_0$ from the ingested air.
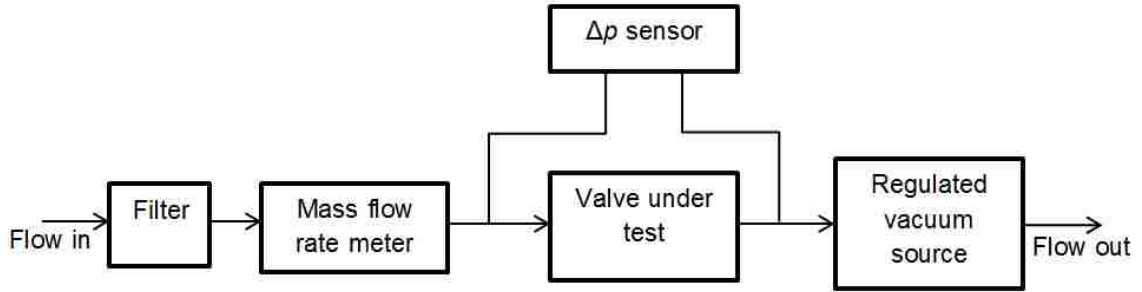
Figure 4-2: Schematic of the flow rate testing setup.

4.2.2 Dust Deposition Testing

Dust testing is conducted to artificially contaminate clean valves, both in the lab as well as in the field. The lab testing allows for an accelerated dust test to assess dust deposition. The field testing allows for collection of accurate dust deposition patterns as seen in real-life situations.

In lab testing, the mass flow rate of air is matched to the valve design operating conditions ($\dot{m}_0$). The dust concentration however, is increased by four orders of magnitude to account for dust deposited over the life of the valve in a shorter time span. This approach has been used in the past by the project's industrial sponsor and has shown similar dust deposition patterns as occur at the end-of-life in the valves. The dust used in this test is Arizona fine dust (manufactured by Powder Technologies Inc.) with particle diameters up to $0.080G_0$. The test lasts approximately 1-2 minutes.

Figure 4-3 shows a schematic diagram for the dust deposition testing setup. Air and dust flow are supplied to the valve through a dust ingestion chamber, which has two inlets and one outlet. The mass flow rate meter and filter used downstream of the valve are the same make and model as used in the flow rate testing (Section 4.2.1). Although there is no filter attached upstream of the valve, large particles never reach the sealing region as they settle in the outer casing of the valve under the effect of gravity. Downstream suction is provided using a regulated vacuum source to match

33

the nominal flow conditions i.e. nominal mass flow rate, $\dot{m}_0$, and nominal gap size, G_0, in the flow/from environment condition.

In field testing, the mass flow rate of air as well as the dust concentration are matched to valve design operating conditions. Natural airborne dust is supplied upstream of the valve without any filter. The test runs continuously for approximately 1000 hours, which corresponds to the valve design lifetime. This test was devised by the project's industrial partner and is utilized in this work to support results from the lab tests.

Photographs of the dust deposition patterns on the poppets of the tested valves are post-processed using an innovative image comparison approach, which is discussed next.
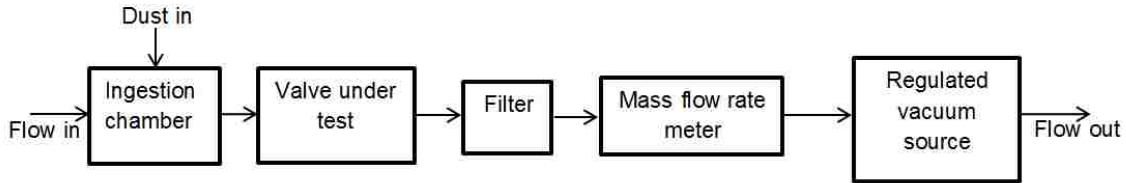
Figure 4-3: Schematic of the dust deposition testing

4.2.3   Post-Processing Approach

An innovative dust quantification post-processing technique is developed in this research work. This technique allows numerical and experimental results to be compared. This method indirectly and non-destructively quantifies the dust deposited on a surface. The approach is implemented using Matlab R2015a [2].

The technique is developed based on the assumption that for a given region, the difference in brightness between a contaminated and clean part is proportional to the fraction of the region covered by dust.

The surface of the poppet is white in colour. Since the method operates on a

difference in brightness (greyscale level), a value of 1.0 corresponds to a perfectly clean location (one no darker than on the clean part) and a value of 0 corresponds to a "fully" contaminated location – one completely covered in dust (completely black). Intermediate levels allow for a quantification of the amount of dust covering the area captured by an individual pixel.

This assumption is visually explained in Fig. 4-4. In the figure, it is assumed that the information captured in one pixel of a digital image is the result of four sub-pixels, though in reality each pixel combines information from the area captured into a greyscale level. For each pixel, the pixel shade (greyscale index) is a reflection of the number of sub-pixels that are completely white (no dust) and completely black (dust).
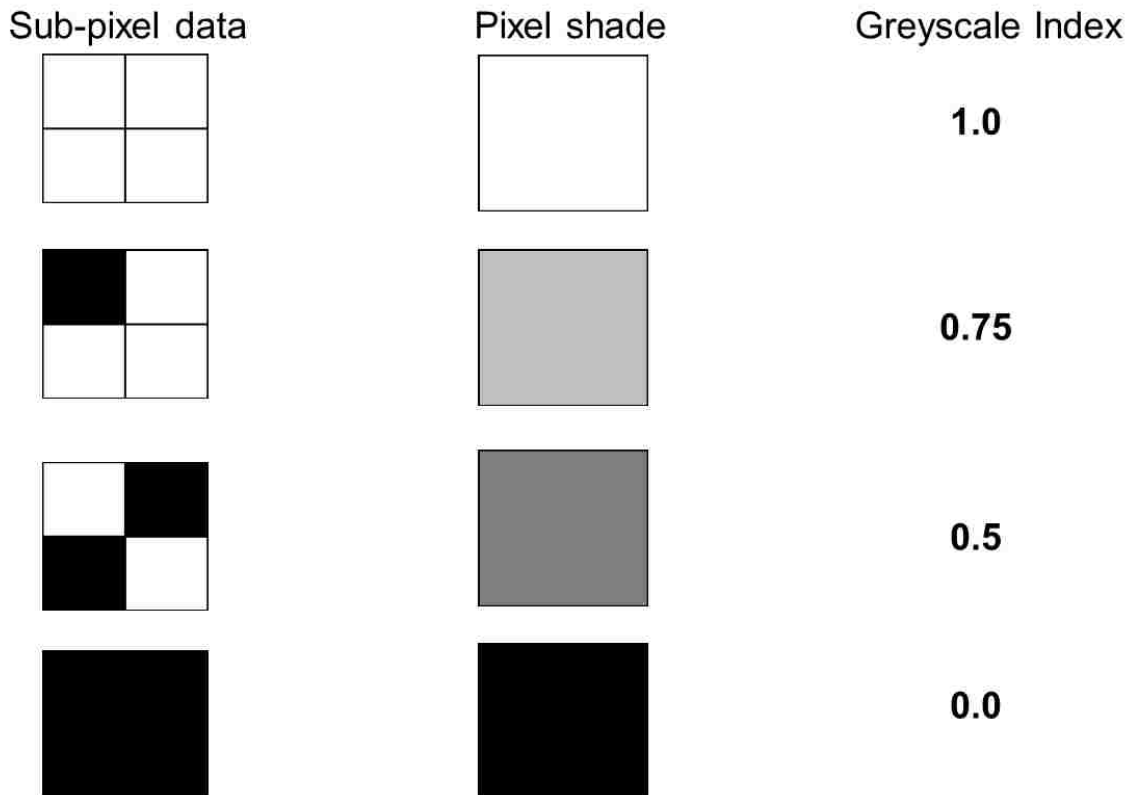
Figure 4-4: Pixel shade and greyscale index corresponding to sub-pixel data

After the dust deposition testing, the valve is carefully disassembled and an image

of the poppet surface (sample part) is captured along with the image of a clean poppet surface from a new valve (reference part) under the same lighting conditions. These images are captured normal to the poppet surface. Each image is stored as a greyscale Cartesian matrix. An interactive boundary identification process sets the poppet radius in pixels and discards data outside the poppet's bounding box. Also, the ribs at the centre of poppet (shown in Fig. 3-2) are disregarded ($r^* < 0$). Therefore, only data bounded by $r^* = 0$ to $r^* = 1.7$ is kept for analysis. As the poppets are circular in shape, Cartesian coordinates used for storing raw images are converted to polar coordinates with zero radius at the centre of the poppet. Points in the polar matrix are then interpolated onto a regular grid of (r, θ) points. Circumferential averages are computed at each radial location. These averages are stored in a brightness matrix ($\bar{B}^\theta$). The difference between the brightness matrix of the reference and the sample parts is calculated. This yields an average change in brightness at each radial location; this is stored in a change in brightness vector ($\Delta \bar{B}^\theta$). The change in brightness is area-averaged for eight equally-spaced intervals of $\Delta r^* = 0.2$. This change in brightness represents the amount of dust deposited on the surface of the poppet in each of these non-dimensional radial intervals. Here it is assumed that there is only one layer of dust deposited on the surface. The fraction of dust deposited in each interval is then calculated by dividing the amount of dust in each interval by the total dust deposited in all intervals. To visualize the results, the fraction of dust deposited is plotted for each Δr^* band. Figure 4-5 illustrates the steps involved in the post-processing approach.
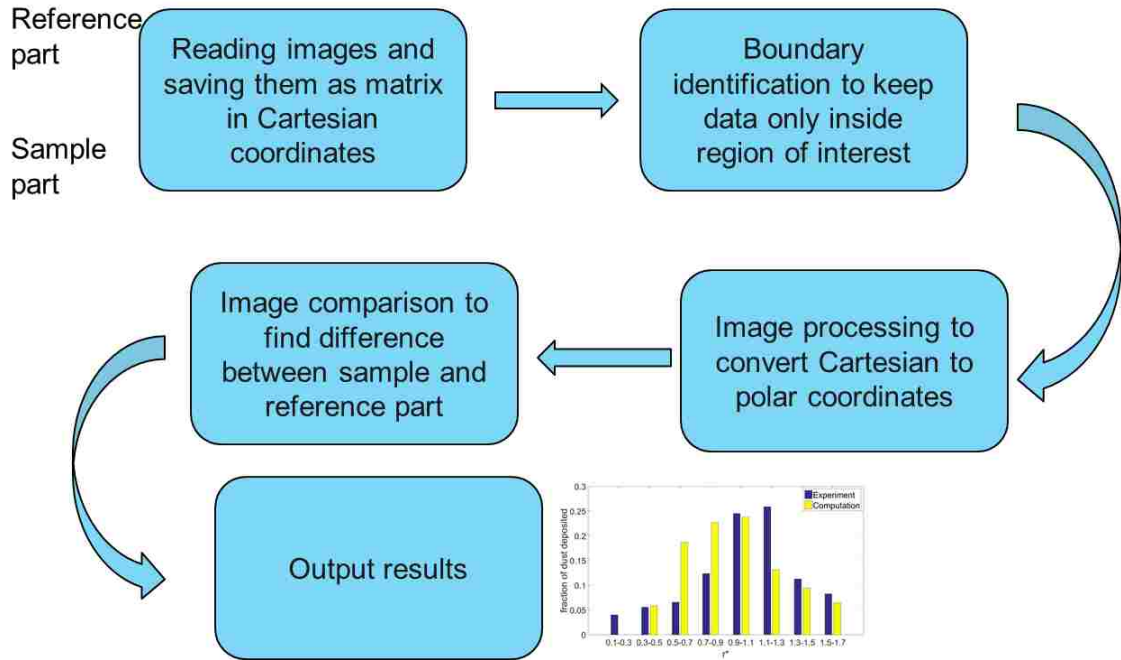
Figure 4-5: Overview of post-processing technique.

The uncertainty associated with this post-processing dust quantification routine is 0.54% of full scale, which includes the uncertainty in the user input process and that associated with the quantization of the brightness data. The calculation of this uncertainty is detailed in appendix E.5.

4.2.4 Leakage Flow Testing

Leakage flow testing is conducted after artificially contaminating the valve. The leakage test is done with a small non-dimensional pressure differential value of 1.52 (see Fig. 3-3) to assess any increase in leakage due to dust deposition on the poppet. A schematic of the leakage flow testing setup is shown in Fig. 4-6. Leakage flow is measured with a laminar flow element (LFE), (Meriam 50MK10-6 [26]) which has an accuracy of 0.72%. The filter upstream of the LFE is designed to stop particles of size $0.020G_0$ and larger. The pressure transducers (Rosemount3051s [25]) give measurements with 0.6% and 0.83% uncertainty for the Δp across the LFE and across

37

the valve under testing, respectively. The resultant uncertainty in the leakage flow measurement is 2.76% of the reading. The determination of these uncertainties is described in appendix E.4.
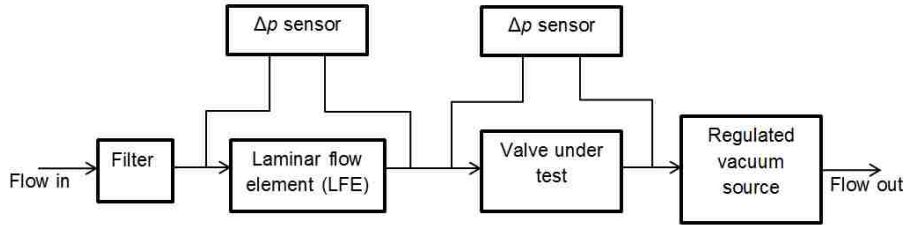
Figure 4-6: Schematic of the leakage flow testing

4.3 Datum Self-Sealing Valve Design Assessment

In this section, the experimental and numerical results for the datum valve design are presented and compared.

4.3.1 Experimental Assessment

All experiments described in the previous section are conducted to assess the datum self-sealing valve design for both inlet configurations i.e tangential and radial inlet flow. The flow rate and leakage test results are given in Table 4.3. The flow rate tests are conducted on clean valves and the leakage flow test is conducted on a contaminated valve (after the in-field dust deposition testing). The experiment results indicate that:

1. in all cases, the flow rate specifications in the "open" conditions are satisfied;

2. in all cases, the leakage flow in the closed state exceeds specifications, sometimes by up to 3 times the specification value; and

3. the increased flow rates for the radial flow inlet at the same pressure differential implies that flow losses are lower for this inlet geometry.

38

Table 4.3: Flow rate and leakage flow test results for datum self-sealing valves.

	Tangential flow inlet			Radial flow inlet		
Flow condition/direction	$\dot{m}/\dot{m}_0$	Specification pass/fail	Margin of pass/-fail	$\dot{m}/\dot{m}_0$	Specification pass/fail	Margin of pass/-fail
Open/ to environment	-6.42	Pass	3.2%	-9.53	Pass	53.2%
Open/ from environment	4.05	Pass	53.4%	5.55	Pass	110%
Closed/ from environment	1.49×10^{-4}	Fail	-6.0%	7.93×10^{-4}	Fail	-333%

The reason for the leakage test failure becomes evident upon comparing experimental and numerical results using the post-processing dust quantification approach. As explained in the previous section, post-processing results for dust deposition are depicted in bands of $\Delta r^* = 0.2$ as shown in Fig. 4-7. This indicates that most deposition occurs in the vicinity of the sealing region, particularly in the range of $0.9 \leq r^* \leq 1.3$. This is exactly the opposite of the desired behaviour. This dust depositing in and around the sealing region is responsible for the self-sealing valve design failing the leakage test results as presented in Table 4.3. The simplified numerical model assumes that the dust deposits upon impact on the poppet surface. All the particle sizes considered for analysis impact the poppet surface in or upstream of the sealing region. Thus, Fig. 4-7 shows that computations predict no deposition

39

downstream of the sealing region. In the experiments, the particles can bounce, roll or slide and continue their trajectories after impact with the surface. Thus, this results in experimental dust deposition downstream of the sealing region as seen in Fig. 4-7.
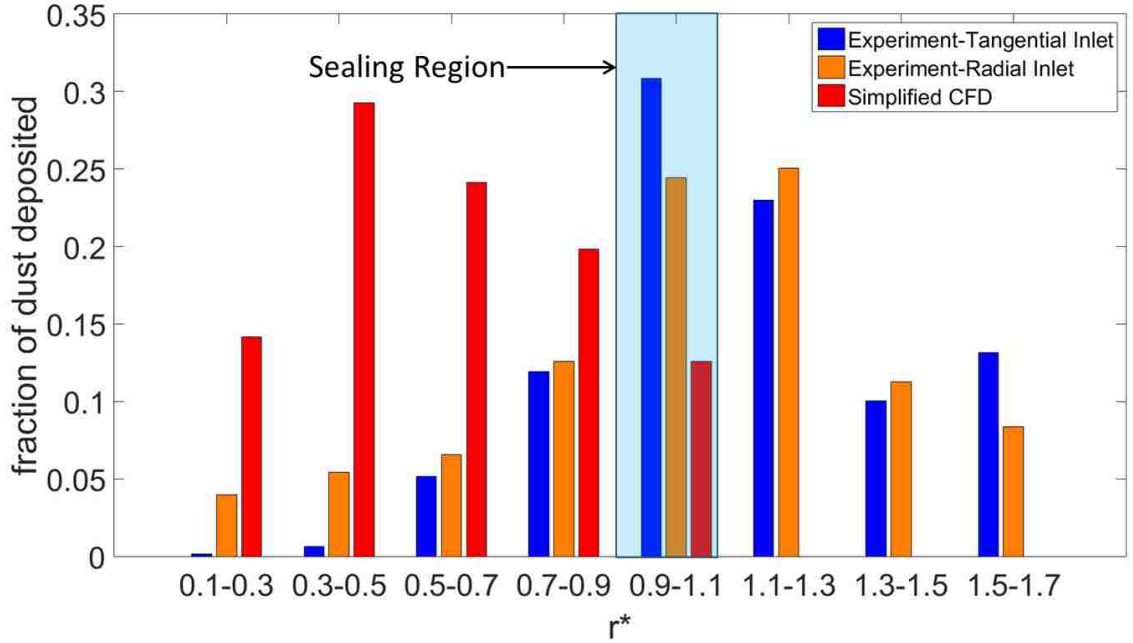
Figure 4-7: Radial distribution of numerically predicted and experimentally measured dust deposition on the poppet for datum valve. Numerical prediction is based on initial particle impacts only.

4.3.2 Assessment of Numerically Predicted Particle Impacts

The paths of various diameters of particles are investigated to gain insight into the experimental results. These paths indicate that small particles (diameters $\leq 0.004G_0$) follow the fluid streamlines closely and hence pass through the sealing region without impacting the poppet surface. Particles of size $0.010G_0$ and larger start to deviate from the fluid streamlines and impact the poppet surface in the sealing region as shown in Fig. 4-8. Figure 4-9 reveals that the particles of diameter $0.020G_0$ impact in and before the sealing region. By studying these particle tracks in detail, it is

found that particles of diameters $0.010G_0$ and $0.020G_0$ impact the poppet surface over a narrow range of r^* from 0.85 to 0.98.
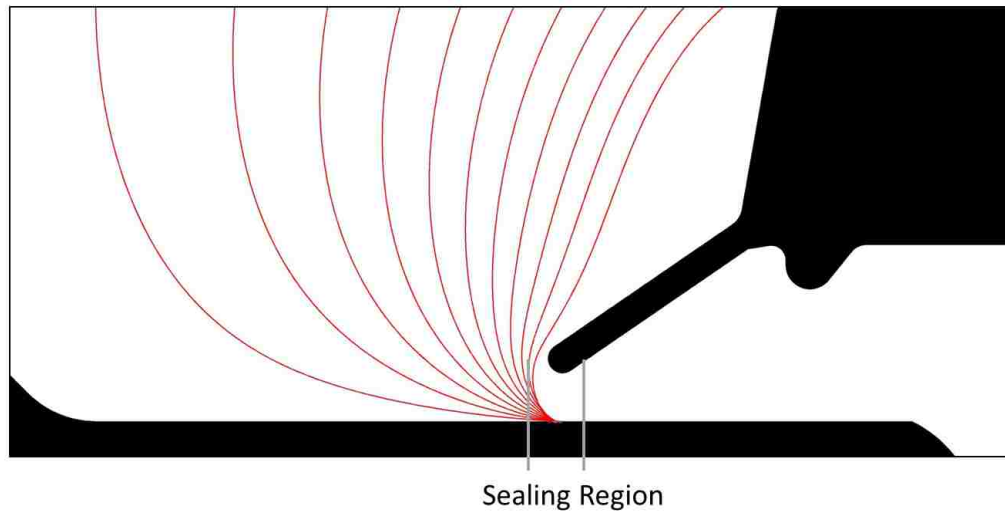
Figure 4-8: Predicted tracks of particles of diameter $0.010G_0$. Particles impact in the sealing region.
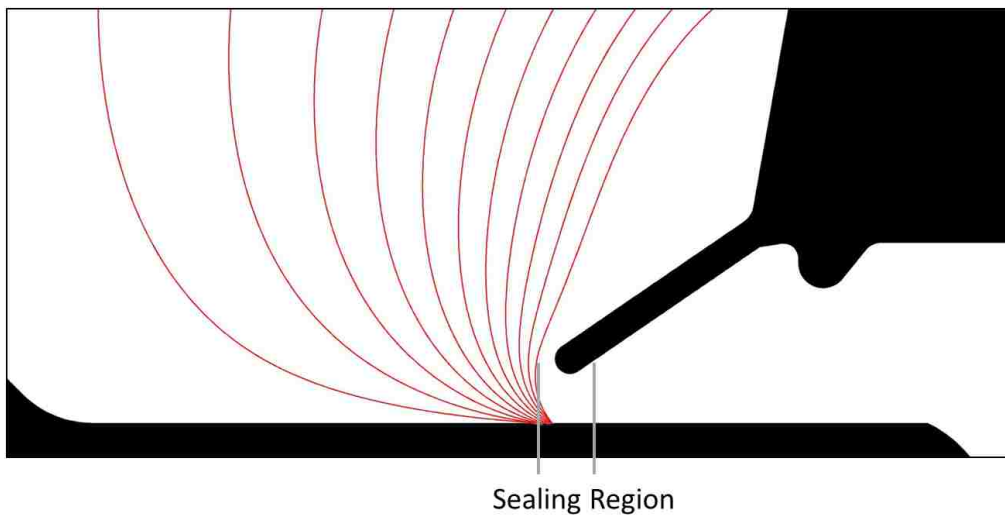
Figure 4-9: Predicted tracks of particles of diameter $0.020G_0$. Particles impact before and in the sealing region.

Figure 4-10 depicts the particle tracks of $0.040G_0$ diameter particles. Particles of

this and larger diameters impact the poppet surface upstream of the sealing region, with $0.040G_0$ particles impacting between $r^* = 0.45$ and $r^* = 0.88$. The same trend of impacts further upstream and with a wider particles spread is observed for particles of diameter $0.080G_0$.
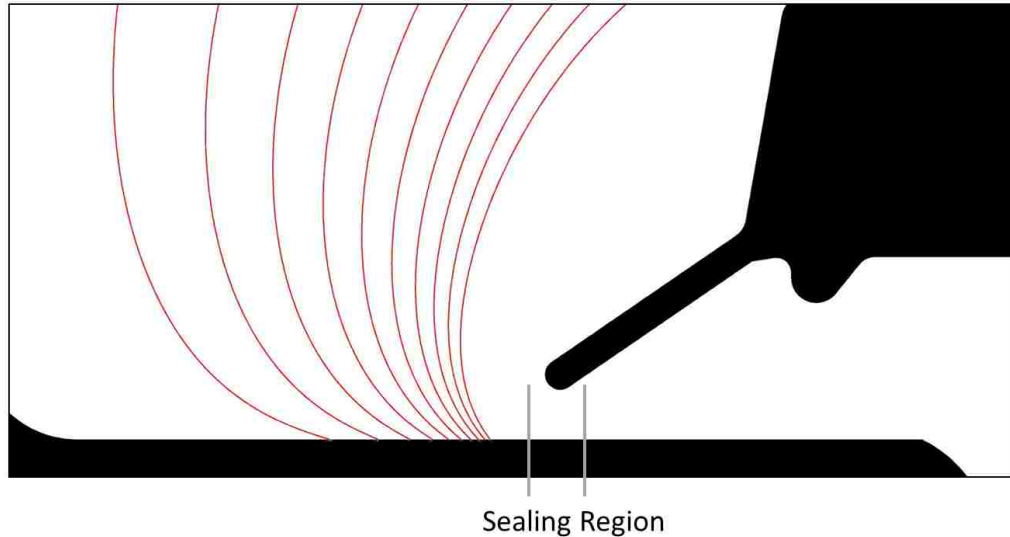
Sealing Region

Figure 4-10: Predicted tracks of particles of diameter $0.040G_0$. Particles impact just before the sealing region.

Particles of discrete discrete are weighted to predict total dust deposition, using the process explained in section 4.1.3. The contribution of individual particle sizes to the total dust distribution is broken down in Fig. 4-11. Since the simplified model only predicts particle tracks up to the first impact location, Fig. 4-11 also indicates at what radial distance the particles impact on the poppet surface. Only small particles up to diameter $0.030G_0$ impact in the sealing region, which can also be seen in Figs. 4-8 and 4-9. As the size of the particles increase, the initial impact location of the particles moves upstream of the sealing region. However, the larger particles ($\geq 0.040G_0$) are expected to bounce more than the smaller particles (up to diameter $0.030G_0$) and hence may impact again on the poppet surface. In total, the predicted fraction of dust deposited along the poppet surface is 73% of the particles

supplied at the inlet.
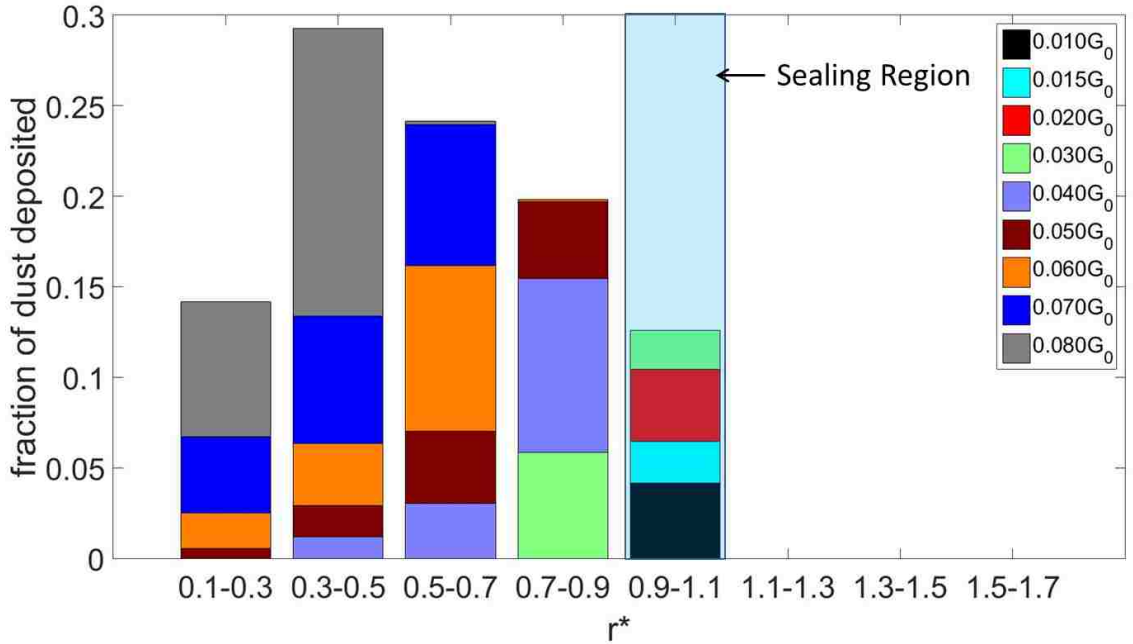
Figure 4-11: Prediction of contribution of individual particle sizes to total dust distribution in datum valve geometry using simplified numerical approach.

The difference between computationally determined particle deposition fractions and the measured dust deposition fractions in Fig. 4-7 can now be explained by looking at impact locations of individual particle sizes in Fig. 4-11. The larger particles impacting far upstream have higher momentum and can bounce after initial impact to deposit in or closer to the sealing region and even downstream of the sealing region. Deposition in the sealing region is suspected to be mainly due to smaller particles, as these have lower momentum and are thus expected to bounce less.

Based on discussions with the project partner, it was initially suspected that larger particles ($\geq 0.040G_0$) are mainly responsible for dust deposition. From the analysis however, it is clear that the smaller particles ($0.010G_0 - 0.040G_0$) also contribute to dust deposition. Therefore, to reduce dust deposition in the sealing region, the

impact of smaller particles should be avoided or moved away from the sealing region. The best case scenario would be to avoid particle impacts completely, but due to the complexity of the geometry and flow pattern, this is not possible. It will be shown, however, that with some modifications to the valve geometry, the number of particles impacting in and around the sealing region can be reduced.

4.4   Valve Redesign Process

The self-sealing valve is redesigned based on insight gained from the assessment of the original design. The redesign is carried out while respecting constraints as imposed by the industrial partner, as follows:

1. The redesign must not involve any changes to the external valve casing to minimize the cost of the redesign. Therefore, all the changes are made locally near the sealing region.

2. The redesign must satisfy the minimum flow rate requirements in both the open/flow conditions while reducing the leakage flow in the closed/no flow condition.

The initial redesign process involved making modifications just upstream of the sealing region to change the flow field and particle paths. A number of different designs were compared both numerically and experimentally. Experimental assessment was carried out using the accelerated in-lab dust testing, as explained in section 4.2.2. Some of the designs considered showed great improvement in terms of leakage flow but failed to meet the minimum flow rate requirements due to increased losses. As a result, designs with changes made downstream of the sealing region were also studied with the aim of decreasing the overall loss coefficient.

The final design modifications are the result of a parametric study which had the aim of achieving the best possible combination of reduced leakage flow and maxi-

mization of the flow rates in the open/flow conditions. The next section discusses the modified design and its assessment using computational and experimental approaches.

4.5   Modified Self-Sealing Valve Design Description and Assessment

The modified self-sealing valve geometry includes two new parts: a "washer" added upstream of the sealing region, and an "exit wall" added downstream of the sealing region. The modified geometry is illustrated in Fig. 4-12.
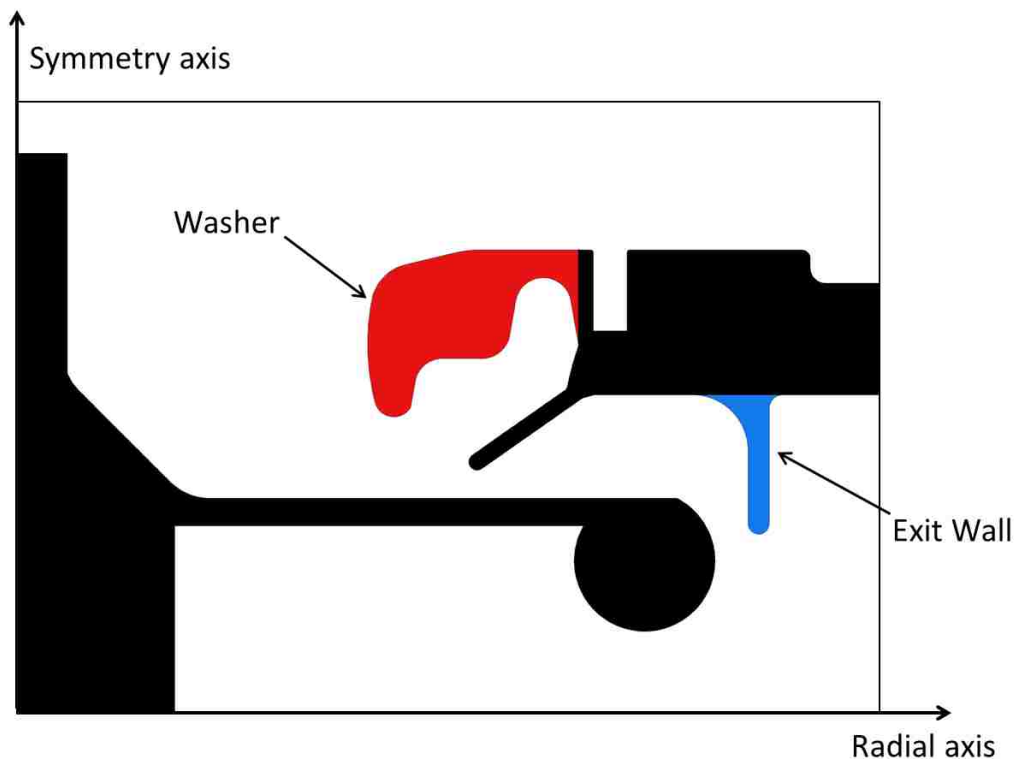
Figure 4-12: Modified geometry including washer and exit wall.

The purpose of adding the washer is to alter the particle paths so that they more closely follow the streamlines over a larger range of particle sizes. The undercut in the bottom side of the washer is to allow the seal to move freely. The inner radius

of the washer is 0.59 r^*, which provides the best balance from the parametric study between maximizing flow rate in the open valve state and minimizing leakage flow in the closed valve state.
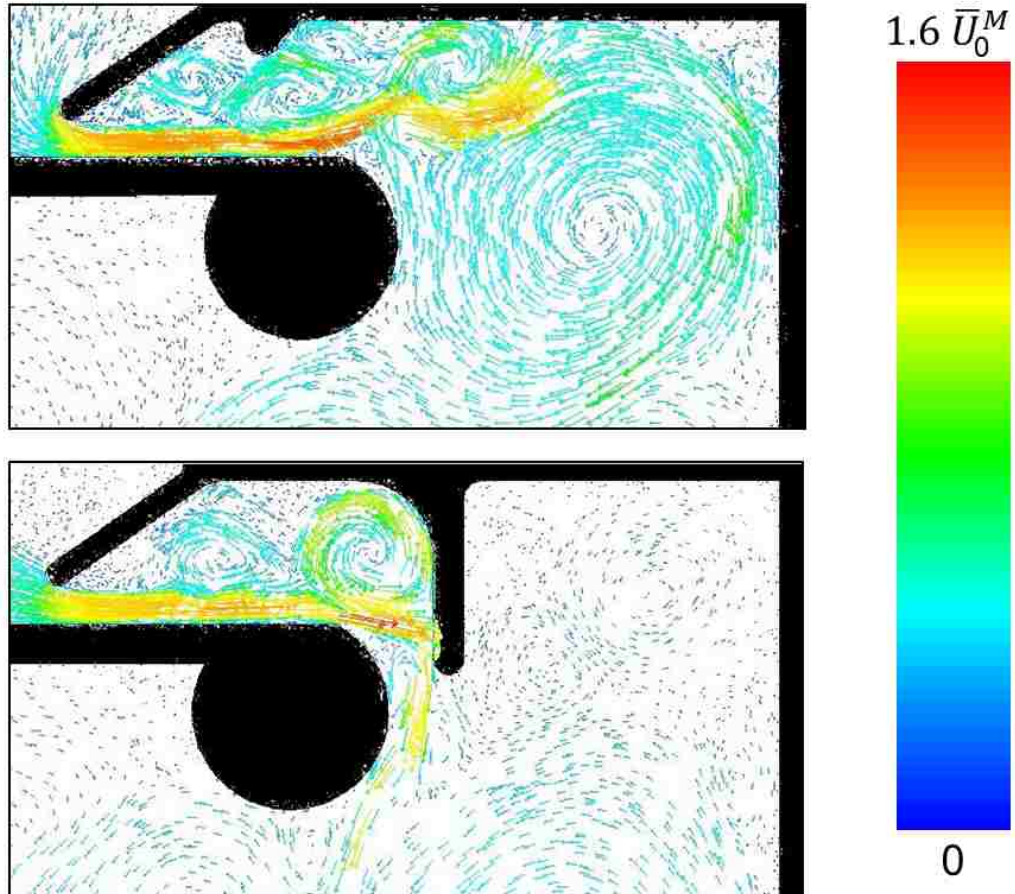
Figure 4-13: Velocity vectors showing reduction in re-circulation by addition of the exit wall.

Due to the introduction of the washer, the upstream flow area is contracted which results in increased flow losses. This prevented washer-alone designs from meeting the flow rate specifications. Therefore, loss-reduction strategies were employed to bring the flow rates back up to acceptable values. The most easily manufactured design change which resulted in acceptable flow rates is the introduction of an exit wall. This wall lowers losses by reducing the size of flow re-circulation zone downstream of

the sealing region. Figure 4-13 depicts the velocity vectors without (top) and with (bottom) the exit wall. The size of the recirculation is clearly reduced. The presence of the wall reduces the loss coefficient in "from environment" operation by 11%. The overall loss coefficient in both flow directions is reduced by 9%, compared to the washer-alone design.

4.5.1 Numerical Assessment and Comparison with Original Valve Geometry

A numerical investigation of the modified geometry indicates that particles of diameter up to $0.010G_0$ never impact the poppet surface. This can be seen in Fig. 4-14. The inset shows that the particles closest to the surface move parallel to it. The particles of the same size impact in the sealing region for the original self-sealing valve geometry (see Fig. 4-8).

Sealing Region
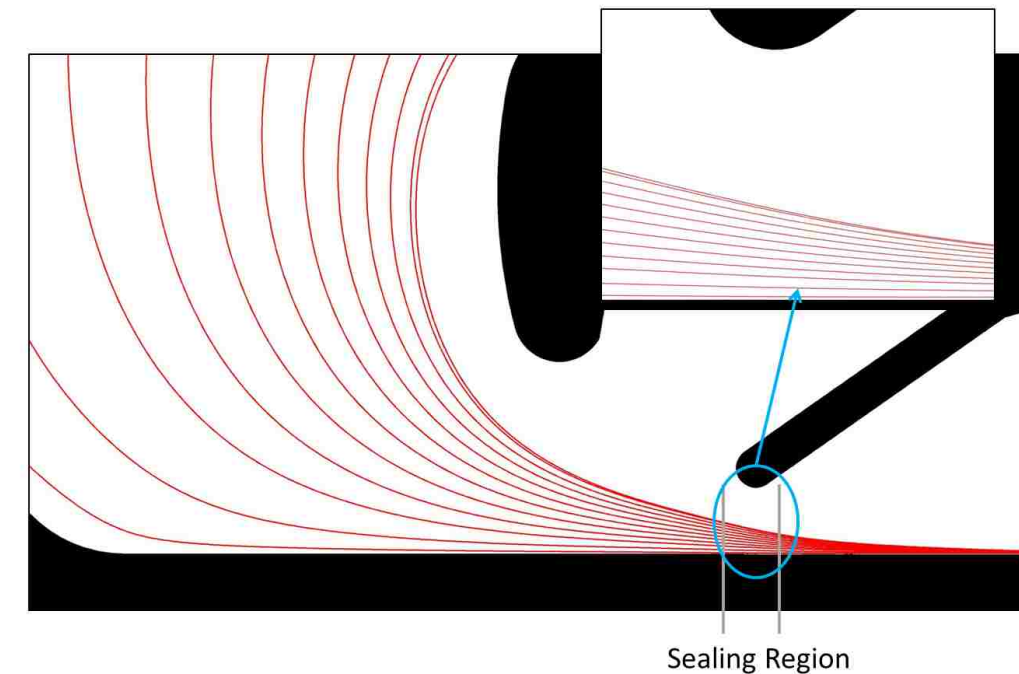
Figure 4-14: Predicted tracks of particles of diameter $0.010G_0$. Inset: no impact of particles on the poppet surface for modified geometry.

Particles of diameter $0.020G_0$ impact the poppet surface in the range $0.30 \leq r^* \leq 0.74$, which can be observed in Fig. 4-15. The radial range of these impacts is increased by approximately seven times compared to the original design. Since it has been determined that particles of this size are unlikely to bounce, moving some of the impacts away from the sealing region reduces the deposition in that critical area.

Sealing Region
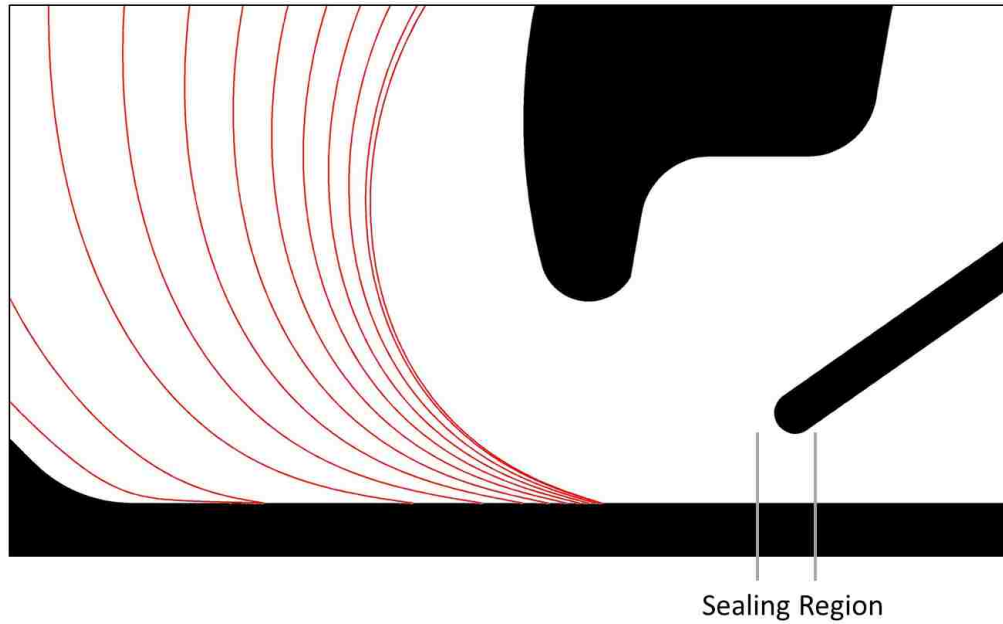
Figure 4-15: Predicted tracks of particles of diameter $0.020G_0$. Particle impacts are shifted upstream for the modified geometry.

Particles of diameter $0.040G_0$ impact the poppet surface at a maximum radial location of $r^* = 0.29$. This represents an approximately nine-fold increase in the distance between the poppet-seal contact point (sealing radius) and these particle impact locations compared to the original valve geometry, as depicted in Fig. 4-16. Particles of diameter $0.080G_0$ and similar sizes do not impact the surface in the region of interest.
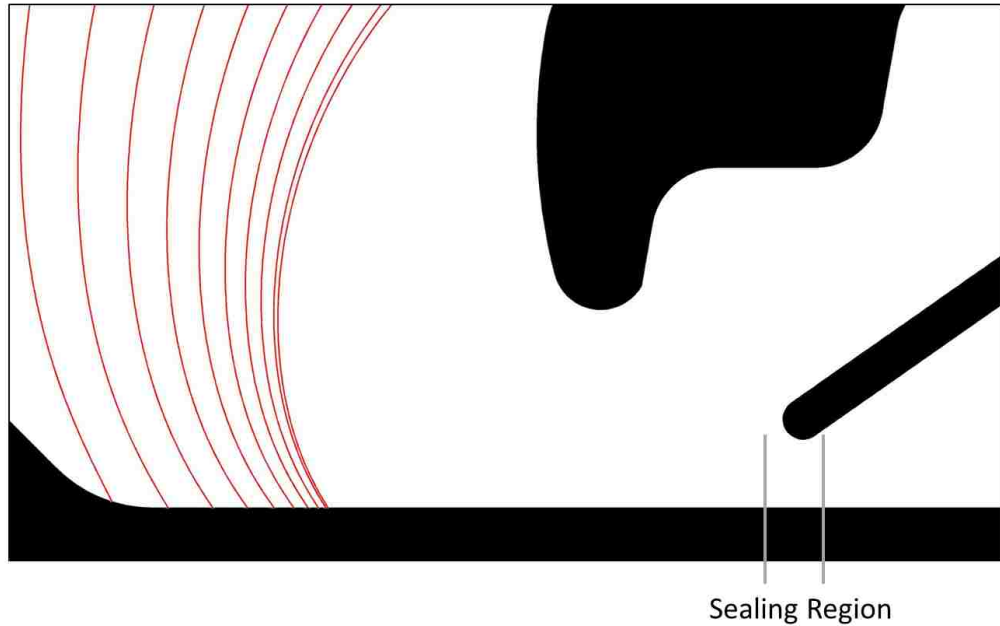
Figure 4-16: Predicted tracks of particles of size $0.040G_0$. Particles impact far upstream of the sealing region for modified geometry.

The introduction of the washer helps the smaller $(0.010G_0)$ particles follow the streamlines in the sealing region and pass through it without impacting the poppet surface. The washer also causes the larger particles $(0.040G_0)$ to deviate from the streamlines earlier than they did in the original valve geometry, forcing these particles to impact far upstream of the sealing region.

Based on the simplified computational approach, a 25% decrease in the total number of particles impacting the poppet surface is predicted for the redesign. Also, the fraction of particles impacting within the sealing region is reduced to 1/3 of the value for the original valve design. In the radial interval just before the sealing region $(0.7 \leq r^* \leq 0.9)$, the fraction of impacts is reduced by a factor of 10. A seen in Fig. 4-17, particle impacts are shifted upstream, with approximately 60% of the particles impacting before $r^* = 0.3$. Some of the small particles $(0.015G_0)$ impact downstream of the sealing region. Thus, by reducing the number of impacts in and around the

sealing region, it is expected that the modified geometry will have less deposition in this region than the original geometry. The total amount of dust deposited is also expected to be reduced.

In Fig. 4-17, the contribution to the dust deposition is seen to be from dust sizes between diameters of $0.015G_0$ and $0.050G_0$. Particles smaller than $0.015G_0$ never impact the poppet surface. Particle greater than $0.050G_0$ in diameter impact the poppet surface outside the domain of interest, i.e. $r^* < 0$. These particles, although impacting in the region of ribs as shown in Fig. 3-2, can still deposit in the region of interest, as suggested by the experimental results in Fig. 4-18.
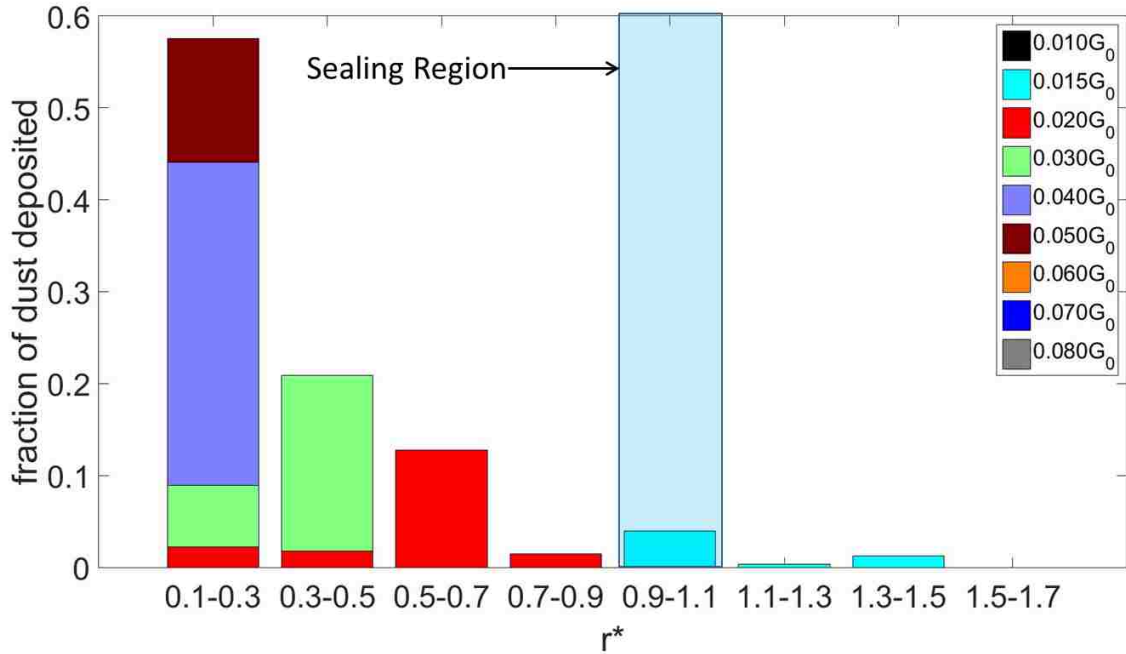
Figure 4-17: Prediction of contribution of individual particle sizes to total dust distribution in modified valve geometry using simplified numerical approach.

4.5.2 Experimental Assessment and Comparison with Original Valve Geometry

The experimental assessment of the modified self-sealing valve design is conducted using the same three experiments employed for the original self-sealing valve design. The flow rate in the open state and the leakage flow in the closed state are given in Table 4.4. The results indicate that:

1. Flow margins are either maintained or only slightly reduced compared to the original self-sealing valve design. Thus, the modified geometry satisfies the minimum flow rate specification constraints.

2. The modified self-sealing valve with the washer and exit wall exceeds the leakage flow specification by a wide margin, with leakage flow reduced by up to 93% when compared to the original valve design.

The underlying reason for a lower leakage flow is the reduction and redistribution of deposited dust in the modified valve design. The numerical and experimental dust deposition results are plotted together for the modified design using the post-processing approach explained earlier in Fig. 4-18. The measured experimental dust deposition indicates a more uniform radial distribution of dust deposited on the poppet surface compared to the experimental dust deposition for the original geometry shown in Fig. 4-7. The fraction of dust deposited in the sealing region is reduced from 0.30 to 0.15 for the tangential inlet variant and from 0.25 to 0.13 for the radial inlet variant. This corresponds to a reduction of $> 50\%$ of the dust supplied at inlet depositing in the sealing region for both these cases. The hypothesized correlation between the amount of dust deposited in the sealing region and the leakage flow rate, which is the basis for the redesign, is corroborated by these results.

Table 4.4: Flow rate and leakage flow test results for modified design.

Flow condition/direction	Tangential flow inlet			Radial flow inlet		
	$\dot{m}/\dot{m}_0$	Specification pass/fail	Margin of pass/-fail	$\dot{m}/\dot{m}_0$	Specification pass/fail	Margin of pass/-fail
Open/ to environment	-6.41	Pass	3.1%	-9.40	Pass	51.1%
Open/ from environment	4.05	Pass	53.4%	5.53	Pass	109%
Closed/ from environment	7.23×10^{-5}	Pass	60%	5.19×10^{-5}	Pass	71.6%

The numerical simulations indicate that a large number of particles impact close to the axis of poppet due to the introduction of the washer. These particles can bounce, roll or slide and deposit in the subsequent radial intervals, as the experiments suggest.

4.6   Limitations of the Simplified Modelling Approach

In the simplified numerical approach it was assumed that the particles deposit at the surface immediately after first impact, as the built-in capabilities of the commercial software used for the analysis restricted the ability to accurately predict post-impact particle trajectories. As a result, as shown in Figs. 4-7 and 4-18, there is no and very little dust deposition predicted by the computations downstream of the sealing region

for the original and modified valve designs, respectively. Nevertheless, in the same figures, it is observed that a significant amount of dust is found in this region in the experiments. A similar trend but with opposite dust behaviour is seen for the region upstream of the sealing region. Thus, the simplified model is not able to capture the dust deposition trends, but it accurately predicts particle trajectories up to the first impact location. To enhance the prediction of dust deposition locations, the numerical model needs to be modified to include the post-impact particle behaviour. This is accomplished via a UDF which modifies the particle trajectory calculations in Fluent. This advanced numerical model is explained in detail and assessed in the next chapter.
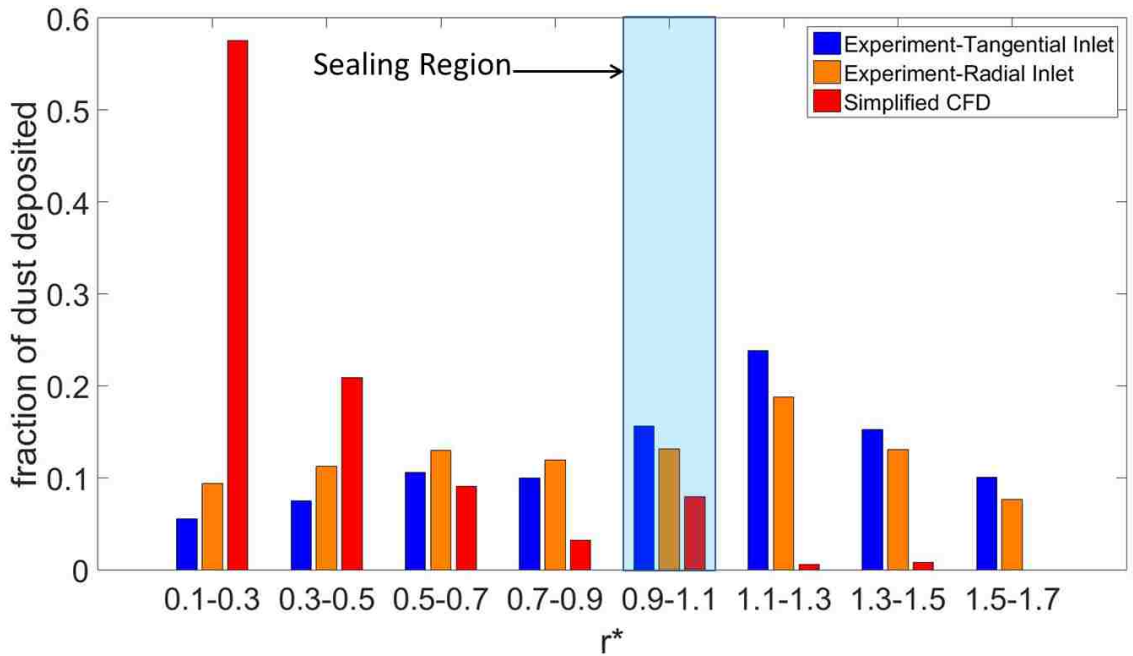
Figure 4-18: Radial distribution of numerically predicted initial particle impacts and experimentally measured dust deposition for the modified valve design.

Chapter 5

Advanced Numerical Modelling and Experimental Calibration

This chapter explains the advanced numerical modelling capabilities, employed by linking a UDF (C code) to Fluent. A simplified geometry, also discussed in this chapter, is used to calibrate the model. The accuracy of the model is assessed after it is calibrated. Finally, the advanced numerical model is applied to the original and modified self-sealing valve geometries to gain additional insight into the post-impact behaviour of particles in the self-sealing valve.

5.1 Advanced Deposition Model

The advanced deposition model enhances the built-in capabilities of Fluent to predict the particle trajectories beyond initial impact by taking into account the particle-wall interactions mechanism explained in section 2.2. The UDF is programmed using built-in macros in Fluent [27]. The advanced deposition model is programmed using the C language and the code is included in appendix **F.**

Fig. 5-1 schematically represents the steps involved in the calculation of post-impact particle trajectories. The UDF replaces the default boundary conditions such

as "reflect," "escape," or "trap." Once the particles are released from the inlet, the UDF executes when a particle impacts the surface. If the particle impacting on the surface has a normal impact velocity lower than the capture velocity, the particle sticks to the surface. Whether or not particles stuck to the surface come to rest or continue to move along the surface is determined as described in the next paragraph. Otherwise, the particle bounces and continues its trajectory in the flow field but with reduced rebound velocity, which depends on the coefficient of restitution (C.O.R.) between the particle and impact surface. Information about the particles that deposit on the wall surface are stored in memory using User Defined Memory Locations (UDML) and exported through a text file. This includes particle ID, particle diameter, particle mass, drag force acting on the particle, moments due to drag force and adhesion force, normal velocity of particle, capture velocity, critical wall shear velocity, and Cartesian coordinates of the impact location.

For the particles that stick to the surface upon impact, their subsequent behaviour must be determined. Whether the particle detaches and re-suspends in the flow, rolls, or slides is determined, as explained in section 2.2 Therefore, if eq. 2.18 or eq. 2.19 are satisfied, particles are able to continue their trajectory in the flow. Those particles which come to a complete stop are considered "deposited" particles and their details are stored using UDML (see preceding paragraph). Thus, the UDF generates another text file which include information about particle ID, particle diameter, particle mass, drag force acting on the particle, moments due to drag force and adhesion force, normal velocity of particle, capture velocity, critical wall shear velocity, and Cartesian coordinates of the deposition locations.

The known input parameters for the model are: material properties for the particle and surface such as Young's modulus, Poisson's ratio, the density of the particle, and the coefficient of static friction; and the fluid density and viscosity. Normal and tangential C.O.R. are two unknown input parameters and are determined from the

calibration process.
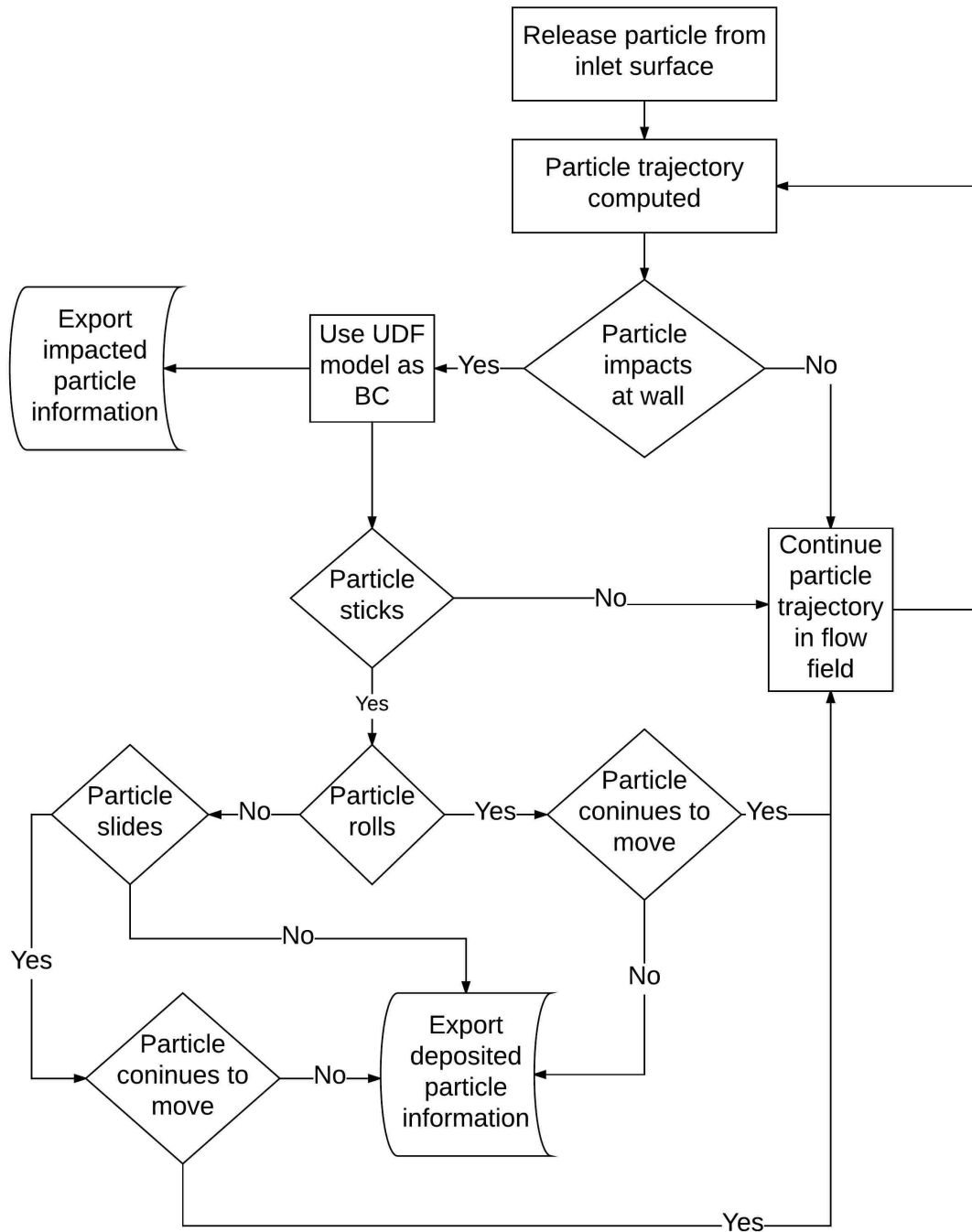
Figure 5-1: Logic flow for the advanced particle deposition model.

5.2 Simplified Geometry for Calibration of Advanced Numerical Model

Two components of C.O.R., a normal C.O.R. and a tangential C.O.R. play important roles in determining post-impact particle trajectories. There is no information available regarding the values of these coefficients for the dust used for analysis and a smooth surface of impact such as the poppet. To test the validity of the advanced deposition model and find the best combination of C.O.R components for the dust and surface material, a simplified geometry with a 90° bend and a rectangular cross-section is designed and analyzed using the advanced numerical method and dust-deposition experiments. The geometry is depicted in Fig. 5-2. The height of the channel is H and the width is $4H$. The stream-wise distance from inlet to outlet is $41.4H$. The channel is symmetric about a vertical plane as indicated in Fig. 5-2.

5.2.1 Computational Setup

The numerical analysis of the simplified geometry (Fig. 5-2) is conducted using symmetry and an incompressible, 3D pressure-based solver in ANSYS Fluent 15.0 [1]. A virtual inlet plenum is used upstream of the channel inlet to obtain the correct inlet streamline pattern. The transition from the inlet plenum to the channel cross-section is made by using a bell mouth. At the numerical inlet boundary, atmospheric pressure is specified. The velocity, U_{avg}, is specified at the outlet to set the desired Reynolds number. The computational grid for analysis is generated using ANSYS Mesher [22] and consists of quadrilateral elements (fully structured). The grid has 2.6 million elements. The mesh density varies such that it is finest closest to the Waals and in the curved section and gradually coarsens towards the centre of the channel height and the symmetry plane, as well as towards the inlet and outlet regions. A mesh independence study showed insignificant changes in the key flow metrics upon further

grid refinement. These key metrics are pressure coefficients and loss coefficients at the channel outlet, and start and end of the curved section. The boundary layers are resolved so that $y^+ < 1$ along all boundaries.

The analysis is done at a Reynolds number of 900, which is close to the operating conditions of the self-sealing valve. A Reynolds number of 900 is selected instead of 600 (self-sealing valve) to allow particles to deviate from the streamlines and impact the surface. The flow field is computed using the $k - \omega$ shear stress transport [23] turbulence model. This turbulence model is used so that y^+ values can be accessed to be used in the UDF (y^+ is not computed by the solver for laminar flow solutions). As was determined in section 4.1, in this Reynolds number regime, the laminar and turbulent viscosity models generate the same flow field solution. The same numerical scheme is used as discussed in chapter 4. The numerical simulations are considered to be converged when all of the following quantities no longer change by more than 1%:

- Reynolds number at $10H$, $15H$, and $20H$ from the inlet;

- pressure coefficients at outlet, and start and end of the curved section; and

- loss coefficient from inlet to outlet, and to the start and end of the curved section.

In the curved section, significant secondary flows develop, as can be seen in Fig. 5-3. This is as expected due to the rotation of the boundary layer vorticity towards the streamwise direction. Zhang et al. [3] also found similar flow behaviour. At the start of the curve, the velocity vectors reveal no secondary flows. As the streamwise distance increases through the bend, the secondary flows grow. The end of the curved portion shows the strongest secondary flow pattern.
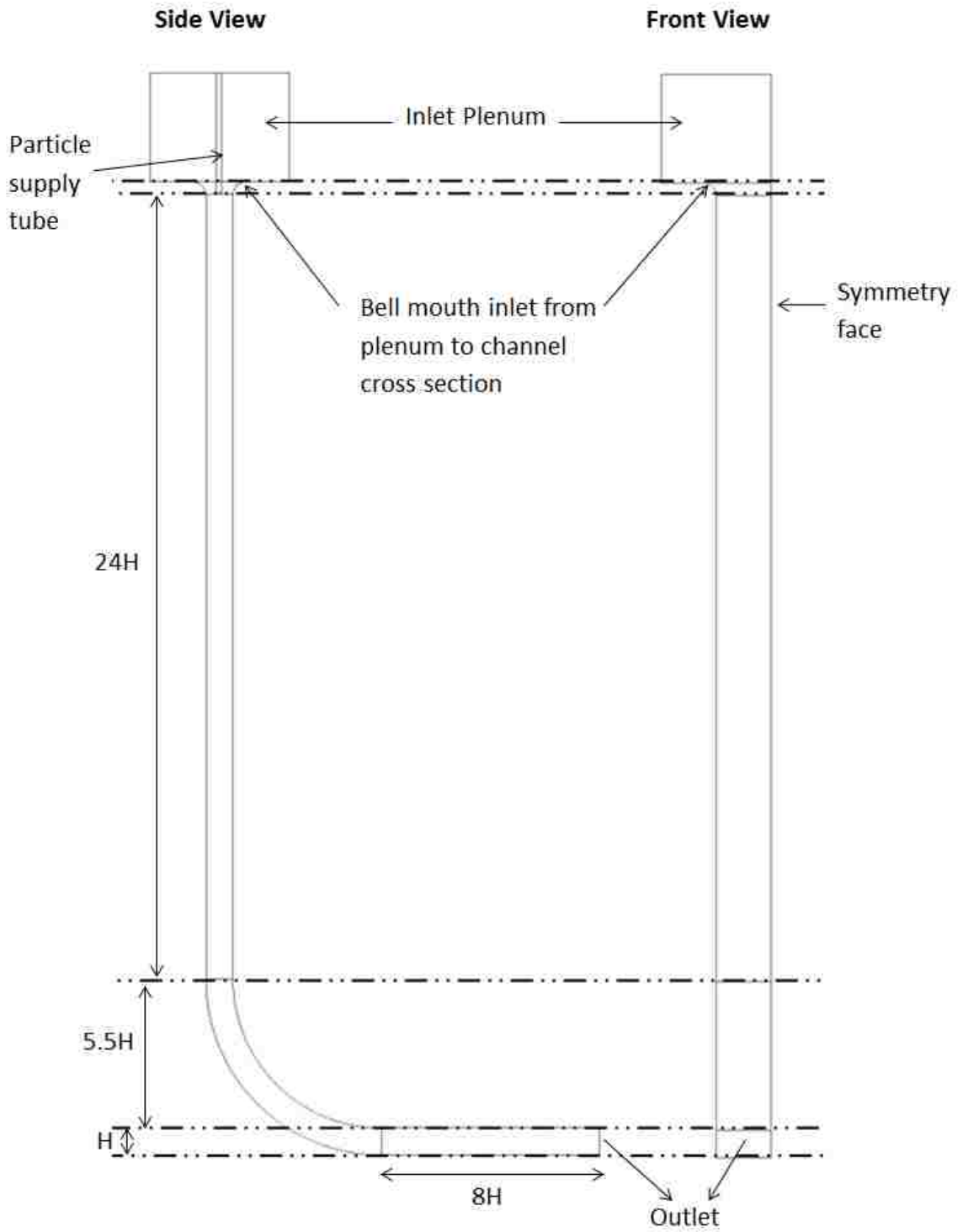
Figure 5-2: Side and front view of the simplified geometry.
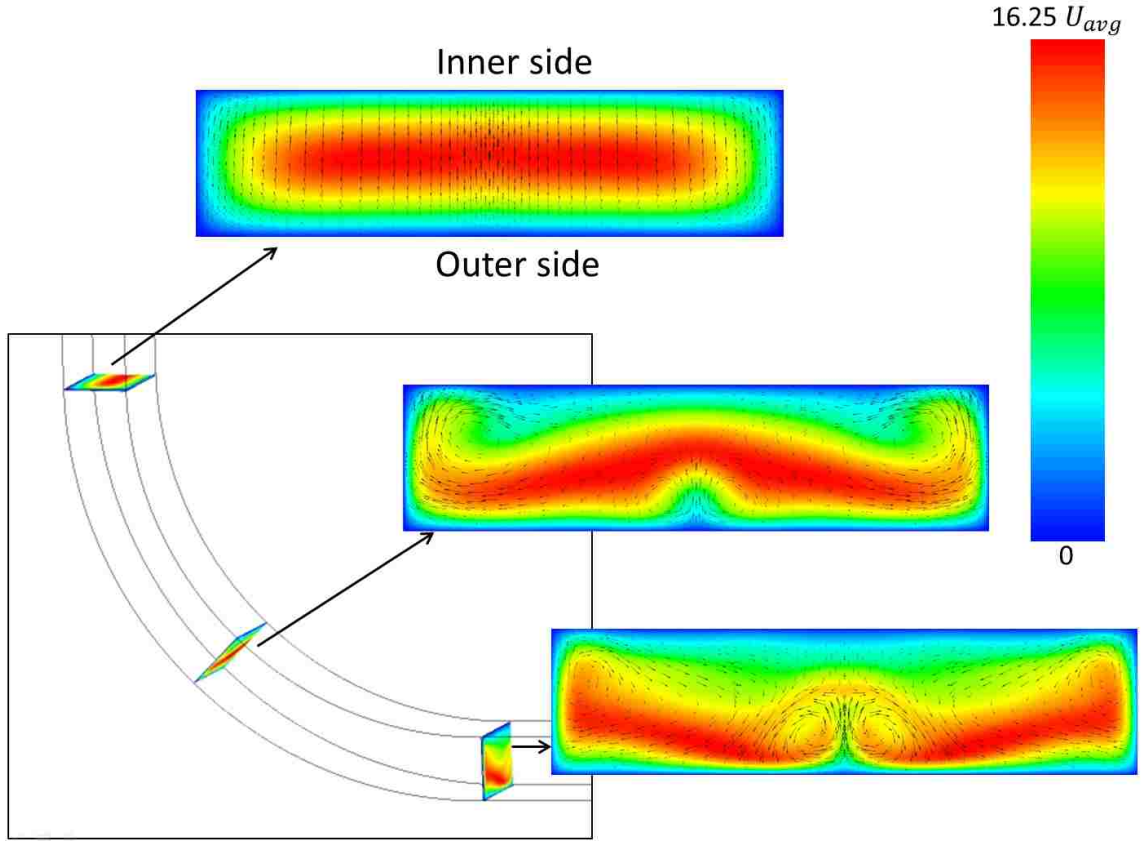
Figure 5-3: Velocity contours and vectors showing presence of secondary flow in the curved bend.

To simulate the particulate phase, the DPM is used. A description of DPM is given in detail in section 4.1.2. However, instead of using the built-in boundary conditions for particle-wall contact, the advanced model UDF (described in section 5) is applied. The particle diameters tested are in the range of $0.08G_0 - 0.16G_0$, where $H = 50G_0$.

5.2.2 Experimental Results and Comparison with Computations

The dust deposition experiment (section 4.2.2) is adapted for the simplified geometry described in section 5.2. Two sets of experiments are conducted, one for particle sizes in the range $0.08G_0 - 0.12G_0$ and another for particle sizes in the range $0.12G_0 -$

$0.16G_0$. Each experiment is repeated three times and the average values are compared with computational results. To enable the comparison, the post-processing approach (explained in section 4.2.3) is used, adapted to the altered geometry. The curved portion of the channel is divided into 9 equal arc length bands of 10° each. The downstream horizontal portion is also divided into 4 bands that have streamwise length equal to the arc length of the bands in the curved portion at bottom of the channel. The bands are depicted in Fig. 5-4. The dust in each band is expressed as a fraction of the total dust deposited in all the bands in a similar manner as was done for the dust deposited on valve poppets. Similar to the self-sealing valve analysis, the change in brightness matrix ($\Delta\bar{B}$) reflects the difference between the dust deposited in an image of the contaminated surface compared to the image when there is no dust on the same surface. The brightness values are averaged across the central $2H$ of the channel.
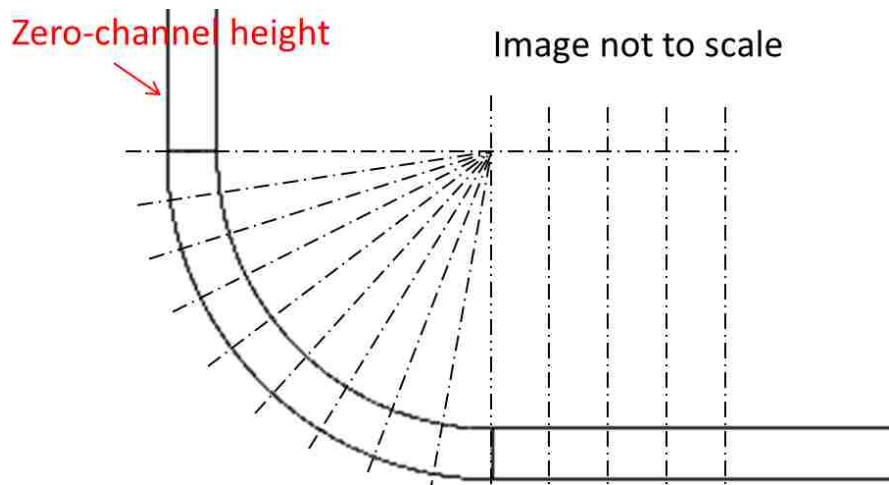
Figure 5-4: The simplified geometry divided into equal bands of streamwise distance at zero-channel height in the region where dust deposition is expected.

As the C.O.R. values are not known a prior for particle impacts on the wall surface, a number of different combinations of normal C.O.R. and tangential C.O.R. are tested in the computations. A relative comparison for the error between numerical

simulations with different C.O.R. combinations is carried out as follows. The value of Root Mean Squares (RMS) error is calculated using following the formula:

$$
\text{RMS error} = \left[\frac{1}{N} \sum_{i=1}^{N} \left(\frac{x_i^2}{\sigma_i^2} \left(1 - \left| \frac{y_i}{x_i} \right| \right)^2 \right) \right]_{0.08G_0 - 0.12G_0}
$$
$$
+ \left[\frac{1}{N} \sum_{i=1}^{N} \left(\frac{x_i^2}{\sigma_i^2} \left(1 - \left| \frac{y_i}{x_i} \right| \right)^2 \right) \right]_{0.12G_0 - 0.16G_0} , \qquad (5.1)
$$

where i is the band number, N is the number of bands, x_i is the fraction of dust deposited in each band experimentally, σ_i is the standard deviation from the three experimental trials for each band, and y_i is the fraction of dust deposition in each band as predicted by the computations.

The results of the analysis are presented in Table 5.1. Twelve different combinations of C.O.R. are tested and the best combination is determined to be the normal C.O.R.= 0.25 and tangential C.O.R.= 0.75. Reagle [28] developed a technique to measure the C.O.R for Arizona fine dust and found that the tangential component is larger than normal component, consistent with the results obtained here.

The computations carried out with the best combination of C.O.R. values yield results as shown in Figs. 5-5 and 5-6. The figures show both the experimental and numerically predicted dust deposition fractions in each band for particle diameter ranges of $0.08G_0 - 0.12G_0$ and $0.12G_0 - 0.16G_0$, respectively. The computational results are weighted based on the particle projected areas and the volume composition of the dust as previously described in section 4.1.3.

Table 5.1: Error Analysis for determining best combination of Normal and Tangential C.O.R.

Error Analysis		Normal C.O.R.			
		0.2	0.25	0.5	0.75
Tangential C.O.R.	0.25	-	26.12	25.80	26.79
	0.5	-	25.92	21.91	25.86
	0.75	25.98	**17.97**	19.95	26.28
	0.8	23.45	25.83	-	-

For the particle size range of $0.08G_0$ and $0.16G_0$, the three bands with the highest dust distribution fractions are accurately predicted computationally. The computations predict 60% of the total dust deposited to be within the $30° - 60°$ bands in the curved portion of the channel. In the experiments, the $30° - 60°$ bands contain 55% of the total dust deposited. In the horizontal portion of the channel, the computations over-predict the dust deposited compared to the experiments. In the three attempts to repeat the experiment, the highest uncertainty is for the "Flat2" and "Flat3" bands. It is suspected that this may be due to the presence of strong secondary flows towards the end of the curved section. In the experiments, most of the dust deposition occurs near the symmetry plane, with maximum deviation from the symmetry plane of $0.51H$. However, dust is not deposited perfectly symmetrically.
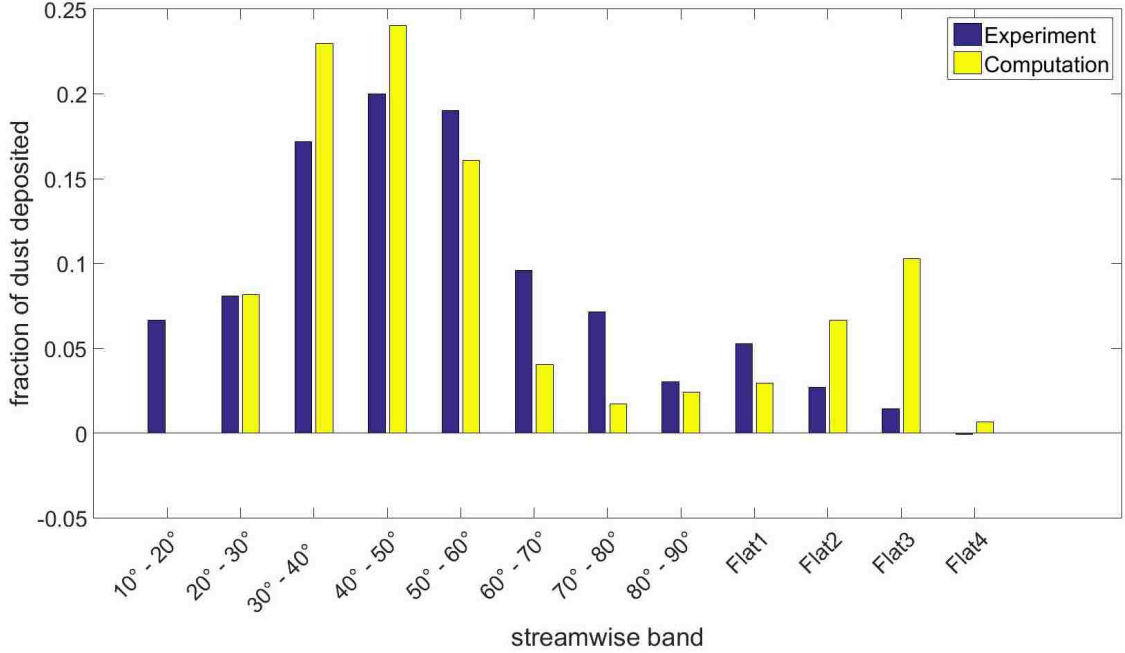
Figure 5-5: Distribution of numerically predicted and experimentally measured dust deposition for bands of equal streamwise distance. Particle diameter range is $0.08G_0 - 0.12G_0$.

Dust deposition experiments conducted for the $0.12G_0 - 0.16G_0$ particle diameter range also show that most deposition occurs in the $30° - 60°$ bands, with 86% of the total dust depositing in this region. The computations predict 85% of the total dust deposition in this region. Hence, the computations are able to predict dust deposition accurately. No dust deposition is predicted beyond the $60°$ band. The maximum deviation of dust from the symmetry plane is $0.56H$.

For both the particle size ranges, the computations accurately capture the trends of dust deposition seen in the experiments.

In Figs. 5-5 and 5-6, some bands show a negative fraction of dust deposited experimentally. These values are well within the range of the uncertainty of the image comparison post-processing method. The precision uncertainty calculated for this geometry is 0.38% of FSR brightness level. The calculation procedure is shown
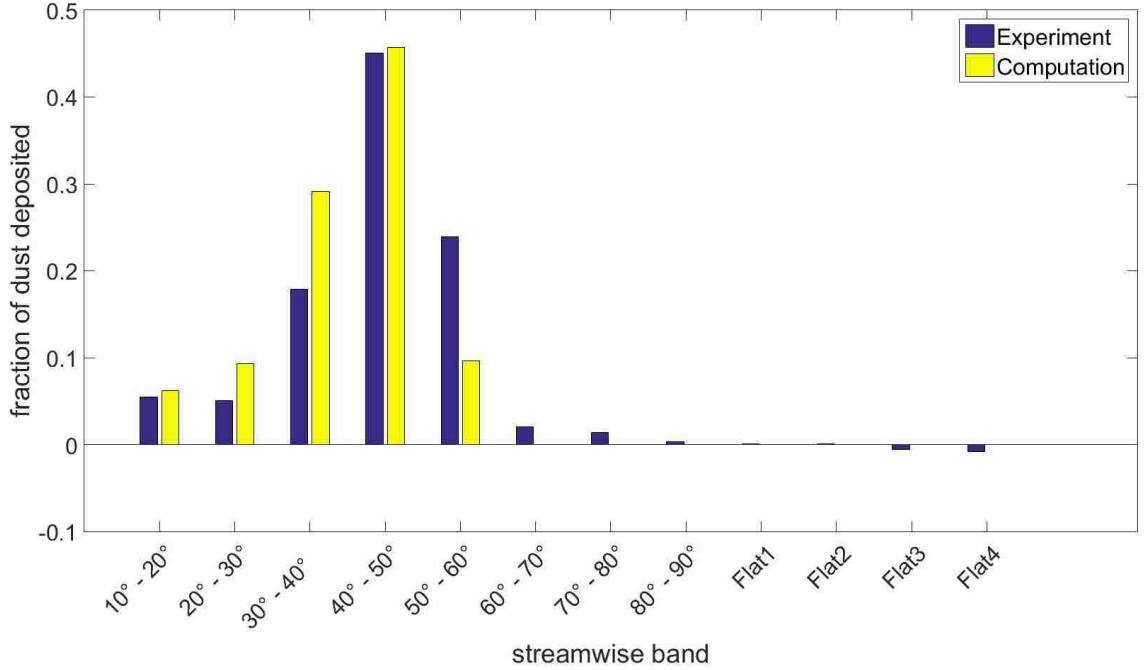
Figure 5-6: Distribution of numerically predicted and experimentally measured dust deposition for bands of equal streamwise distance. Particle diameter range is $0.12G_0 - 0.16G$.

in appendix E.5.

5.2.3   Confidence Interval Analysis

To quantify the agreement between numerically predicted and experimentally measured dust deposition, confidence interval analysis is conducted using the Student's t-test. A value of Student's t for the experimental sample size is selected for different confidence levels. Then the confidence interval, Δ_i, is calculated by using the following formula [29]:

$$\Delta_i = \frac{t\sigma_i}{\sqrt{m}} \tag{5.2}$$

where t is the value of Student's t, σ_i is the standard deviation for each band, and $m = 3$ is the number of times the experiment is repeated.

The confidence interval is represented as a fraction of the computationally-predicted dust deposition (y_i) for both the particle diameter ranges shown in Fig. 5-5 and Fig.

65

5-6 averaged based on the square root of mean squares, as follows:

$$\frac{\Delta_i}{y_i} = \sqrt{\frac{1}{2}\left(\left[\left(\frac{\Delta_i}{y_i}\right)^2\right]_{0.08G_0-0.12G_0} + \left[\left(\frac{\Delta_i}{y_i}\right)^2\right]_{0.12G_0-0.16G_0}\right)} \tag{5.3}$$

In Fig. 5-7, this RMS value of Δ_i/y_i is plotted against the streamwise distance (SD) non-dimensionalized by channel height (H) for a different number of bands n. A smaller number of bands means that the computed dust deposition fraction is averaged over a larger streamwise distance for each band.
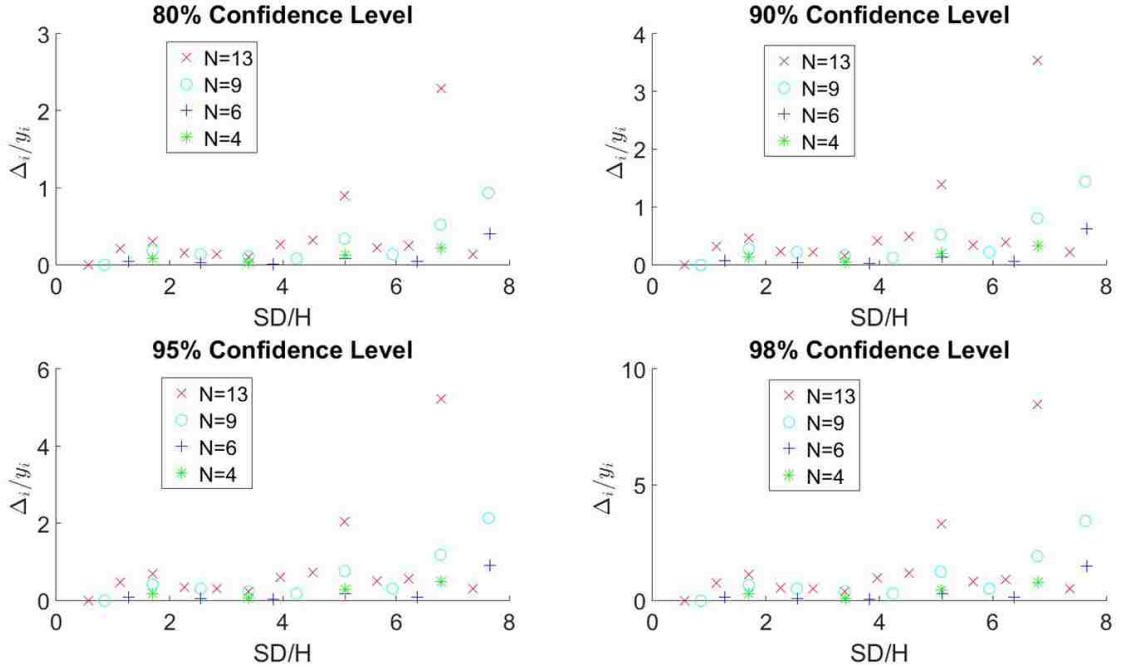
Figure 5-7: Normalized confidence interval (Δ_i/y_i) plotted against normalized stream-wise distance (SD/H). n is the number of bands.

The confidence interval fractions in Fig. 5-7 are averaged using room mean squares analysis, using the formula:

$$\overline{\left(\frac{\Delta}{y}\right)}_{RMS} = \sqrt{\frac{1}{N}\sum_{i=1}^{N}\left(\frac{\Delta_i}{y_i}\right)^2} \text{ and,} \tag{5.4}$$
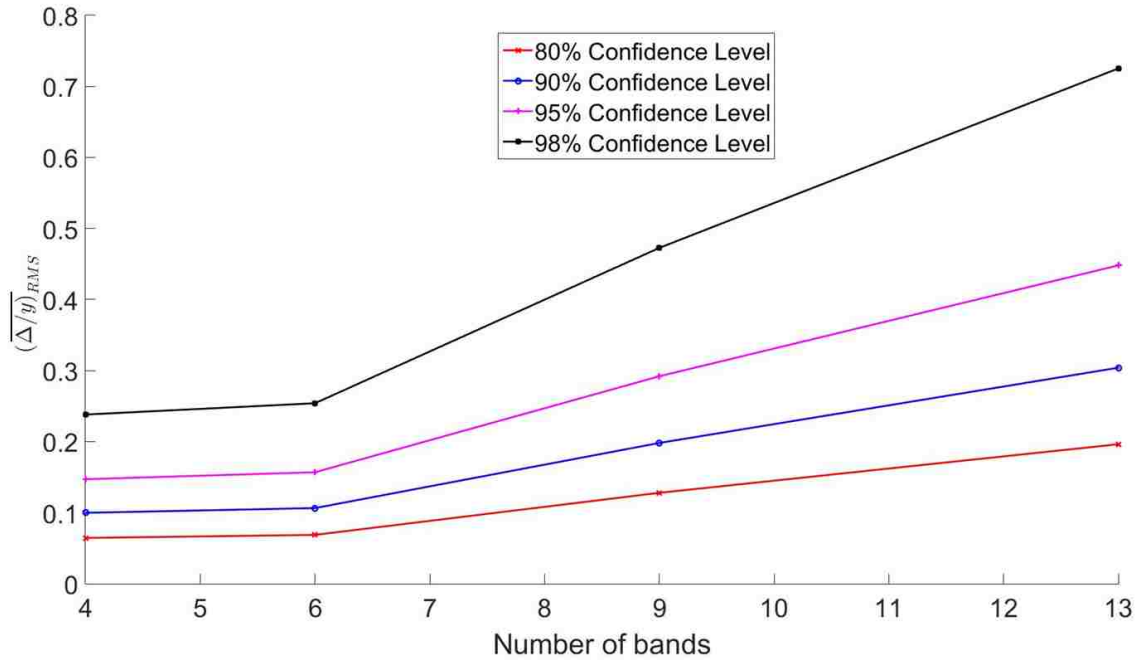
Figure 5-8: Confidence interval as a fraction of predicted dust deposition for different confidence levels.

the results are shown in Fig. 5-8 as a function of the number of bands. As the number of bands increases, the confidence interval also increases with increasing confidence level.

For the results presented in Fig. 5-5 and Fig. 5-6, where $N = 13$, it can be said that on average there is 80% confidence that the experimental dust deposition values will lie within 15% of the predicted computational dust fraction; or 90% confidence that experimental values will lie within 25% of the predicted value. If the streamwise distance is represented by only 4 bands, a 98% confidence level is achieved to predict that experimental values within 25% of the computational value. There is thus a trade-off between confidence level and the number of bands (precision of prediction location).

5.3 Datum Self-Sealing Valve Analysis with Advanced Numerical Model

In this section, the advanced numerical model is applied to the original valve, and the results are compared with the experimental data presented earlier in chapter 4.

5.3.1 Advanced Numerical Model Results

The advanced numerical model for deposition prediction, using the UDF as the particle-wall interaction boundary condition, is used with the flow field solution for the self-sealing valve original geometry. The best C.O.R. combination determined for the simplified 90° bend geometry is used in the UDF for the self-sealing valve analysis. The particle tracks are regenerated for the particle sizes of interest. The results are presented in exactly the same way as those from the simplified approach, but the advanced model results include the effect of bouncing, rolling, and/or sliding of particles after initial impacts with the poppet.

Figure 5-9 illustrates the particle tracks of the $0.010G_0$ diameter particles. All the particles impact in the sealing region with impact angles between 1° and 32°. The particles impacting with low angles have lower normal velocity. Thus, these particles deposit in the sealing region upon first impact as their normal velocity is lower than the capture velocity. Approximately 30% of the total particles supplied at this size deposit on the poppet surface, 95% of those in the sealing region. The particles impacting the surface with a high impact angle are able to bounce and continue their trajectory, remaining suspended in the flow well past the sealing region.
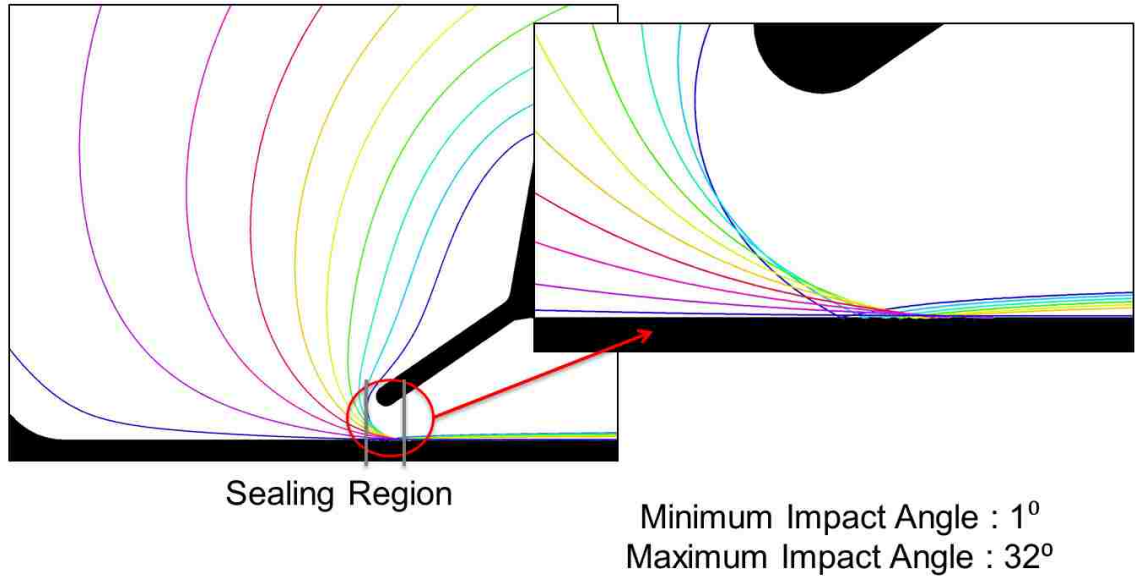
Figure 5-9: Predicted tracks of particles of diameter $0.010G_0$ using advanced numerical modelling. Inset: particles impacting with low normal velocities deposit in the sealing region.

Fig 5-10 shows the particle tracks of $0.040G_0$ diameter particles. These particles impact the poppet surface over a wide range of impact angles, ranging from $14°$ to $62°$. Most of the particles bounce after the first impact but with a lower rebound velocity than their impact velocity. Approximately 10% of the particles deposit at the first impact. 45% of the total particles deposit on the poppet surface, including particles depositing after subsequent impacts. The deposition of particles is spread over the entire poppet surface.

Minimum Impact Angle : 14⁰
Maximum Impact Angle : 62⁰

Sealing Region
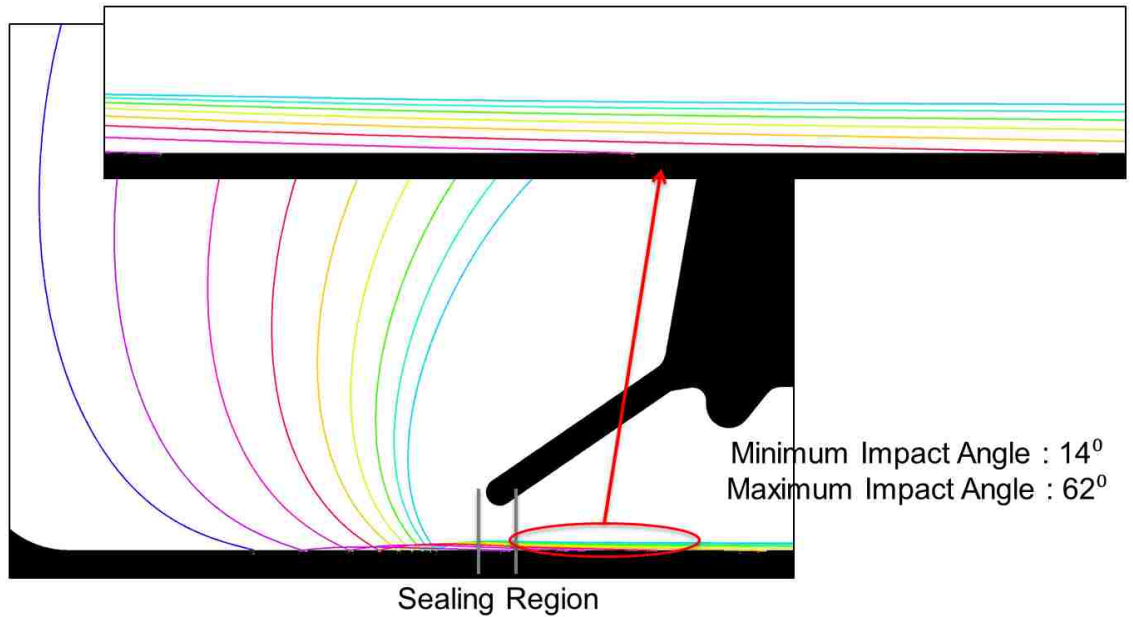
Figure 5-10: Predicted tracks of particles of diameter $0.040G_0$ using advanced numerical modelling. Particles impact the surface with a wide range of impact angles.

Fig. 5-11 depicts the predicted tracks of $0.080G_0$ diameter particles, impacting at very high angles and thus, high normal velocities. None of these particles stop at the first impact, as the normal velocity exceeds the capture velocity. Similar to the $0.040G_0$ particles, these particles impact the poppet surface upstream and downstream of the sealing region multiple times. Due to the combination of the flow being accelerated in the sealing region and the high initial impact velocities of these particles, none of the $0.080G_0$ diameter particles deposit in the sealing region. They do deposit upstream and downstream of the sealing region.
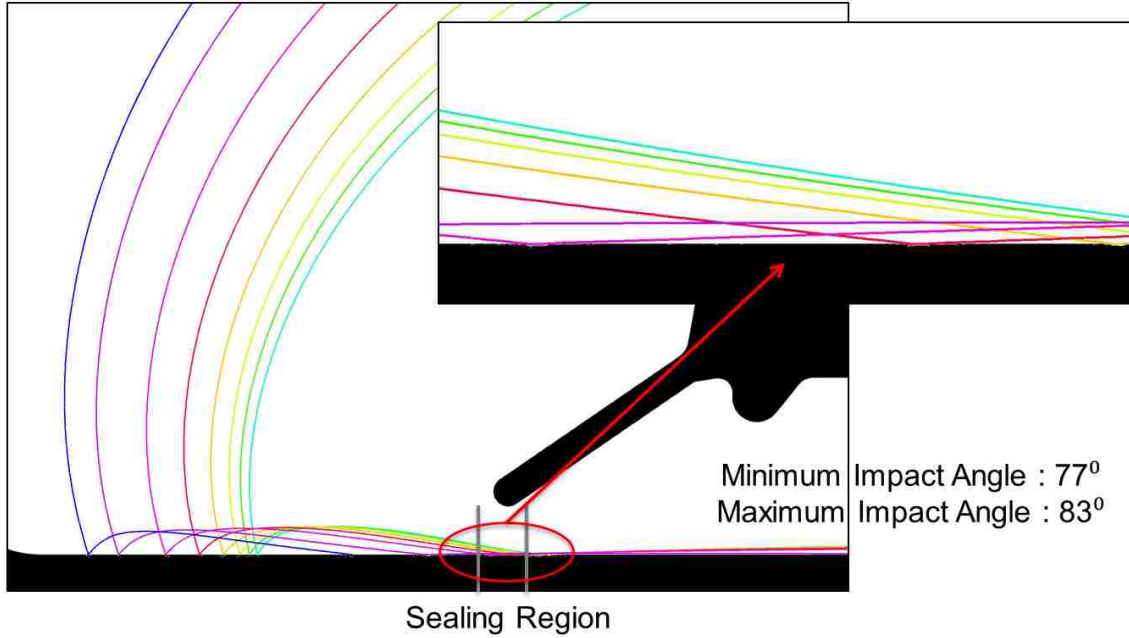
Figure 5-11: Predicted tracks of particles of diameter $0.080G_0$ using advanced numerical modelling. Inset: particles that impact in the sealing region bounce rather than deposit.

Fig. 5-12 quantifies the contribution of individual dust sizes to the total dust distribution predicted by the computations. The same weighting scheme applied to the results from the simplified numerical approach is used. As the particle tracks suggest, most of the dust deposition in the sealing region is due to the small particles, i.e. the particles $\leq 0.020G_0$ in diameter. These particles contribute approximately 50% of the dust deposited in the sealing region. Particles greater than $0.060G_0$ in diameter are predicted to deposit outside the sealing region. Overall dust deposition on the poppet is predicted to be dominated by mid-sized particles, i.e. those of approximate diameter $0.040G_0$.
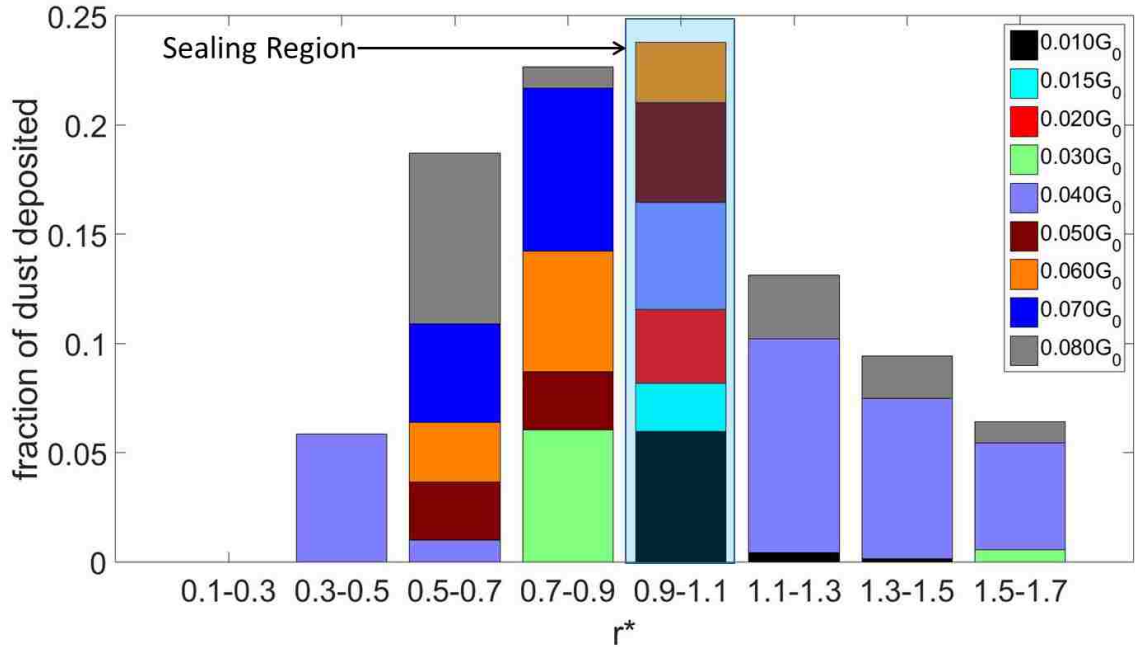
Figure 5-12: Prediction of the contribution of individual particle sizes to total dust deposition on the poppet surface for the original valve geometry. Particles $\leq 0.020G_0$ contribute to approximately 50% of the dust deposition in the sealing region.

5.3.2 Comparison of Advanced Numerical Modelling Results with Experiments

The prediction of dust deposition using the advanced numerical model is compared with the experimental dust deposition patterns for the original valve geometry in Fig. 5-13. The experimental results are those discussed in section 4.3.1. With the enhanced modelling capabilities, the particles can now be tracked until they come to rest and hence, dust deposition is predicted to occur over the entire poppet surface (unlike the simplified modelling, where there is no dust deposition predicted beyond the sealing region). Both the advanced numerical model and experiments conducted on the two inlet geometries show high dust deposition in the sealing region. The overall dust deposition trend is also accurately captured by the advanced numerical model. The

numerical model predicts 60% of the total dust to deposit in and around the sealing region (i.e. $0.7 \leq r^* \leq 1.3$). 61% and 65% of the total dust deposited in this region, for the radial and tangential inlet cases, respectively, is observed experimentally.

The differences between the predicted and actual dust deposition in some regions can be explained by the fact that the experimental dust deposition results are from the field test with natural dust and no filter at the inlet, yielding a continuous distribution of dust sizes deposited on the surface. In the computations, only particles up to $0.080G_0$ in diameter are used. The numerical dust deposition prediction is made by weighing the discrete particle sizes based on their projected area and volume composition as before.
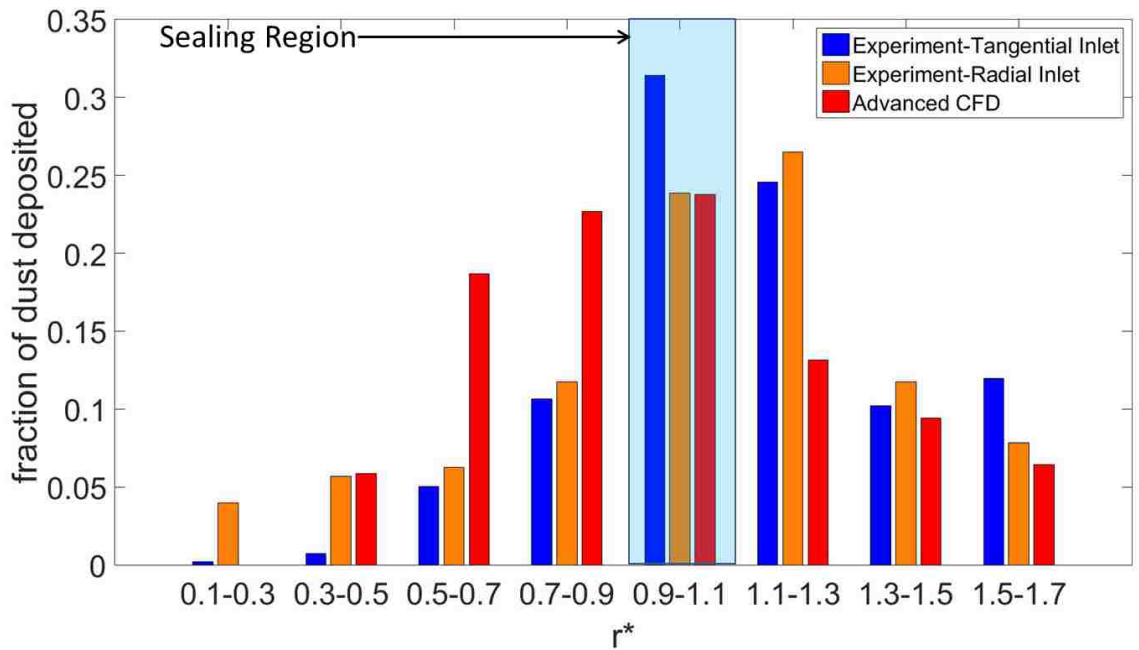
Figure 5-13: Radial distribution of numerically predicted and experimentally measured dust deposition in the original valve geometry. Numerical prediction is based on advanced deposition modelling.

From the analysis of the original valve geometry using the simplified numerical modelling, it did not prove possible to clearly identify the mechanism for the dust

deposition. The simple model did indicate that spreading out the particles impacting in and near the sealing region helps to reduce dust deposition in the sealing region. Although this is partially true for the small particles ($0.010G_0$) impacting and depositing in the sealing region upon first impact, the main mechanism responsible for dust deposition is the particles striking the surface with a low normal velocity at a low impact angle. Thus, to reduce the dust deposition, nearly tangential impacts for particles of any size should be avoided.

5.4 Modified Self-Sealing Valve Analysis with Advanced Numerical Model

In this section, the advanced numerical model is applied to the modified valve, and the results are compared with the experimental data presented earlier in chapter 4.

5.4.1 Advanced Numerical Model Results

To gain additional insight into the particle behaviour in the modified valve, particle tracks are generated using the enhanced deposition model with the original flow field solution. The simplified numerical analysis using the built-in DPM approach determined that $0.010G_0$ diameter particles never touch the seal and are able to pass through the sealing region as shown in Fig. 4-14. Therefore, the advanced numerical model did not change particle tracks for this particle size since only post-impact behaviour is affected.

Figures 5-14 and 5-15 illustrate the particle tracks of $0.040G_0$ and $0.080G_0$ diameter particles, respectively. Some of the $0.040G_0$ and all of the $0.080G_0$ diameter particles impact on top of the ribs (shown in Fig. 3-2). These ribs are outside of the domain of interest as $r^* = 0$ is at the start of the flat surface. The axisymmetric numerical model assumes the presence of ribs at every circumferential angle. In re-

ality, these ribs only cover approximately 40% of the circumferential area. Particles impacting on the flat surface between the ribs are expected to impact the surface at angles closer to 90° and bounce with a higher rebound velocity, which decreases the likelihood to deposit upon subsequent impact.

The particles of diameter $0.040G_0$ which impact in the domain of interest all impact at an angle of approximately 60°. In the original geometry, these particles impact over a wide range of angles from 14° to 62°. Therefore, in the modified geometry, the particles of the same size impact with a higher normal velocity than in the original geometry which decreases the likelihood that they will deposit since the rebound velocity is greater. Some of the $0.040G_0$ diameter particles subsequently deposit in the vicinity of the sealing region. A similar behaviour is seen with the $0.080G_0$ diameter particles which deposit in and around the sealing region after three or more impacts.
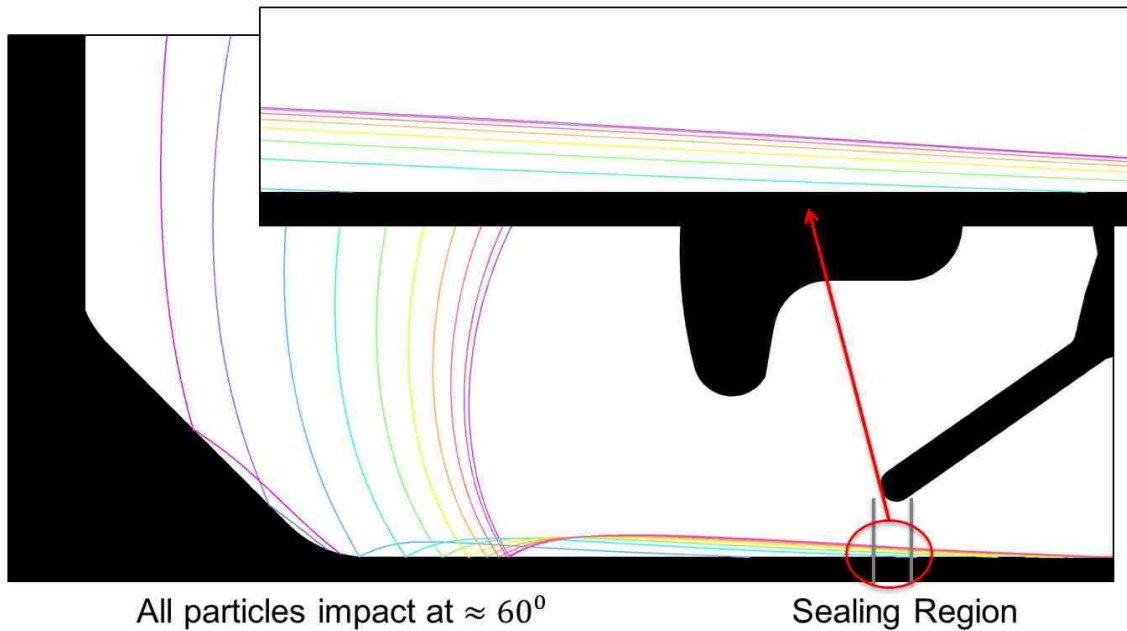
Figure 5-14: Predicted tracks of particles of diameter $0.040G_0$ using advanced numerical modelling. Inset: some particles deposit in the vicinity of sealing region.
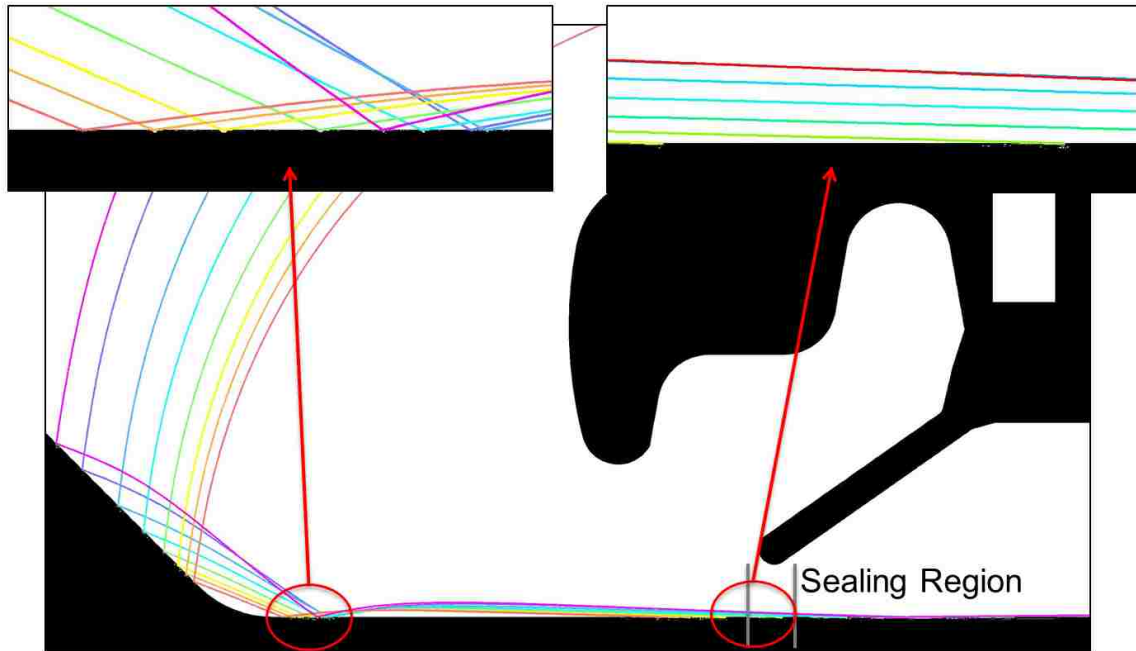
Figure 5-15: Predicted tracks of particles of diameter $0.080G_0$ using the advanced numerical modelling. Left inset: particles bouncing after second impact. Right inset: particles deposit in and around the sealing region.

In exactly the same way as in the assessment of the original geometry, different particle sizes are weighted with respect to their projected area on the poppet surface and the composition of the dust. Figure 5-16 depicts the contribution of individual particle sizes to the total dust distribution in the modified valve geometry. The dust deposition is predicted to be dominated by particles of diameter $> 0.015G_0$ in the sealing region, resulting in a reduction of the total deposition by approximately 40% in this region. The region of highest dust deposition occurs upstream of the sealing region.
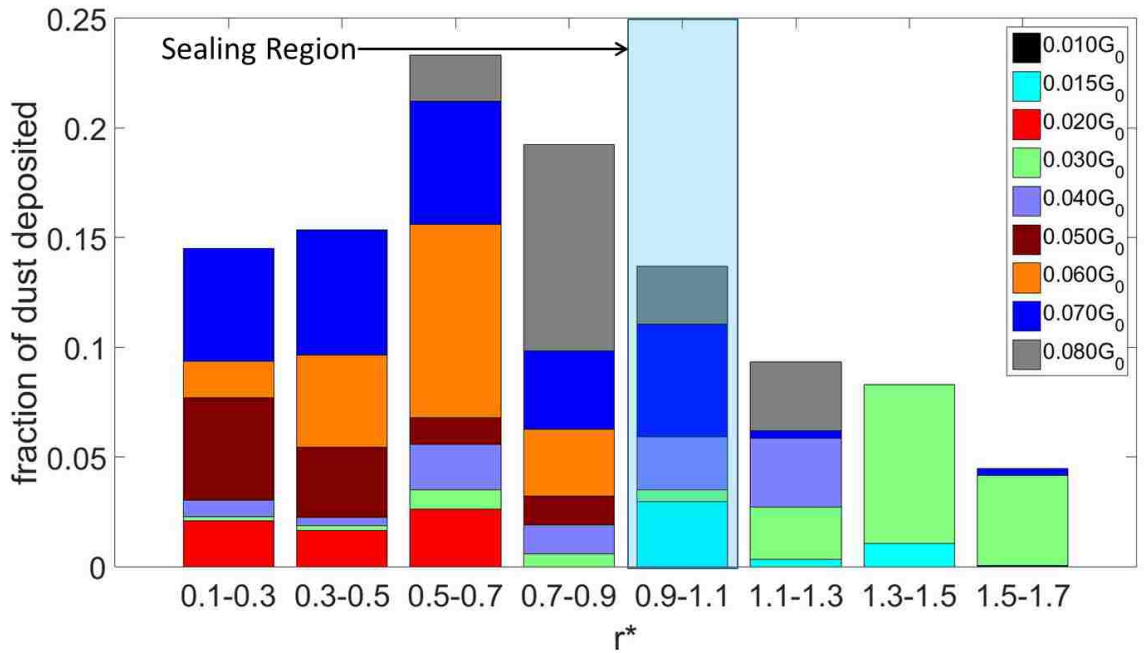
Figure 5-16: Prediction of contribution of individual particle sizes to total dust deposition on poppet surface in modified valve geometry. Approximately 75% of the dust in the sealing region is contributed by particles $> 0.015 G_0$.

5.4.2 Comparison with the Original Valve Geometry

Figure 5-17 is a comparison of the predicted dust deposition as a fraction of dust supplied for the original and modified valves using the advanced numerical modelling. Here, the fraction of dust supplied is used in contrast to previous figures which depicted the fraction of dust deposited. This is due to the fact that the amount of dust supplied is the same in both geometries while the amount of dust deposited is different. Thus, an objective comparison of the two designs must be based on the fraction of dust supplied. In the sealing region, a decrease in deposition of approximately 40% for the modified geometry is predicted.
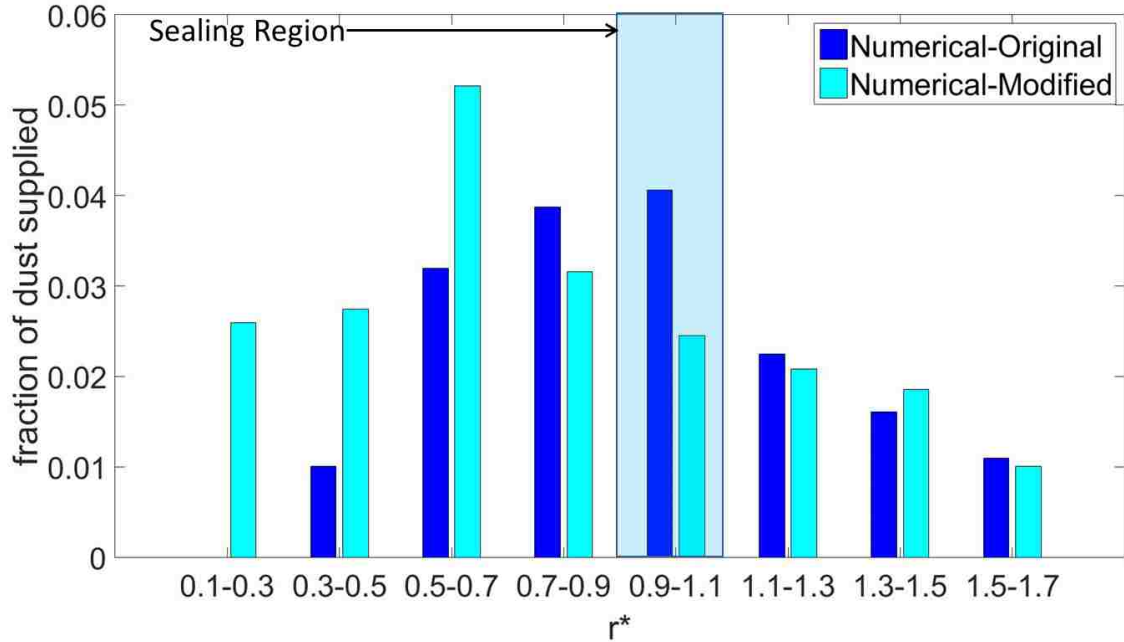
Figure 5-17: Advanced numerical modelling predicts reduction of dust deposition by $\approx 40\%$ in sealing region for the modified valve geometry.

Figures 5-18 and 5-19 are comparisons of the original and modified geometry results for the tangential and radial inlet configurations respectively. The results are again based on the fraction of dust supplied that is deposited in each $\Delta r^* = 0.2$ band. Since there was no way of determining what sizes of particles deposit in a given location in the experiments, the fraction of dust supplied is weighted based on the fraction of particles supplied that deposit in each $\Delta r^* = 0.2$ band in the computations. In both cases, the dust deposition has increased far upstream of the sealing region, but has been reduced significantly ($> 50\%$) in the sealing region. The reason behind this significant improvement is the change in trajectories of all particle sizes with the introduction of the washer. In the original geometry, particles of approximate diameter $0.010G_0$ are mostly responsible for dust deposition in the sealing region. In the modified design, these particles never impact the poppet surface and hence the dust deposition is reduced.
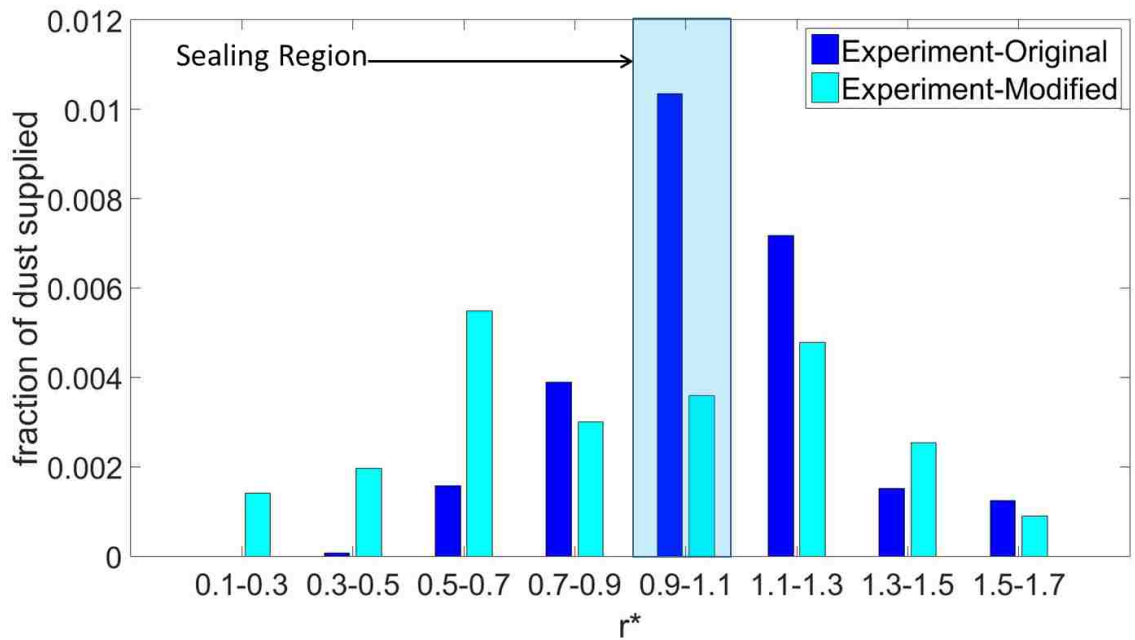
Figure 5-18: Experimentally measured dust deposition in the tangential inlet flow valve. Modified geometry reduces dust deposition by > 50% in the sealing region.
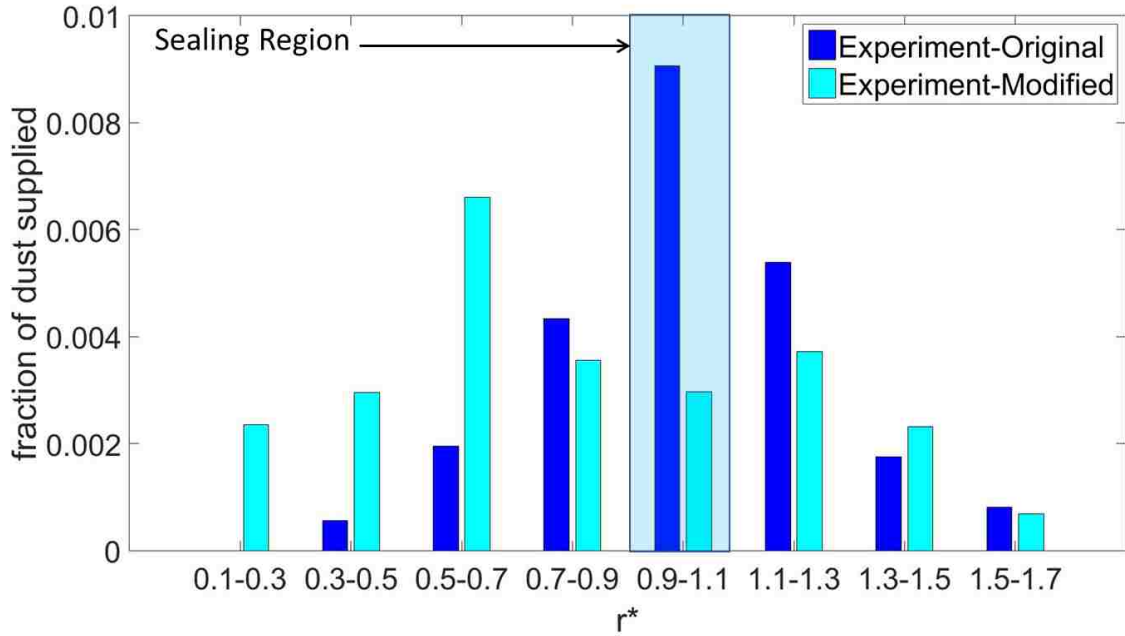
Figure 5-19: Experimentally measured dust deposition in the radial inlet flow valve. Modified geometry reduces dust deposition by > 50% in the sealing region.

For particles of larger diameters, such as $0.040G_0$ and $0.080G_0$, the initial impact angles are changed due to the presence of the washer such that most particles impact the poppet surface with high normal velocity, and rebound with a higher velocity than they do with the original valve geometry.

5.5   Comparison of Predicted and Measured Changes for the Modified Valve

The reduced dust deposition in both cases (tangential and radial inlets) is reflected in the leakage test results, discussed earlier in table 4.4. The modified geometry passes by margins of 60% and 72% under the leakage flow specification, for tangential and radial inlet flow cases, respectively. The modified geometry therefore, reduces leakage flow by up to 93% compared to the original geometry.

Figure 5-20 presents the percentage reduction in dust deposition for the modified valve as predicted by the computations and measured by the experiments. A positive value indicates that the modified geometry has less dust deposition in a radial band. In all bands, the experiments show greater changes than do the computations, including greater improvement in the sealing region. In some intervals, the deposition is higher in the modified than in the original geometry. Those regions lie outside of the sealing region and its adjacent bands. The advanced numerical method is seen to accurately predict the trends of decrease or increase of dust deposition in each band.
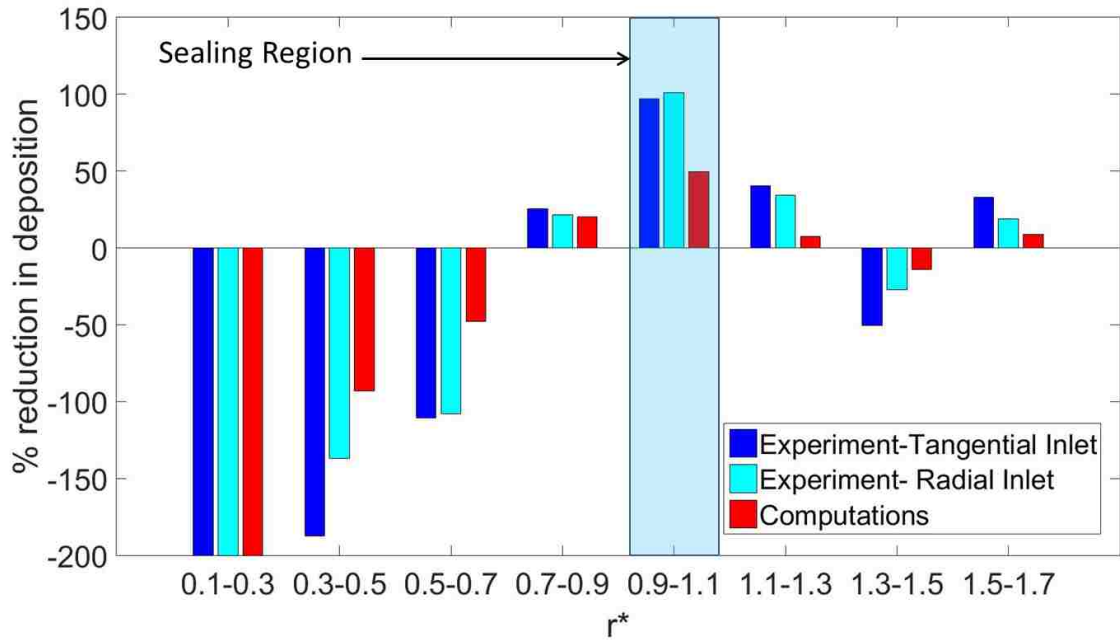
Figure 5-20: Percentage reduction in deposition associated with the modified valve as predicted by computations and measured by experiment.

Chapter 6

Summary, Conclusions, and Recommendations

This chapter briefly summarizes the work detailed in this thesis, extracts conclusions, and provides recommendations for future work and design best practices.

6.1   Summary

A detailed numerical and experimental assessment of a self-actuated pressure sealing valve is presented in this thesis. Using this combined approach, insight is gained into the mechanisms responsible for dust deposition in critical regions of this device. Based on the insight gained, modifications to the original geometry are made which alter the particle paths to decrease leakage flow without significantly increasing flow losses.

Numerical assessment is carried out with a simplified and an advanced numerical approach. It is established that although Discrete Phase Modelling (DPM) in Fluent is sufficient to model the discrete phase for the problems with low particulate concentration in the continuous phase, the built-in boundary conditions are not sufficient to assess the particle-wall interactions. A user defined function (UDF) is developed

and used to implement an advanced deposition model which enables the prediction of post-impact particle trajectories. An analysis with a simplified 90° bend geometry is conducted numerically and experimentally to determine the best combination of normal and tangential Coefficient of Restitution (C.O.R.). The best values are found to be 0.25 and 0.75 for the normal and tangential components, respectively. These values are used to further analyze dust deposition mechanisms in the self-sealing valve geometry. Dust deposition behaviour on a surface is altered by shifting and dispersing the particle impact locations, essentially increasing the particle's normal impact velocity and avoiding impacts for certain particle sizes. Less deposition in critical areas is seen as a result. The advanced numerical deposition model accurately captures the dust deposition trends seen in the experiments.

A dust quantification method and its application is also described. The approach is used to quantitatively and qualitatively compare a contaminated part to a clean part. This is achieved by finding the difference in brightness or greyscale level and then circumferentially averaging the differences (for circular poppets). This simple technique can be used to examine the change in patterns on any image, without the need for expensive equipment.

6.2   Conclusions

The main reason for dust deposition is identified as the impact of particles on the poppet surface with low normal velocity and low impact angles. Particles having lower momentum before the impact on a surface are less likely to bounce and hence are more likely to come to a complete stop. Particle deposition is also influenced by the location of initial impact. Impacts in and around the sealing region are avoided in the redesigned geometry, achieving a reduction of up to 93% in the leakage flow. The redesigned geometry has at least a 61% performance margin relative to the leakage

flow specifications. Comparison of experimental data and numerical predictions is made possible by the post-processing dust quantification model which requires only a standard digital camera and Matlab program. The advanced numerical model is able to predict particle deposition locations, on average, to within 15% of the predicted value with an 80% confidence level.

Differences in the inlet conditions have a small effect on the particle deposition behaviours, as seen in the differences between tangential and radial inlet flow experimental results. A single numerical model is sufficient to study the two different inlets. The radial inlet flow variant, in which the flow enters the valve with lower swirl than for the tangential inlet variant, shows a 30% larger reduction in leakage flow.

6.3 Recommendations

Based on the insight gained into dust deposition and the flow mechanisms at play in the self-sealing valve, recommendations are made regarding future product design guidelines. These are followed by recommendations for future work.

6.3.1 Design Guidelines

Firstly, as seen from the computational results and verified using the experiments, separation regions in the self-sealing geometry result in greater flow losses. These can be prevented by avoiding or shrinking separation regions as seen for the modified geometry in Fig. 4-13.

Secondly, to avoid impacts on a surface the particles should follow the fluid streamlines. In the case of a high density ratio of the particulate phase to the continuous phase, this is not possible. Particles deviate from the fluid streamlines when the flow experiences a sharp turn, as seen in Fig. 6-1. In the original geometry, the particles deviate from the streamlines near the sealing region and hence impact the surface.

In the modified geometry, due to the introduction of the washer, particles deviate from streamlines far upstream of the sealing region and are able to follow the streamlines again as they reach the sealing region (Fig. 6-2). Particle deviations, therefore, should occur outside the vicinity of critical regions so that particles can again the streamlines before reaching critical regions.

Thirdly, the main mechanism for particle deposition is determined to be particles impacting the surface at low impact angles, which should therefore be avoided. Particles contacting surfaces at low impact angles have lower normal velocity and are less likely to bounce. In Fig. 6-3, a particle hitting the wall at a low impact angle (14°) is not able to bounce while the particle impacting at a slightly higher impact angle (21°) is able to continue its trajectory.
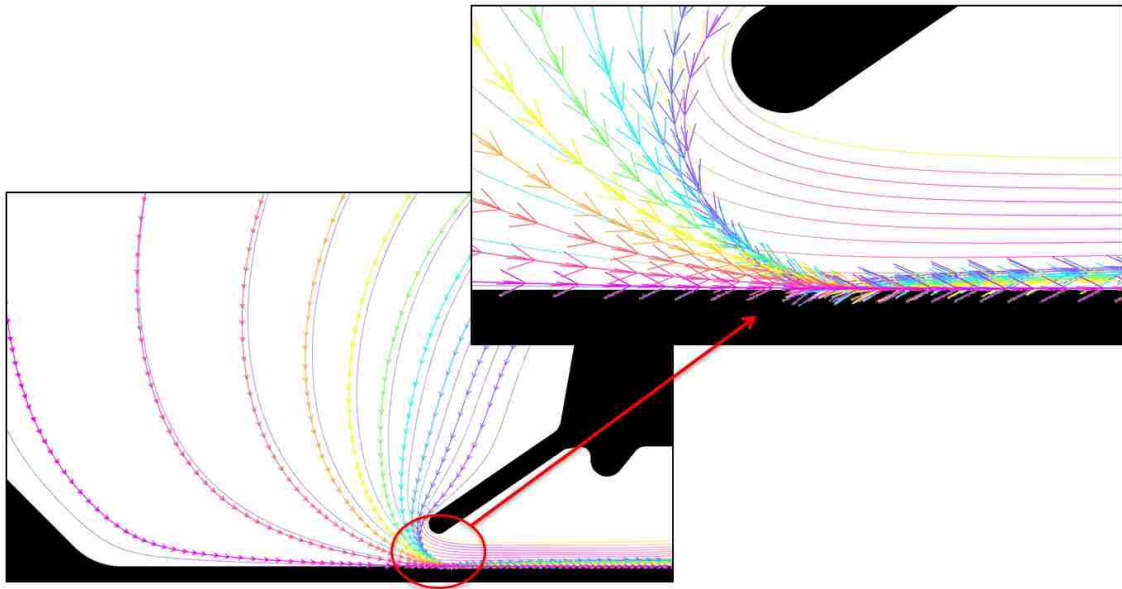
Figure 6-1: Particle tracks (lines with arrows) deviate from the streamlines (lines without arrows) close to the sealing region in the original geometry. Inset: particles impact on the poppet surface.
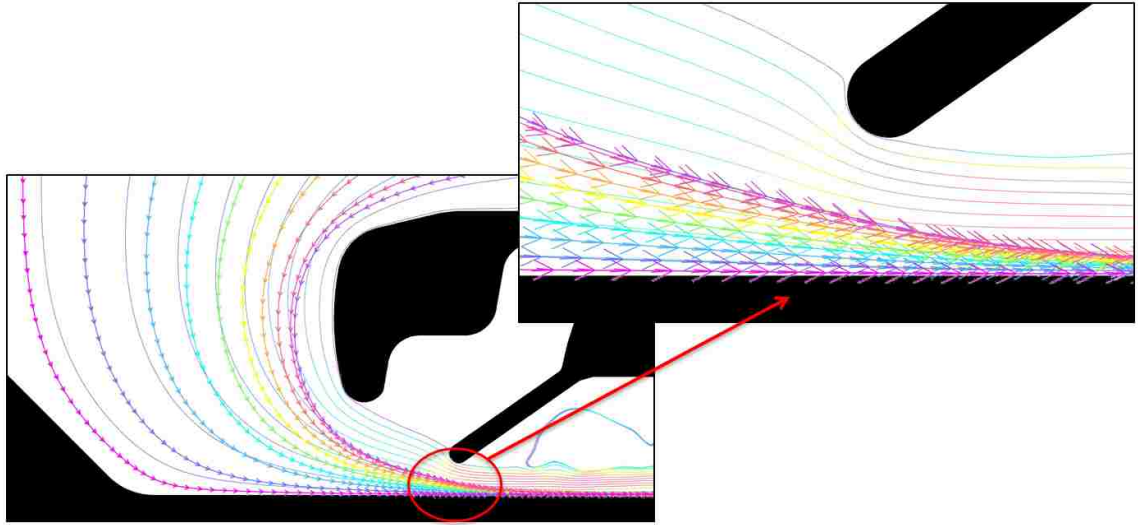
Figure 6-2: Particle tracks (lines with arrows) deviate from the streamlines (lines without arrows) far upstream of the sealing region in the modified geometry. Inset: particles follow the streamlines in the sealing region.

6.3.2 Future Work

This thesis involves the assessment of a self-sealing valve using an axisymmetric model. As discussed earlier, the ribs (Fig. 3-2) only cover about 40% of the circumferential area. Hence, computations should be carried out without the effects of these ribs in an axisymmetric model and the dust deposition predicted by weighing the effect of the ribs based on the area fraction they cover. Alternatively, a sector of the self-sealing valve can be simulated in 3D to account for the presence or absence of ribs. Also, experiments can be conducted to get accurate values of Coefficients of Restitution (C.O.R.) using different impact angles and different impact velocities.

As the self-sealing valve investigated in this thesis is a bi-directional valve, a computational study assessing the effect of flow in the reverse direction on already deposited particles could be conducted using the two way coupling for particle-fluid interactions.
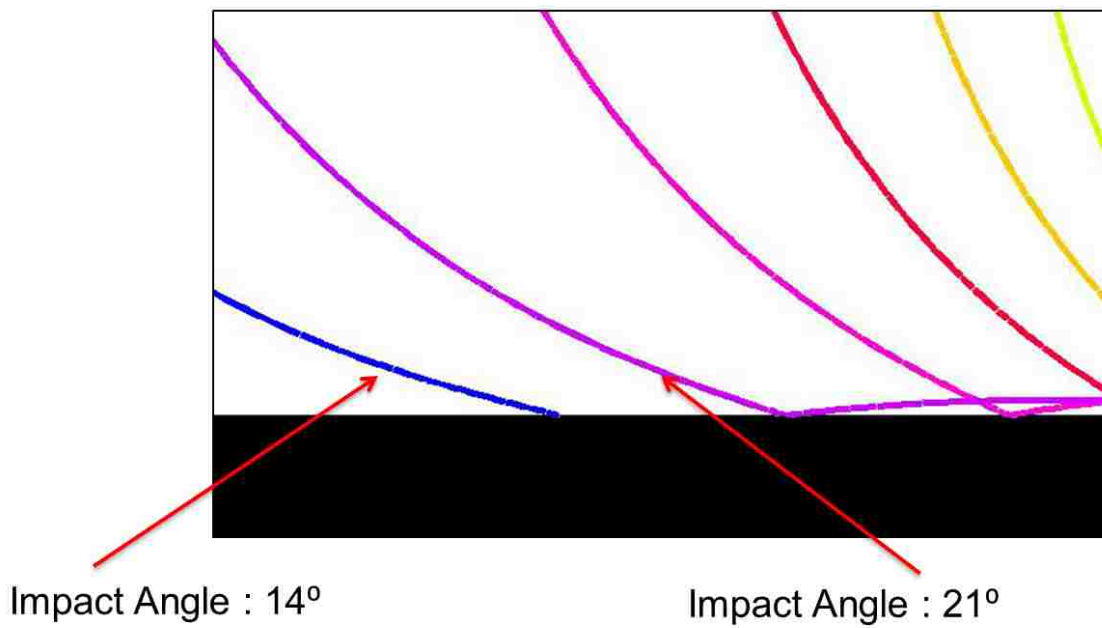
Figure 6-3: A particle hitting the poppet at low impact angle (14°) is not able to bounce while the particle impacting at a slightly higher impact angle (21°) is able to continue its trajectory.

Bibliography

[1] ANSYS, Inc., Canonsburg, PA. *ANSYS Fluent User's Guide, Version 15.0*, November 2013.

[2] The MathWorks, Inc., Natick, MA. *MATLAB Primer R2015a, Version 24*, March 2015.

[3] Zhang, P., Gros, Y., Roberts, R.M., and Benard, A. Modeling of turbulent Flow with particle deposition in curved pipes. In *7th International Conference on Multiphase Flow*, Tampa, FL USA, May 30 - June 4 2010.

[4] Chen, Q., and Ahmadi, G. Deposition of particles in a turbulent pipe flow. *Journal of Aerosol Science*, 28(5):789–796, 1997.

[5] Matida, E. A., Nishino, K., and Torii, K. Statistical simulation of particle deposition on the wall from turbulent dispersed pipe flow. *International Journal of Heat and Fluid Flow*, 21(4):389–402, 2000.

[6] Saffmam, P.G. The lift on a small sphere in a slow shear Flow. *Journal of Fluid Mechanics*, 31:624, 1968.

[7] Wilson, S. R., Liu, Y., Matida, E. A., and Johnson, M. R. Aerosol deposition measurements as a function of reynolds number for turbulent flow in a ninety-degree pipe bend. *Aerosol Science and Technology*, 45(3):364–375, 2011.

[8] Pilou, M., Tsangaris, S., Neofytou, P., Housiadas, C., and Drossinos, Y. Inertial particle deposition in a 90° laminar Flow Bend: An eulerian fluid particle approach. *Aerosol Science and Technology*, 45(11):1376–1387, 2011.

[9] Kleinstreuer, C., and Zhang, Z. Laminar-to-turbulent fluid-particle flow in human airway model. *International Journal of Multiphase Flow*, 29:271–289, 2003.

[10] Greenfield, C., and Quarini, G. A Lagrangian simulation of particle deposition in a turbulent boundary layer in the presence of thermophoresis. *Applied Mathematical Modeling*, 22:759–771, 1998.

[11] Abuzeid, S., Busnaina, A.A., and Ahmadi, G. Eulerian and Lagrangian simulation of particle deposition from a point source in a turbulent channel flow. *Particulate Science and Technology*, 8, 1990.

[12] Shankara, P.S. CFD simulation and analysis of particulate deposition on gas turbine vanes. Master's thesis, The Ohio State University, Columbus, Ohio, 2010.

[13] Karimi-Esfahani, M. An investigation of the cold gas dynamic supersonic spray process particle/flow field. Master's thesis, University of Windsor, Windsor, Ontario, 2005.

[14] El-Batsh, H., and Haselbacher. Numerical investigation of the effect of ash particle deposition on the flow field through turbine cascades. In *Proceedings of ASME Turbo Expo 2002*, Amsterdam, The Netherlands, June 3-6 2002.

[15] Meseguer,J.,Slobozhanin,L.A., and Perales,J.M. A review on the stability of liquid bridges. *Advances in Space Research*, 16(7):5–14, 1995.

[16] Berbner, S., and Loeffler, F. Influence of high temperatures on particle adhesion. *Powder Technology*, 78(3):273–280, 1994.

[17] Soltani, M., and Ahmadi, G. On particle adhesion and removal mechanisms in turbulent flow. *Journal of Adhesion Science and Technology*, 8(7), 1994.

[18] Johnson, K.L., Kendall, K., and Roberts, A.D. Surface energy and the contact of elastic solids. In *Proceedings of the Royal Society of London. Series A, Mathematical and Physical Sciences*, volume 324, pages 301–313. The Royal Society, September 1971.

[19] Dahneke, B. Further measurements of the bouncing of small latex spheres. *Journal of Colloid and Interface Science*, 51(1):58–65, 1974.

[20] Brach, R.M., and Dunn, P.F. A mathematical model of the impact and adhesion of microspheres. *Aerosol Science and Technology*, 16(1):51–64, 1992.

[21] Wang, H.C. Effects of inceptive motion on particle detachment from surfaces. *Aerosol Science and Technology*, 13(3):386–393, 1990.

[22] ANSYS, Inc., Canonsburg, PA. *ANSYS Fluent Meshing User's Guide, Version 15.0*, November 2013.

[23] Menter, F.R. Two-equation eddy-viscosity turbulence models for engineering applications. *AIAA Journal*, 32(8):1598–1605, August 1994.

[24] TSI Incorporated, Shoreview, MN. *General Purpose Thermal Mass Flowmmeter: Operation and Service Manual, Revision H*, August 2015.

[25] Emerson Process Management, Chanhassen, MN. *Rosemount 3051 Pressure Transmitter, Version SA*, September 2014.

[26] Meriam Process Technologies, Cleveland, OH. *Meriam LFE: Laminar Flow Element*, September 2011.

[27] ANSYS, Inc, Canonsburg, PA. *ANSYS Fluent UDF Manual, Version 15.0*, November 2013.

[28] Reagle, C.J. *Technique for measuring the coefficient of restitution for micropar-ticle sand imimpact at high temperature for turbomachinery applications.* PhD thesis, Virginia Polytechnic Institute and State University, August 2012.

[29] Holman, J. P. *Experimental methods for engineers.* McGraw-Hill, Seventh Edi-tion edition, 2001.

[30] Figliola, R. S., and Beasley, D. E. *Theory and design for mechanical measur-ments.* John Wiley & Sons, Inc., third edition, 2000.

Appendix A

Permissions

Dear Prof. Gill:

It has been confirmed that your paper was presented at the FEDSM2016 Conference, therefore, it is our pleasure to grant you permission to use all or any part of the ASME paper "A Combined Numerical and Experimental Assessment of Air and Dust Flow in a Low-Reynolds Number Valve Including Modifications to Prevent Valve Seal Contamination," by Ravinder Gill, Jeff Defoe, Gary Rankin, Paper number FEDSM2016-7669, cited in your letter for inclusion in a masters thesis dissertation tentatively entitled A COMBINED NUMERICAL AND EXPERIMENTAL ASSESSMENT OF AIR AND DUST FLOW IN A LOW-REYNOLDS NUMBER VALVE INCLUDING MODIFICATIONS TO PREVENT VALVE SEAL CONTAMINATIONto be published by University of Windsor.

Permission is granted for the specific use as stated herein and does not permit further use of the materials without proper authorization. Proper attribution must be made to the author(s) of the materials. **Please note:** if any or all of the figures and/or Tables are of another source, permission should be granted from that outside source or include the reference of the original source. ASME does not grant permission for outside source material that may be referenced in the ASME works.

As is customary, we request that you ensure full acknowledgment of this material, the author(s), source and ASME as original publisher. Acknowledgment must be retained on all pages printed and distributed.

Many thanks for your interest in ASME publications.

Sincerely,

Beth Darchi
Publishing Administrator
ASME
2 Park Avenue, 6th Floor
New York, NY 10016-5990
Tel 1.212.591.7700
darchib@asme.org

Figure A-1: Permission from ASME regarding work published in the Proceedings of FEDSM 2016.

Appendix B

Derivation of Fluid Velocity at the Centre of the Particle

In the viscous sub-layer, the dimensionless streamwise velocity, u^+ is equal to the dimensionless wall distance, y^+:

$$u^+ = y^+ \tag{B.1}$$

u^+ can be expressed in terms of fluid velocity, V, and wall friction velocity, u^*:

$$u^+ = \frac{u}{u^*} = \frac{V}{u^*} \tag{B.2}$$

y^+ can be expressed in terms of u^* and y (the distance of the first grid point from the wall, which is equal to the radius of the particle):

$$y^+ = \frac{u^* y \rho}{\mu} = \frac{u^* y}{\mu} \frac{d_p}{2} \tag{B.3}$$

Hence, the fluid velocity V can be represented as:

$$V = \frac{\rho}{\mu} \frac{d_p}{2} u^{*2} \tag{B.4}$$

Appendix C

Composition of Arizona Fine Dust

Table C.1 shows the composition of Arizona fine dust particles sizes by volume percentage. The table presented here is modified to illustrate composition according to the normalized dust size. The actual composition table can be accessed from Powder Technologies Inc. website, available at:

http://www.powdertechnologyinc.com/product/iso-12103-1-a2-fine-test-dust/

Table C.1: Arizona Fine Volume % composition available from Powder Technologies Inc.

Size	% Less than
$0.0019G_0$	$4.5 - 5.5$
$0.0028G_0$	$8.0 - 9.5$
$0.0055G_0$	$21.3 - 23.3$
$0.011G_0$	$39.5 - 42.5$
$0.022G_0$	$57.0 - 59.5$
$0.044G_0$	$73.5 - 76.0$
$0.088G_0$	$89.5 - 91.5$
$0.176G_0$	$97.9 - 98.9$
$0.249G_0$	$99.0 - 100.0$
$0.352G_0$	100.0

Appendix D

Matlab Code Used in Post-Processing

```matlab
%Created by Ravinder Gill
tic
clear
clc
close all
profile −timer real


%defining the xy coordinates of image
x=[−250:1:250];
y=[−250:1:250];


%changing xy xoordinates to r and theta
[X,Y]= meshgrid(x,y);
R=sqrt(X.^2+Y.^2);
theta=atan2(Y,X);
```

```matlab
r2=linspace(80,245,166);
theta2=linspace(0,2*pi-2*pi/1001,1001);
[R2,THETA2]=meshgrid(r2,theta2);


hold on
figure(1)
%reading the clean poppet image,converting it from rgb to %
    grayscale,cropping, resizing and converting it to polar matrix.
CP=imread('%Path_to_the_locatin_of_image_stored_on_local_machine%'
    );
CPgray=rgb2gray(CP);
CPdouble=im2double(CPgray);


    CPdouble=imresize(CPdouble,0.5);
imshow(CPdouble);
CPimagesize=size(CPdouble);
CPimagesizeX=CPimagesize(:,1);
CPimagesizeY=CPimagesize(:,2);


[CPa,CPb] = newginput(3);
CPpt1=[CPa(1,:),CPb(1,:)];
CPpt2=[CPa(2,:),CPb(2,:)];
CPpt3=[CPa(3,:),CPb(3,:)];
[cCP rCP] = circlepoints(CPpt1, CPpt2, CPpt3);
xCP=cCP(:,1);
yCP=cCP(:,2);
rCP=rCP(1,:);  circCP= draw(xCP,yCP,rCP);
```

```matlab
choiceCP=questdlg ( 'Are_you_happy_with_the_selection_of_points?' , '
    Point_Seletion ' , 'Yes ' , 'No ' , 'No ' ) ;
while ~isequal ( choiceCP , 'Yes ' )
        switch choiceCP
                case 'Yes '
                        disp ( [ choiceCP ' points_are_confirmed . ' ] )
                case 'No '
                        disp ( [ choiceCP ' reselect_the_points . ' ] )
                        [ CPa ,CPb]=newginput ( 3 ) ;
                        CPpt1=[CPa ( 1 , : ) ,CPb ( 1 , : ) ] ;
                        CPpt2=[CPa ( 2 , : ) ,CPb ( 2 , : ) ] ;
                        CPpt3=[CPa ( 3 , : ) ,CPb ( 3 , : ) ] ;
                        [ cCP rCP ] = circlepoints (CPpt1 , CPpt2 ,
                            CPpt3 )
                        xCP=cCP ( : , 1 ) ;
                        yCP=cCP ( : , 2 ) ;
                        rCP=rCP ( 1 , : ) ;
                        circCP= draw (xCP , yCP , rCP ) ;
                        choiceCP=questdlg ( 'Are_you_happy_with_the_
                            selection_of_points?' , 'Point_Seletion ' ,
                            'Yes ' , 'No ' , 'No ' ) ;
end
end
CPcropped=imcrop (CPdouble , [ xCP-rCP yCP-rCP , 2*rCP 2*rCP ] ) ;
imshow (CPcropped )
CPfinal=imresize (CPcropped , [ 501 501 ] ) ;
CPsurface = scatteredInterpolant ( [R ( : ) ;R ( : ) ] , [ theta ( : ) ; 2*pi+theta
    ( : ) ] , [ CPfinal ( : ) ; CPfinal ( : ) ] , 'linear ' , 'none ' ) ;
CP_polar=CPsurface (R2 ,THETA2 ) ;
```

%%Same procedure is followed for the images of dirty poppets which give AC_polar and AW_polar matrix%%

%POLAR DIFFEREDENCE MATRIX

DAC_polar=CP_polar−AC_polar ;

DAW_polar=CP_polar−AW_polar ;

%Mean over circumference

DAC_polar_avg=**mean**(DAC_polar,1) ;

DAW_polar_avg=**mean**(DAW_polar,1) ;

hold on

Raxis1=**linspace**(4.12,12.8,166) ;

Raxis1=**linspace**(4.12,12.8,166) ;

Raxis=(Raxis1−4.12)/(9.0−4.12) ;

ri1=(4.88∗Raxis(:,4:23))+4.12;

ri2=(4.88∗Raxis(:,24:43))+4.12;

ri3=(4.88∗Raxis(:,44:63))+4.12;

ri4=(4.88∗Raxis(:,64:83))+4.12;

ri5=(4.88∗Raxis(:,84:103))+4.12;

ri6=(4.88∗Raxis(:,104:123))+4.12;

ri7=(4.88∗Raxis(:,124:143))+4.12;

ri8=(4.88∗Raxis(:,144:163))+4.12;

r1=(4.88∗Raxis+4.12) ;

deltar1=r1(:,2)−r1(:,1) ;

%experimentaldust deposition of first dirty poppet

xi11=DAC_polar_avg(:,4:23) ;

```matlab
xi12=DAC_polar_avg(:,24:43);
xi13=DAC_polar_avg(:,44:63);
xi14=DAC_polar_avg(:,64:83);
xi15=DAC_polar_avg(:,84:103);
xi16=DAC_polar_avg(:,104:123);
xi17=DAC_polar_avg(:,124:143);
xi18=DAC_polar_avg(:,144:163);
den1=(2*pi).*(sum(DAC_polar_avg.*r1.*deltar1));
dep11=((2*pi).*( sum(xi11.*ri1.*deltar1)))/den1;
dep12=((2*pi).*( sum(xi12.*ri2.*deltar1)))/den1;
dep13=((2*pi).*( sum(xi13.*ri3.*deltar1)))/den1;
dep14=((2*pi).*( sum(xi14.*ri4.*deltar1)))/den1;
dep15=((2*pi).*( sum(xi15.*ri5.*deltar1)))/den1;
dep16=((2*pi).*( sum(xi16.*ri6.*deltar1)))/den1;
dep17=((2*pi).*( sum(xi17.*ri7.*deltar1)))/den1;
dep18=((2*pi).*( sum(xi18.*ri8.*deltar1)))/den1;


dustdep1=[dep11;dep12;dep13;1.2*dep14;dep15;1.2*dep16;dep17;dep18
    ];   %dust deposition fractions for first dirty poppet



%Using the same procedure, experimental dust deposited on second
    dirty poppet can be found
dustdep2=[dep21;dep22;dep23;dep24;dep25;dep26;dep27;dep28];

%%computational dust deposition prediction
%7.5microns
particledep7p5=xlsread('7.5micronstickinglocations.xlsx')*1000
A7p5=(particledep7p5-4.12)./(9.0-4.12)
```

B7p5=**sort**(A7p5)

edges=[0.1 0.3 0.5 0.7 0.9 1.1 1.3 1.5 1.7]

N7p5=histcounts(B7p5,edges)

numdep7p5=N7p5;

S7p5=**sum**(numdep7p5);

%10microns

particledep10=xlsread('10micronstickinglocations.xlsx')*1000

A10=(particledep10−4.12)./(9.0−4.12)

B10=**sort**(A10)

edges=[0.1 0.3 0.5 0.7 0.9 1.1 1.3 1.5 1.7]

N10=histcounts(B10,edges)

numdep10=N10;

S10=**sum**(numdep10);

%%Simularly, computational dust depesition for other dust sizes is determined

AreaImpacted= (.429*155***pi***R5^2)+(.1*155***pi***R7p5^2)+ (.1*155***pi*** R10^2)+(.09*155***pi***R15^2)+ (.09*155***pi***R20^2)+(.045*155***pi***R25 ^2)+(.045*155***pi***R30^2)+ (.045*155***pi***R35^2)+(.045*155***pi***R40 ^2);

depbin1= ((.429*numdep5(:,1)***pi***R5^2)./AreaImpacted)+((.1* numdep7p5(:,1)***pi***R7p5^2)./AreaImpacted)+((.1*numdep10(:,1)***pi*** R10^2)./AreaImpacted)+((0.09*numdep15(:,1)***pi***R15^2)./ AreaImpacted)+((0.09*numdep20(:,1)***pi***R20^2)./AreaImpacted) +((0.045*numdep25(:,1)***pi***R25^2)./AreaImpacted)+((0.045* numdep30(:,1)***pi***R30^2)./AreaImpacted)+((0.045*numdep35(:,1)***pi*** *R35^2)./AreaImpacted)+((0.045*numdep40(:,1)***pi***R40^2)./

AreaImpacted)

depbin2= ((.429*numdep5(:,2)*pi*R5^2)./AreaImpacted)+((.1*
numdep7p5(:,2)*pi*R7p5^2)./AreaImpacted)+((.1*numdep10(:,2)*pi*
R10^2)./AreaImpacted)+((0.09*numdep15(:,2)*pi*R15^2)./
AreaImpacted)+((0.09*numdep20(:,2)*pi*R20^2)./AreaImpacted)
+((0.045*numdep25(:,2)*pi*R25^2)./AreaImpacted)+((0.045*
numdep30(:,2)*pi*R30^2)./AreaImpacted)+((0.045*numdep35(:,2)*pi
*R35^2)./AreaImpacted)+((0.045*numdep40(:,2)*pi*R40^2)./
AreaImpacted)

depbin3= ((.429*numdep5(:,3)*pi*R5^2)./AreaImpacted)+((.1*
numdep7p5(:,3)*pi*R7p5^2)./AreaImpacted)+((.1*numdep10(:,3)*pi*
R10^2)./AreaImpacted)+((0.09*numdep15(:,3)*pi*R15^2)./
AreaImpacted)+((0.09*numdep20(:,3)*pi*R20^2)./AreaImpacted)
+((0.045*numdep25(:,3)*pi*R25^2)./AreaImpacted)+((0.045*
numdep30(:,3)*pi*R30^2)./AreaImpacted)+((0.045*numdep35(:,3)*pi
*R35^2)./AreaImpacted)+((0.045*numdep40(:,3)*pi*R40^2)./
AreaImpacted)

depbin4= ((.429*numdep5(:,4)*pi*R5^2)./AreaImpacted)+((.1*
numdep7p5(:,4)*pi*R7p5^2)./AreaImpacted)+((.1*numdep10(:,4)*pi*
R10^2)./AreaImpacted)+((0.09*numdep15(:,4)*pi*R15^2)./
AreaImpacted)+((0.09*numdep20(:,4)*pi*R20^2)./AreaImpacted)
+((0.045*numdep25(:,4)*pi*R25^2)./AreaImpacted)+((0.045*
numdep30(:,4)*pi*R30^2)./AreaImpacted)+((0.045*numdep35(:,4)*pi
*R35^2)./AreaImpacted)+((0.045*numdep40(:,4)*pi*R40^2)./
AreaImpacted)

depbin5= ((.429*numdep5(:,5)*pi*R5^2)./AreaImpacted)+((.1*
numdep7p5(:,5)*pi*R7p5^2)./AreaImpacted)+((.1*numdep10(:,5)*pi*
R10^2)./AreaImpacted)+((0.09*numdep15(:,5)*pi*R15^2)./
AreaImpacted)+((0.09*numdep20(:,5)*pi*R20^2)./AreaImpacted)

$+((0.045*\text{numdep25}(:,5)*\textbf{pi}*\text{R25}\,\hat{}\,2)./\text{AreaImpacted})+((0.045*\\\text{numdep30}(:,5)*\textbf{pi}*\text{R30}\,\hat{}\,2)./\text{AreaImpacted})+((0.045*\text{numdep35}(:,5)*\textbf{pi}\\*\text{R35}\,\hat{}\,2)./\text{AreaImpacted})+((0.045*\text{numdep40}(:,5)*\textbf{pi}*\text{R40}\,\hat{}\,2)./\\\text{AreaImpacted})$

$\text{depbin6}=((.429*\text{numdep5}(:,6)*\textbf{pi}*\text{R5}\,\hat{}\,2)./\text{AreaImpacted})+((.1*\\\text{numdep7p5}(:,6)*\textbf{pi}*\text{R7p5}\,\hat{}\,2)./\text{AreaImpacted})+((.1*\text{numdep10}(:,6)*\textbf{pi}*\\\text{R10}\,\hat{}\,2)./\text{AreaImpacted})+((0.09*\text{numdep15}(:,6)*\textbf{pi}*\text{R15}\,\hat{}\,2)./\\\text{AreaImpacted})+((0.09*\text{numdep20}(:,6)*\textbf{pi}*\text{R20}\,\hat{}\,2)./\text{AreaImpacted})\\+((0.045*\text{numdep25}(:,6)*\textbf{pi}*\text{R25}\,\hat{}\,2)./\text{AreaImpacted})+((0.045*\\\text{numdep30}(:,6)*\textbf{pi}*\text{R30}\,\hat{}\,2)./\text{AreaImpacted})+((0.045*\text{numdep35}(:,6)*\textbf{pi}\\*\text{R35}\,\hat{}\,2)./\text{AreaImpacted})+((0.045*\text{numdep40}(:,6)*\textbf{pi}*\text{R40}\,\hat{}\,2)./\\\text{AreaImpacted})$

$\text{depbin7}=((.429*\text{numdep5}(:,7)*\textbf{pi}*\text{R5}\,\hat{}\,2)./\text{AreaImpacted})+((.1*\\\text{numdep7p5}(:,7)*\textbf{pi}*\text{R7p5}\,\hat{}\,2)./\text{AreaImpacted})+((.1*\text{numdep10}(:,7)*\textbf{pi}*\\\text{R10}\,\hat{}\,2)./\text{AreaImpacted})+((0.09*\text{numdep15}(:,7)*\textbf{pi}*\text{R15}\,\hat{}\,2)./\\\text{AreaImpacted})+((0.09*\text{numdep20}(:,7)*\textbf{pi}*\text{R20}\,\hat{}\,2)./\text{AreaImpacted})\\+((0.045*\text{numdep25}(:,7)*\textbf{pi}*\text{R25}\,\hat{}\,2)./\text{AreaImpacted})+((0.045*\\\text{numdep30}(:,7)*\textbf{pi}*\text{R30}\,\hat{}\,2)./\text{AreaImpacted})+((0.045*\text{numdep35}(:,7)*\textbf{pi}\\*\text{R35}\,\hat{}\,2)./\text{AreaImpacted})+((0.045*\text{numdep40}(:,7)*\textbf{pi}*\text{R40}\,\hat{}\,2)./\\\text{AreaImpacted})$

$\text{depbin8}=((.429*\text{numdep5}(:,8)*\textbf{pi}*\text{R5}\,\hat{}\,2)./\text{AreaImpacted})+((.1*\\\text{numdep7p5}(:,8)*\textbf{pi}*\text{R7p5}\,\hat{}\,2)./\text{AreaImpacted})+((.1*\text{numdep10}(:,8)*\textbf{pi}*\\\text{R10}\,\hat{}\,2)./\text{AreaImpacted})+((0.09*\text{numdep15}(:,8)*\textbf{pi}*\text{R15}\,\hat{}\,2)./\\\text{AreaImpacted})+((0.09*\text{numdep20}(:,8)*\textbf{pi}*\text{R20}\,\hat{}\,2)./\text{AreaImpacted})\\+((0.045*\text{numdep25}(:,8)*\textbf{pi}*\text{R25}\,\hat{}\,2)./\text{AreaImpacted})+((0.045*\\\text{numdep30}(:,8)*\textbf{pi}*\text{R30}\,\hat{}\,2)./\text{AreaImpacted})+((0.045*\text{numdep35}(:,8)*\textbf{pi}\\*\text{R35}\,\hat{}\,2)./\text{AreaImpacted})+((0.045*\text{numdep40}(:,8)*\textbf{pi}*\text{R40}\,\hat{}\,2)./\\\text{AreaImpacted})$

```
depfinal=[depbin1 depbin2 depbin3 depbin4 depbin5 depbin6 depbin7
    depbin8]        %numerical dust deposition prediction
chart=[dustdep1 dustdep2 depfinal]

H=bar(chart,'grouped')
set(H,{'FaceColor'},{'b';'c';});
set(gca,'fontsize', 34);
xlabel('r*');
ylabel('fraction_of_dust_depsited');
A=legend('Experiment-Tangential','Experiment-Radial','Computations
    ');
Labels = {'0.1-0.3', '0.3-0.5', '0.5-0.7', '0.7-0.9','0.9-1.1','
    1.1-1.3','1.3-1.5','1.5-1.7'};
set(gca, 'XTick', 1:8, 'XTickLabel', Labels);
set(A,'fontsize',34)

%Function file- circlepoints.m
%% Calculates the centre and radius of the circle from selected
    points %%

function [centre radius] = circlepoints(pt1, pt2, pt3)

pt1 = double(pt1);
pt2 = double(pt2);
pt3 = double(pt3);
delta_a = pt2 - pt1;
delta_b = pt3 - pt2;
grad_a = delta_a(2) / delta_a(1);
grad_b = delta_b(2) / delta_b(1);
```

```
%centre  is  where  the  lines  perpendicular  to  the  center  of  a  and  b
    intersect
centre(1) = (  grad_a*grad_b*(pt1(2)−pt3(2)) + grad_b*(pt1(1)+pt2
    (1)) − grad_a*(pt2(1)+pt3(1)) ) / (2*(grad_b−grad_a));
centre(2) = ((pt1(1)+pt2(1))/2 − centre(1)) / grad_a + (pt1(2)+pt2
    (2))/2;
radius = norm(centre − pt1);


%Function  file −  draw.m
%draws  a  circle  based  on  centre  and  radius  calculated  by
    circlepoints.m
function  c = draw(x,y,r)
hold on
th = 0:pi/50:2*pi;
xunit = r * cos(th) + x;
yunit = r * sin(th) + y;
c = plot(xunit, yunit);
hold  off


%The  function  newginput.m  is  the  modified  version  of  matlab  built−
    in  ginput.m  with  changed  cursor  type.
```

Appendix E

Uncertainty Analysis

In this appendix, the methodology and equations used to determine the uncertainty of quantities measured in the experiments are presented. Note that the nomenclature used in this appendix is separate from that used in the remainder of the thesis.

E.1 Design Stage Uncertainty

The design stage uncertainty, U_d, in a measurement is given by the device and can be calculated by equation [29]:

$$U_d = \sqrt{U_0^2 + U_C^2} \qquad (E.1)$$

where U_0 is the zero order uncertainty and is given by

$$U_0 = \pm \frac{1}{2} \text{ (instument scale resolution)}, \qquad (E.2)$$

and U_C corresponds to the instrument error given by

$$U_C = \sqrt{\sum_{i=i}^{M} e_i^2} \qquad (E.3)$$

where M is the number of errors e_i listed by the manufacturer.

E.2 Resultant Uncertainty due to More Than one Variable

To find the uncertainty in a function R composed of n independent variables $x_1 \ldots x_n$, the most probable value of the resultant uncertainty, U_R, is given by Kline and Mc-Clintock equation [30]:

$$U_R = \sqrt{\left(\frac{\partial R}{\partial x_1}U_1\right)^2 + \left(\frac{\partial R}{\partial x_2}U_2\right)^2 + \ldots\ldots\ldots\ldots\ldots + \left(\frac{\partial R}{\partial x_n}U_n\right)^2} \qquad \text{(E.4)}$$

where U_i is the uncertainty of n independent variables.

E.3 Uncertainty in the Mass Flow Rate Reading

The resolution of the mass flow rate meter is 0.01 Std L/min, which gives a zero order uncertainty of ± 0.005 Std L/min. The accuracy of the mass flow rate meter is given to be 2% of the reading. For $\dot{m}_0$ value of 25.7 Std L/min, the uncertainty due to instrument error is computed to be 0.514 Std L/min. Calculating the design stage uncertainty using equation E.1 gives a value equal to 2% of the $\dot{m}_0$ value.

E.4 Uncertainty in the Leakage Flow Rate Reading

The leakage flow rate is computed using the calibration equation from Meriam (the LFE Supplier). The equation is given as follows:

$$\dot{m} = \rho * \left((B \times \Delta P) + (C \times (\Delta P)^2)\right) \qquad \text{(E.5)}$$

where B and C are calibration constants provided by the supplier which have values of 1.53×10^{-4} CFM/in. H_2O and 1.9×10^{-7} CFM/(in. H_2O).^{2}, respectively.

The uncertainty in the pressure measurement comes from the pressure transducer (Rosemount 3051) and is equal to 0.04% of the span (for a span value of 4 in. H_2O, the resulting uncertainty is 0.0016 in. H_2O). The accuracy of the LFE is provided to be 0.72%. Using equations E.4 and E.1, the uncertainty in the leakage flow measurement is computed to be 2.7% of the reading.

E.5 Precision Error

Precision error is the measure of the scatter of data from repeated measurements made under nominally fixed operating conditions. A statistical estimate of the precision uncertainty is available using a 95% confidence interval from the Student's t test and is given by following formula [30]:

$$U_p = t_{v,P} S_x \tag{E.6}$$

where $t_{v.P}$ is the Student's t value at $v = n - 1$ (degrees of freedom) and $P = 95\%$ confidence interval. S_x is the standard deviation of the sample data.

The precision error is assessed for the the post-processing image comparison approach and is found to be 0.54% and 0.38% for the self sealing valve and simplified 90°bend geometry analysis, respectively. The Matlab code for the computation of this precision uncertainty is given below, where a sample of five images (of the same part) is used. Figure E-1 shows the standard deviation of the five measurements with respect to the mean values in different bands.
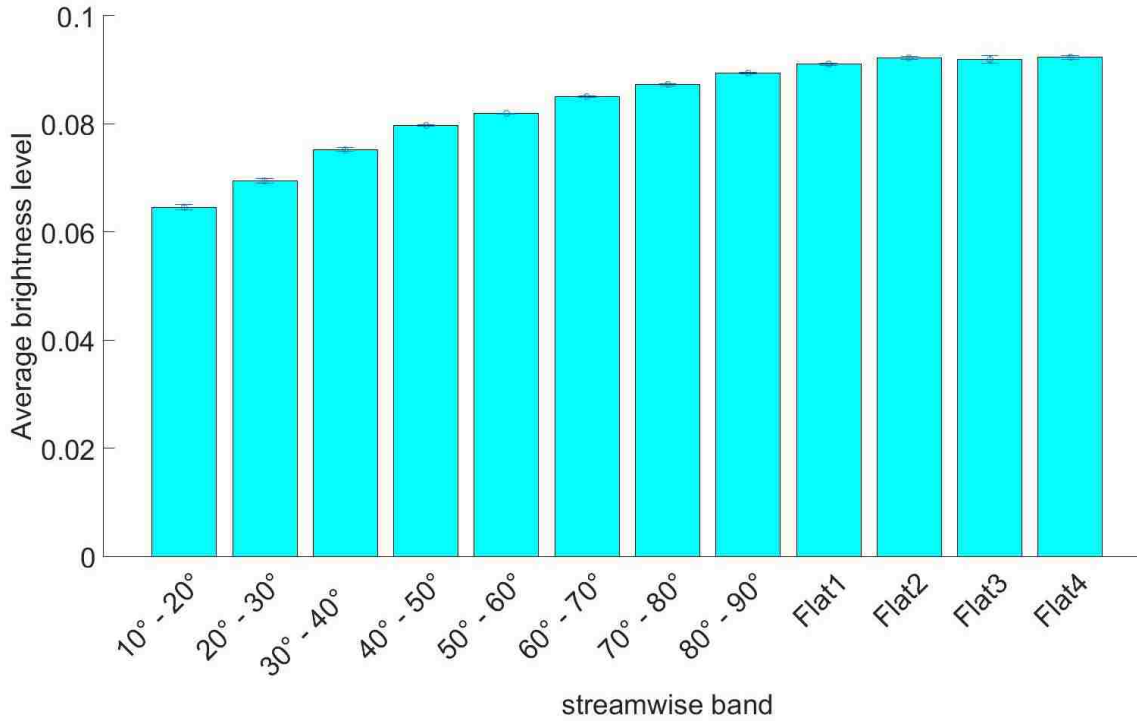
Figure E-1: Average brightness level from five attempts of taking image of a single clean part. Error bars show ±1 standard deviation.

E.6   Matlab Code for Uncertainty Calculation

%Using the matlab code in appendix B, get 5 different brightness matrices **for** 5 images of clean parts and combine them to a single matrix
chart=[sumDPmatrixnew sumDP2matrixnew sumDP3matrixnew sumDP4matrixnew sumDP5matrixnew];

%calculate the average and standard deviation in 5 attempts
average=**mean**(transpose(chart));
standarddeviation=**std**(transpose(chart));

```
%Plot the standard deviation levels on the average brightness level
figure(2)
hold on
H=bar(1:12,average(:,2:13))
set(H,{'FaceColor'},{'c'});
errorbar(1:12,average(:,2:13),standarddeviation(:,2:13),'o')
set(gca,'fontsize', 28);
B=ylabel('Average_brightness_level');
set(B,'fontsize', 28);
C=xlabel('streamwise_distance');
set(C,'fontsize', 28);
sprintf('20%c_-_30%c',char(176),char(176)),
sprintf('30%c_-_40%c___',char(176),char(176)),
sprintf('40%c_-_50%c',char(176),char(176)),
sprintf('50%c_-_60%c',char(176),char(176)),
sprintf('60%c_-_70%c',char(176),char(176)),
sprintf('70%c_-_80%c',char(176),char(176)),
sprintf('80%c_-_90%c',char(176),char(176)),
sprintf('Flat1'),sprintf('Flat2'),sprintf('Flat3'),sprintf('Flat4')};
set(gca, 'XTick', 1:12, 'XTickLabel', Labels);
ax=gca;
ax.XTickLabelRotation=45

%finding resultant standard deviation using pooled statistics
resultantstd=sqrt((1/12).*sum(standarddeviation.^2))
%calculating uncertainty using 95% confidence interval
t=2.015;    %for a sample size of 5
P=resultantstd./sqrt(5)
uncertainty=t.*P
```

Appendix F

UDF Code for Advanced Deposition Model

```
/* Created by Ravinder Gill*/
/* boundary condition for particle−wall impact */
#include "udf.h"
#include "dpm.h"
#include "mem.h"
#include "sg.h"
#define NUM_UDM 6 /* number of user defined memory locations */
real ParticleTotalMass;
real P_Mass[6];
real P_Impact_Mass[6];
real P_Stick_Mass[6];
Domain *domain;

/* Boundary Condition macro for deposition model*/
DEFINE_DPM_BC(bc_reflect, p, t, f, f_normal, dim)
{
```

```
#if RP_2D
/*#if RP_3D only for 3D cases*/
real alpha,vcr=0,calc,E,val,kc,ucws,ucrr,ucrs,ustar,yplus,ds;
/* angle of particle path with face normal */
real ks,kp; real vn=0 ; real vpabs=0, MassImpact,MassI,
MassS,xpos,ypos,zpos,
particle,Fd,Fpo,distance,a,dragmoment,adhesionmoment,adhesionfriction;
real nor_coeff = 0.25;
real tan_coeff = 0.75;
real Wa = 0.039; /* work of adhesion*/
real nu_s = 0.30; /* Poisson's ratio for surface */
real nu_p = 0.33; /* Poisson's ratio for particle */
real E_s = 3.2e11; /* Young's modulus for surface */
real E_p = 1.2e9; /* Young's modulus for particle */
real rho_p = 983; /* density of particle */
real VISC = 1.7894e-05 ; /*Viscosity of air*/
real k=0.5; /*static coefficient of friction*/
real tem_Mass=0;
real tem_Particle_Dia=0;
real A[ND_ND],es[ND_ND], dr0[ND_ND];

FILE *fp1;
FILE *fp2;
FILE *fp3;
FILE *fp4;

Thread *tcell = P_CELL_THREAD(p);
/*pointer to the thread of the cell that the particle is currently in*/
cell_t c = P_CELL(p);
```

```
/* cell index of the cell that the particle is currently in */


Domain* d;
real normal[3];
int i, idim = dim;
real NV_VEC(x);


if (rp_axi_swirl)
{
real R = sqrt(p->state.pos[1]*p->state.pos[1] +
p->state.pos[2]*p->state.pos[2]);
if (R > 1.e-20)
{
idim = 3;
normal[0] = f_normal[0];
normal[1] = (f_normal[1]*p->state.pos[1])/R;
normal[2] = (f_normal[1]*p->state.pos[2])/R;
}
else
{
for (i=0; i<idim; i++)
normal[i] = f_normal[i];
}
}
else
d=Get_Domain(1);
for (i=0.; i<idim; i++)
normal[i] = f_normal[i];
C_UDMI(c,tcell,0) += 1.0;
```

```c
if (p->type==DPM_TYPE_INERT)
{
alpha = M_PI/2. - acos(MAX(-1.,MIN(1.,NV_DOT(normal,p->state.V)/
MAX(NV_MAG(p->state.V),DPM_SMALL))));
if ((NNULLP(t)) && (THREAD_TYPE(t) == THREAD_F_WALL))
F_CENTROID(x,f,t);
/* calculate the normal component, re-scale its magnitude by the
coefficient of restitution and subtract the change */
/* Compute normal velocity. */
for(i=0; i<idim; i++)
{
vn += p->state.V[i]*normal[i];
vpabs+=pow(p->state.V[i],2.);
}
vpabs=pow(vpabs,0.5);
/*compute critical velocity*/
ks = (1-(nu_s*nu_s))/(3.14*E_s);
kp = (1-(nu_p*nu_p))/(3.14*E_p);
calc = (5.*3.14*3.14*(ks+kp))/(4.*(pow(P_RHO(p),1.5)));
E = 0.51*(pow(calc,(2./5.))); /*El-Batsh parameter*/
vcr = pow(((2*E)/P_DIAM(p)),(10./7.));
Message("Critical_capture_Velocity_is_%g\n",vcr);
Message("Normal_Particle_Velocity_is_%g\n",vn);
MassImpact= P_FLOW_RATE(p); /* flow rate of particles in
stream in kg/s */
C_UDMI(c,tcell,1)+=MassImpact;
val = ((1.-(pow(nu_s,2.)))/E_s)+((1.-(pow(nu_p,2.)))/E_p);
kc = (4./3.)/val;
/*calculating critical wall shear velocity for rolling*/
```

114

```
ucws = ((1*Wa)/(C_R(c,tcell)*P_DIAM(p)))*(pow((Wa/(P_DIAM(p)*kc)),
(1./3.)));
ucrr=sqrt(ucws);
Message("Wall_shear_velocity_for_rolling_is_%g\n",ucrr);
/*calculating critical wall shear velocity for sliding*/
ucrs=0.5*pow((k*Wa)/(rho_p*P_DIAM(p)),0.5);
Message("Wall_shear_velocity_for_sliding_is_%g\n",ucrr);
/*calculating wall friction velocity */
yplus=F_STORAGE_R(f,t,SV_WALL_YPLUS_UTAU);
ds=C_WALL_DIST(c,tcell);
ustar=(VISC*yplus)/(ds*C_R(c,tcell));
Message("Wall_friction_velocity_is_%g\n",ustar);
/* Alternate Method 1*/
/*dudz = -1*C_DUDX(c,tcell);
ustar= sqrt((VISC*dudz)/C_R(c,tcell));
Message("Friction vel by regular formula is %g\n",ustar);*/
/* Calculating drag force*/
Fd=8.007*pow(P_DIAM(p),2)*1.225*pow(ustar,2);
Message("Drag_force_is_%g\n",Fd);
/* Calculating pull off force */
Fpo=2.355*Wa*P_DIAM(p);
Message("Pull_off_force_is_%g\n",Fpo);
/* Calculating adhesion distance*/
distance=4.71*Wa*pow(P_DIAM(p),2)/kc;
a=pow(distance,(1/3));
/* calculating dragmoment*/
dragmoment=Fd*P_DIAM(p)/2;
Message("Drag_moment_is_%g\n",dragmoment);
/* calculating adhesionmoment*/
```

```
adhesionmoment=Fpo*a;
Message("Adhesion_moment_is_%g\n",adhesionmoment);
/* calculating adhesionfriction */
adhesionfriction=Fpo*k;
Message("Adhesion_friction_is_%g\n",adhesionfriction);
MassImpact=P_FLOW_RATE(p);
tem_Particle_Dia=P_DIAM(p)*pow(10,6);
MassI=1.33*3.14*pow((tem_Particle_Dia/2),3)*rho_p;
xpos=P_POS(p)[0];
ypos=P_POS(p)[1];
zpos=P_POS(p)[2];
particle=p->part_id;
fp1=fopen("Impact2.txt","a");
fprintf(fp1,"%f_%f_%f_%f_%f_%f_%f_%f_%f\n",
particle,tem_Particle_Dia,vn,vcr,MassI,ustar,xpos,ypos,zpos);
fclose(fp1);
fp5=fopen("forces.txt","a"); fprintf(fp5,"%f_%f_%f_%f_%f_%f_%f\n",
particle,tem_Particle_Dia,Fd*pow(10,10),Fpo*pow(10,10),dragmoment*pow
(10,10),adhesionmoment*pow(10,10),adhesionfriction*pow(10,10));
fclose(fp5);
/* PARTICLE DOES NOT STICK*/
if(vn > vcr)
{
C_UDMI(c,tcell,2) += 1.0;
C_UDMI(c,tcell,3) += P_FLOW_RATE(p);
/* Subtract off normal velocity. */
for(i=0; i<idim; i++)
p->state.V[i]-= vn*normal[i];
/* Apply coefficient of restitution. */
```

```
for(i=0; i<idim; i++)
p->state.V[i]*= tan_coeff;
/* Add reflected normal velocity. */
for(i=0; i<idim; i++)
p->state.V[i]-= nor_coeff*vn*normal[i];
/* Store new velocity in state0 of particle */
for(i=0; i<idim; i++)
p->state0.V[i]= p->state.V[i];
return PATH_ACTIVE; }
/* PARTICLE DEPOSITS*/
else
if(dragmoment>adhesionmoment)
{
if(ustar < ucrr)
{
/*num of particles deposited or num of hits*/
C_UDMI(c,tcell,4) += 1.0;
/* mass of particles deposited*/
C_UDMI(c,tcell,5) += P_FLOW_RATE(p);
tem_Mass=P_FLOW_RATE(p);
MassS=1.33*3.14*pow((tem_Particle_Dia/2),3)*rho_p;
xpos=P_POS(p)[0];
ypos=P_POS(p)[1];
zpos=P_POS(p)[2];
particle=p->part_id;
fp2=fopen("Stickr.txt","a");
fprintf(fp2,"%f_%f_%f_%6.2f_%f_%6.2f_%f_%f_%f_%f\n",
particle,tem_Particle_Dia,MassS,vn,vcr,ucrr,ustar,xpos,ypos,zpos);
fclose(fp2);
```

```
}
}
else
if (Fd>adhesionfriction)
{
if (ustar < ucrs)
{
/*num of particles deposited or num of hits*/
C_UDMI(c,tcell,4) += 1.0;
/* mass of particles deposited*/
C_UDMI(c,tcell,5) += P_FLOW_RATE(p);
tem_Mass=P_FLOW_RATE(p);
MassS=1.33*3.14*pow((tem_Particle_Dia/2),3)*rho_p;
xpos=P_POS(p)[0];
ypos=P_POS(p)[1];
zpos=P_POS(p)[2];
particle=p->part_id;
fp3=fopen("Sticks.txt","a");
fprintf(fp3,"%f_%f_%f_%6.2f_%f_%6.2f_%f_%f_%f_%f\n",
particle,tem_Particle_Dia,MassS,vn,vcr,ucrs,ustar,xpos,ypos,zpos);
fclose(fp3);
}
}
else
if (vn<vcr)
{
/*num of particles deposited or num of hits*/
C_UDMI(c,tcell,4) += 1.0;
/* mass of particles deposited*/
```

```
C_UDMI(c,tcell,5) += P_FLOW_RATE(p);
tem_Mass=P_FLOW_RATE(p);
MassS=1.33*3.14*pow((tem_Particle_Dia/2),3)*rho_p;
xpos=P_POS(p)[0];
ypos=P_POS(p)[1];
zpos=P_POS(p)[2];
particle=p->part_id;
fp4=fopen("Stick.txt","a");
fprintf(fp4,"%f_%f_%f_%6.2f_%f_%6.2f_%f_%f_%f_%f\n",
particle,tem_Particle_Dia,MassS,vn,vcr,ucrr,ustar,xpos,ypos,zpos);
fclose(fp4);
}
}
return PATH_ABORT;
#endif
}
DEFINE_ON_DEMAND(reset_UDMsnew)
{
int i=0;
Thread *t;
Domain *d;
cell_t c;
face_t f;
d=Get_Domain(1);
Message("Setting_UDMs_\n");
thread_loop_c(t,d)
{
begin_c_loop(c,t)
{
```

```
for ( i =0; i <6; i++)
C_UDMI( c , t , i )=0.0;
}
end_c_loop ( c , t )
}
}
```

Vita Auctoris

Name	Ravinder Singh Gill
Place of Birth	Dharoud, Punjab, India
Year of Birth	1991
Education	University of Windsor, Windsor ON 2010-2014 B.A.Sc.
	University of Windsor, Windsor ON 2014-2016 M.A.Sc.